Active/Passive control of fluid-borne and structure-borne disturbances in fluid-filled piping systems

By

Mustafa Baris Kiyar

Thesis submitted to the Faculty of the

Virginia Polytechnic Institute and State University

In partial fulfillment of the requirements for the degree of

Master of Science

In

Mechanical Engineering

APPROVED:

_____

Dr. Chris R. Fuller, Committee Co-chair

_____

Dr. Marty E. Johnson, Committee Co-chair

_____

Dr. Mike Kidner

Blacksburg, Virginia

Defended on November 14, 2003

Keywords: Active/passive control, Coupled waves, Piping systems

Active/Passive control of fluid-borne and structure-borne disturbances in fluid-filled piping systems

by

M. Baris Kiyar

Committee Co-chairs: M. E. Johnson & C. R. Fuller

Mechanical Engineering

(ABSTRACT)

Energy due to fluid-borne and structure-borne disturbances propagating in a fluid-filled pipe will be carried by the structure and the fluid. Energy transfer may occur between these two media due to the coupling between the structure and the fluid. It's not clear when the excitation is fluid-borne or structure-borne, due to the complexity in piping installation designs and the strong coupling between the fluid and shell walls. It is necessary to devise control approaches that tackle both components of the excitation simultaneously. This study will demonstrate new approaches in active and passive control techniques and show their advantages over classical control approaches.

It is necessary to understand the physical behavior of fluid-filled pipes, in order to develop a viable control methodology. The equations of motion for the shell and the fluid are needed to characterize the system. These combined with the dispersion equations can then be used to derive analytical expressions for energy flow in the system. The research is limited to lower order wave types. Hence, the expressions for energy flow are derived only for the *n=0* and *n=1* shell waves and *n=0* fluid wave. Higher order waves have cut-on frequencies and were not analyzed. Current sensing methodologies are

limited to the analysis of wave types separately. A new approach of wave decomposition using multiple sensors is developed and used to characterize discontinuities along the pipe.

The effect of discontinuities and correct control methodologies are investigated. A new control methodology is developed and implemented. The natural distribution of energy into different wave types as it encounters discontinuities is used to devise control solutions with non-intrusive inertial actuators. Improvements of *16 dB* in shell waves and *12 dB* in fluid waves over the correct control approach are experimentally demonstrated.

Acknowledgements

I would like to take this opportunity to thank all the people who have contributed to the achievement of this work. I would like to thank my committee co-chairs Dr. Chris Fuller for giving me the opportunity to work in the field of acoustics and Dr. Marty Johnson for his valuable time and contributions. Their technical expertise and insight into complex problems was highly educational. I would like to thank Dr. Mike Kidner for serving on my advisory committee. Special thanks are due for Mr. Wonho Joo of Hyundai Heavy Industries, Korea, for his support during the course of this work.

I would like to extend my appreciation to all my friends in the Vibration and Acoustics Laboratories. Special thanks are due to Dawn Bennett and Lynda King for their moral support. I would like to recognize Dr. Jamie Carneal and Steve Booth for their help.

I would like to thank my entire family and friends in Turkey for their continual support and push from overseas. I would like to thank my parents, Tekin and Mucella Kiyar and my sister Burcu for being there when I needed them. I can't thank them enough or repay them for all they have given. There are far too many names that need recognition and pages wouldn't suffice if I tried to recount them all here. You know who you are.

Table of contents

Table of figures

Chapter 1

Introduction

Piping installations are integral parts of many engineering systems and find various uses in both military and commercial applications. While pipes provide the useful function of energy and fluid transfer, they can also transmit unwanted noise and vibrations. These unwanted vibrations can be both fluid-borne and structure-borne. Unwanted vibrations have two main effects: (i) mechanical fatigue and (ii) excessive radiated noise. It is, therefore, of utmost importance to develop integrated noise and vibration control solutions for piping installations. Furthermore, noise control solutions are of special importance for naval military vessels that rely on silent operation.

Noise and vibrations in fluid filled pipes can be generated by many sources such as pumps used to convey the fluid, orifices that control flow and bends that change the direction of flow. Fluid borne pulsations can be caused by turbulence which is initiated by pumps, compressors, or discontinuities along the pipe. Structure-borne vibrations can be excited due to imbalances in rotating machinery or supporting structures. Due to the strong coupling between the fluid and the shell walls, the excitation is both fluid-borne and structure-borne. In addition, all wave types present in the system will be coupled together at discontinuities and energy will be transferred between wave types, rendering a noise control solution that solely focuses on one wave type ineffective. Therefore, the study and elimination of flanking energy pathways in control applications is emphasized.

Two parameters are important when analyzing fluid filled pipes: (i) frequency and (ii) the ratio of fluid mass to shell mass per unit length. The number of propagating waves will increase as the frequency increases and the ratio of masses will determine the coupling between fluid waves and shell waves. Noise control in maritime vessels is important at lower frequencies, as waves with lower frequencies travel more effectively through structural supports. Hence, this thesis concentrates on the three main wave types that carry energy at lower frequencies: the *n=0* extensional and *n=1* bending waves in the shell and the *n=0* fluid wave where *n* denotes the circumferential wave order.

Some of the existing noise control technologies currently finding use are reviewed in chapter 4. New methods for the experimental determination of fluid-filled pipe behavior are presented in chapter 3. A method for the determination of coupled wave amplitudes using multiple sensors is introduced. This new approach of experimentally determining multiple wave amplitudes portrays a more realistic solution to the mechanism of fluid filled pipes. New and novel noise control solutions are then presented and their advantages over their predecessors are explained. Active methods of noise control in pipes are also investigated.

1.1. Literature review and past related work

The rest of this chapter contains a review of the theoretical models for the vibration of pipes and experimental methods. It concludes with a summary of the thesis structure.

1.1.1. Vibrations of shells

There are a number of shell theories that have been proposed to study the behavior of thin-shells. A thin shell can be considered as a three dimensional body that is bounded by two closely spaced surfaces. Industrial cylindrical vessels and pipes are a subset of thin shells. Leissa [1] presents a detailed discussion of various thin shell theories. Gazis [2] studied the three-dimensional propagation of waves for *in vacuo* cylinders. Fuller [3] described the free vibrations of infinitely long thin cylindrical shells using the Flügge shell theory. Fegeant [4] formulated closed form solutions for point mobilities of axisymmetrically excited cylindrical shells. More recently, Brennan & Variyart [5] have derived closed form solutions for the mobility of circumferential modes in an infinitely long thin walled pipe. Brennan & Variyart [6] have also derived simplified dispersion relationships for *in vacuo* pipes. Zhang *et al.* [7] investigated the vibrations of *in vacuo* shells using a wave propagation approach and compared these with results obtained from finite element analysis. The reader is also encouraged to refer to Flügge [8], Love [9], and Donnell [10] for detailed descriptions of shell theories.

1.1.2. Research on fluid filled cylindrical shells

While the study of vibrations of *in vacuo* pipes is a good starting point and can be used where the internal medium is significantly less dense than the shell, the solutions provided by these studies cannot be used when there is a heavy internal loading. Fuller and Fahy [11] have studied the characteristics of wave propagation in fluid filled shells through the examination of dispersion curves and energy distributions of free waves. The behavior of free waves in a fluid filled shell was found to depend on mass per unit length of fluid to the mass per unit length of shell and shell wall thickness. It was found

that energy would be carried in the fluid or the shell at low frequencies depending on the excitation and energy would be shared between the shell and fluid at higher frequencies. Fuller [12] investigated the input mobility of an infinite cylindrical shell. It was shown that at higher frequencies energy was distributed between the shell and the fluid and any vibration control solution requires control of both fluid waves and shell waves. Fuller [13] has also studied the response of an infinite cylindrical shell to internal monopole excitation. It was found that vibrational energy would be in the fluid and energy would be transferred to the shell as the excitation source moved closer to the shell wall. Brevart & Fuller [14, 15] studied the response of a coupled fluid-shell medium to impulse excitation. It has been found that most of the energy in the system is carried in the shell for beam (or of higher mode) type excitations. Finnveden [16] derived simplified equations of motion for the shell and fluid in fluid-filled pipes. Finnveden [17] derived the expressions for modal density in fluid filled pipes and input power from point sources. Feng [18] studied the acoustic properties of fluid-filled pipes and compared energy distributions with different types of excitation. Feng [19] also compared experimental results with his theory. It was found that theoretical prediction agrees with experimental results of *in vacuo* pipes, whereas there is a big deviation in experimental results from theoretical results in fluid-filled pipes. Xu & Zhang [20, 21] studied the vibrational power flow in a fluid-filled cylindrical shell and compared the results with vibrational power flow of an *in vacuo* shell. Zhu [22] studied the coupling between the fluid and structure using the Rayleigh-Ritz method. Pinnington [23] investigated the axisymmetric waves propagating in a pressurized flexible tube. It was shown that at low frequencies only axisymmetric waves propagate and the stiffness of the shell plays an important role in the coupling between the fluid and the structure. Zhang *et al.* [24] studied the fluid-structure interaction in pipes in the frequency domain.

1.1.3. Research on fluid filled pipes with fluid flow

Tijdeman [25] has studied the propagation of sound waves in cylindrical tubes filled with gas. Michalke [26] studied the effects of mean flow on sound generation in a pipe. The equations of motion for the fluid were derived for very small mach numbers and the solutions were derived in the form of acoustic modes. Gorman *et al.* [27] derived the partial differential equations governing the vibration of a pipeline with viscous flow. Brevart & Fuller [28] studied the effects of internal flow on the distribution of vibrational energy in a fluid-filled cylindrical shell. It is shown that the effect of flow is greatest near coincidence or the cut-on frequencies of the higher order waves.

1.1.4. Research on experimental work

Most of the publications on vibrations of fluid-filled pipes (or shells) consist of theoretical work. While these publications present closed-form solutions and can be readily applied, they are mostly limited to basic piping schemes or models where the boundary conditions and the system can easily be identified. In reality, piping systems are usually complex and identification of system parameters is very difficult. Therefore, good experimental methods and techniques are indispensable.

The basis for the basic wave decomposition technique was established by Chung and Blaser [29]. Pavic studied the application of wave decomposition techniques to fluid-filled pipes [30]. Fahy [31] used wave decomposition methods based on phase differences of closely placed microphones to measure acoustic intensity. Pavic [32, 33] and Verheij [34, 35] have presented configurations for strain gauges and accelerometers to measure vibrational energy flow. Royston [36] has used shaped PVDF sensors to

measure the acoustic wave in water filled steel pipes. Pinnington & Briscoe [37] studied the application of external sensors to measure the fluid pulsations in fluid-filled pipes. Briscoe & Pinnington [38] have also used PVDF transducers in the form of PVDF wire to measure power in axisymmetric waves in both fluid-filled and *in vacuo* pipes. It has been shown [38] that externally applied sensors can detect the fluid waves in soft walled pipes, but will detect fluid waves in hard walled pipes if the excitation is only in the fluid. For all practical purposes the excitation in a hard walled pipe will be both fluid-borne and structure-borne. Thus, results from these measurements will be questionable, as higher order waves will interfere with measurements. Taylor [39] has presented the use of two-channel method to measure structural intensity in beams. More recently, de Jong *et al.* [40] has presented a procedure to measure vibro-acoustic energy flow in pipes. Configurations for circumferential wave decomposition in thin walled pipes have been described in de Jong's [41] dissertation. Ming *et al.* [42] has also worked on the same measurement principle as de Jong.

1.1.5. Research on discontinuities in fluid filled pipes

Piping systems are complex structures with various discontinuities. The amount of research on the effects of these discontinuities on wave propagation is scarce at best and only few researchers have tackled this issue. Finnveden [43] studied the effects of flanges on the vibrational behavior of fluid-filled pipes. It has been shown that the stiffness controlled shell mode and rigid mass resonate just below the cut-on frequency of shell modes. Xu *et al.* [44] studied the effects of wall joints in pipes on wave propagation. The effect of the differences in materials on both sides of the joint is emphasized and the use of this effect as a noise control approach is suggested.

1.1.6. Research on control approaches for fluid filled pipes

While studies on theory of fluid-filled pipes can easily be found, research on noise and vibration control approaches are very difficult to locate. Dodson *et al.* [45] studied the effects of quarter-wavelength silencers in hydraulic systems. The insertion loss characteristics of quarter-wavelength tubes were analyzed. However, the flanking energy pathways or the presence of multiple waves were ignored. Kravchenko [46] proposed the use of active vibration isolation in piping systems to control transmitted vibrations through supports. Lin & Tsai [47] tried to control non-linear vibrations in pipes. However, their research ignores the effects of flow and pressure. A comprehensive study on active control of vibrations in fluid-filled cylindrical shells was conducted by Brevart [48]. A Plexiglas pipe was used as a cylindrical shell. The performance of active control depended on the excitation type and control performance was limited due to the coupling between the shell and the fluid. Maillard [49] experimented on active control of pulsations in fluid-filled pipes due to pump pulsations. Non-intrusive piezoelectric based actuators were mounted externally to control fluid pulsations. However, their performance was limited and did not result in perfect cancellations.

1.1.7. Other miscellaneous research

Other researchers have studied various topics related with fluid-filled pipes. Ruotolo [50] has studied the effects of stiffeners on wave propagation and compared various shell theories. Muggleton [51] *et al.* has studied the changes in the wavenumber for leak detection. It has been shown that the wave speed of the fluid wave will be less than the free-field wave speed. Xu *et al.* [52] studied the effects of periodically stiffening the pipe on wave propagation. The changes in the stiffening conditions are discussed and their

effect on controlling power for higher order modes is presented. Feng [53] studied the effects of build-up inside the pipe on the wave propagation. It has been shown that build-up inside the pipe will reduce the wave speed and act as an absorptive layer. Liu *et al.* [54] studied fluid-structure interaction in fluid-filled pipes using statistical energy analysis.

1.2. Scope of work and contribution of thesis

The object of this study was to develop robust noise and vibration control solutions for fluid-filled piping systems. Most of the work presented in this thesis is experimental with some theoretical effort going into developing new approaches in sensing methodologies. Both active and passive noise control solutions have been investigated with the final goal of applying the results to a realistic piping system to achieve the desired control.

Most of the current research done in fluid-filled pipes consists of theoretical modeling and lacks practical applicability. There is a noteworthy deficiency in research on measurement techniques that have practical applications. Many researchers base their techniques on the standard two-channel method and forego correcting for the coupled properties of the fluid-filled system by targeting specific wave types. Although, some techniques like Pinnington [37] are quite easy to apply, they require exact knowledge of system behavior and characteristics to yield qualitative results and are susceptible to errors due to changes in the system (i.e. bubbles in the fluid).

The first part of this study involved the development of robust practical measurement techniques that could be readily applied to realistic systems. The ten-channel method was developed for the specific purpose of assessing multiple wave types at the same

time and their contributions to the total energy in the system and its ease of application. It requires a single set of measurements and is impervious to changes in the system.

There is also a significant lack of research on noise and vibration control approaches. Present passive noise and vibration devices continue to be used even though they have inherent flaws that prevent them from being effective. Furthermore, these passive devices act as discontinuities and rather than functioning as a control tool, they serve to redistribute energy between various wave types rendering noise control approaches ineffective if not detrimental. Kiyar *et al.* [55] studied these devices and discontinuities that render them ineffective and characterized their properties. By analyzing the flaws of these classical devices new control approaches were developed. Two new passive control devices presented by Kiyar *et al.* [56] are the symmetric Helmholtz resonator and the symmetric distributed vibration absorber. The symmetric Helmholtz resonator is an improvement on the classical Helmholtz resonator. The device is made symmetric with a circular Helmholtz volume and incorporates opposing necks to remove the effect of shell excitation that renders a classical resonator ineffective. Symmetric distributed vibration absorber is another new device. It takes a standard vibration absorber and wraps it around the pipe symmetrically. It works by simultaneously controlling both the in-plane and extensional waves. Additionally, the stiffness layer of the symmetric distributed vibration absorber can be chosen or adjusted in such a way that the resonant frequency of the absorber in the radial direction equals the resonant frequency of the absorber in the axial direction.

The amount of research on active control of sound and vibration in fluid-filled pipes is sparse and few researchers have taken the time to study the application of ANC. Most of the research on this area involves controlling a specific wave type present in the fluid-

filled pipe system. Discontinuities in a fluid-filled pipe redistribute energy and render active control solutions that tackle a single type of wave ineffective. Kiyar *et al.* [57] presented an active control solution using externally applied inertial actuators to control multiple energy carrying wave types at the same time in a fluid-filled pipe with flow. The ease of application for the active control system and its performance makes it a viable noise control approach.

It is the author's hope that the noise and vibration control solutions developed along the course of this study will find their way into piping installations found in the industry. The main consideration during the investigation of the solutions presented in this thesis was their practicality and applicability.

1.3. Arrangement of thesis

This thesis can be divided into three main segments: the theory describing the behavior of fluid-filled pipes, the methods used to measure this behavior, and relevant noise control solutions.

Chapter two starts with the description of various wave types present in fluid-filled pipes. The shell theories governing the behavior of fluid-filled pipes will be compared and equations of motion for the shell and the fluid will be derived. These equations of motion will then be coupled together to describe the behavior of the coupled fluid-shell system. The dispersion equation will be derived for the non-dimensional wavenumbers and the dispersion curves will be presented. Lastly, the equations for energy flow in the system will be presented.

Chapter three presents the measurement methods used in this study. A theoretical basis on circumferential and axial wave decomposition is presented. Wave amplitude and cross-spectrum estimates that use two measurements are reviewed. Wave amplitude decomposition methods based on multiple measurements are analyzed and the ten-channel decomposition method developed during the course of this study is presented. The validity of the measurement methods is analyzed and the susceptibilities of these methods to errors are presented. Experimental results using these methods are presented and the chapter is finished with descriptions of the limitations of these methods.

In chapter four the passive noise control solutions found in piping installations are described. Experimental setups used for the work are presented. The behaviors of supporting structures are analyzed and their effects on wave types are presented. Passive isolators like the quarter-wavelength tube and Helmholtz resonator are analyzed and their limitations are presented. The symmetric Helmholtz resonator and symmetric distributed vibration absorber are investigated and their advantages over their predecessors are discussed.

An active noise control approach for fluid-filled pipes is discussed in chapter 5. The theory of the filtered reference-LMS feed-forward controlling scheme is reviewed. Calculation of wave amplitudes is used to assess the effectiveness of active control. The chapter is concluded with a discussion of active control results.

Overall conclusions and possible directions for future work are presented in the final chapter.

Chapter 2

The theories of vibration of shells

In this chapter the theory of vibrations in cylindrical shells is presented. The chapter begins with a description of wave types present in the system. The equations of motion for the shell and fluid will then be presented. The dispersion relationship and dispersion curves will be presented and the power flow in each of the waves will be derived.

2.1. Wave types present in the system

The concept of a "ring frequency" ω_o is used to separate the vibrational behavior into high and low frequency regimes. The ring frequency is given by $\omega_o = {}^{c_l}\!/_{a}$, where *a* is the mean radius of the shell and the c_L is the speed of the extensional wave in a plate made of the same material. The pipe vibrates in the breathing mode at the ring frequency and the circumference around the mean radius of the pipe equals the corresponding wavelength $\lambda = 2\pi {}^{c_L}\!/_{\omega_o}$ in a plate. The excitation frequency can be normalized to the ring frequency, $\Omega = \omega {}^{a}\!/_{c_L}$ where Ω is the non-dimensional excitation frequency. The non-dimensional frequency produces behavior that is independent of the pipe size. Pavic has shown that the equations of motion for the coupled fluid-filled system can be simplified at frequencies well below the ring frequency [57]. The ring frequency for the pipe used in this study (2" NPS galvanized steel) with a mean radius of 30.35x10e-3 m is

found to be approximately *19 kHz*. Therefore the simplified equations were utilized in this study.

The behavior of the pipe well below the ring frequency can be described using four wave types: (i) *n=0* longitudinal wave with *n* describing the circumferential mode number, (ii) *n=0* fluid wave (also called the acoustic wave), (iii) *n=0* torsional wave, which is predominantly uncoupled from the fluid, and (iv) *n=1* shell wave, which is also called the bending wave. In this mode the pipe behaves like a beam. The cross-section of the pipe remains unchanged, but it oscillates about the longitudinal (*z*) axis. The higher order modes are not taken into consideration in this study as only imaginary wave number solutions exist below their "cut-on" frequency which do not contribute to energy transmission.

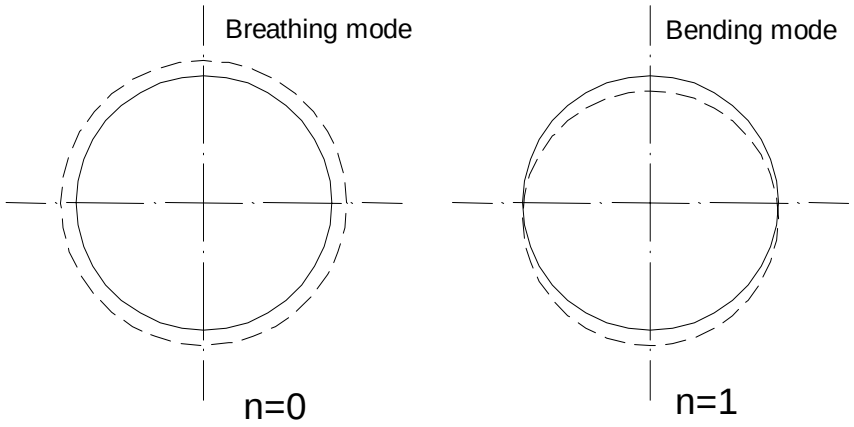

Figure 2.1. Modal shapes of shell

2.2. Review of theories for the vibration of circular shells

The derivations of theories to describe the vibration of thin circular cylindrical shells can be found in Leissa [1], Soedel [58], and Heckl [59]. The differences in the theories are due to different simplifications of the linear three dimensional theory of elasticity. The thin shell theory can be applied only if the thickness of the shell is small compared to the other dimensions ($h/r << 1$). The thickness of the shell need not be constant, but constant thickness simplifies the equations. This study is only concerned with shells of constant thickness.

The following assumptions are made in the classical theory of thin shells:

1) The thickness of the shell is small compared to other dimensions, i.e. the smallest radius of curvature.
2) Strains and displacements are sufficiently small so that the quantities of the second and higher order terms in the strain-displacement terms can be neglected.
3) The transverse normal stress is small compared with the other normal stress components and may be neglected (see figure 2.3).
4) Normals to the undeformed middle surface remain straight and normal to the deformed middle surface and suffer no extension (see figure 2.2).

The first assumption defines the “thin shell.” The second assumption permits us to refer all calculations to the original configuration of the shell and ensures that the differential equations are linear. The fourth assumption is also known as Kirchoff’s hypothesis and categorizes thin shells. The third and fourth assumptions deal with the constitutive

equations of the shell and assume the shell to behave like a material with special orthotropy where the stress in the radial direction is infinite and therefore no normal and shear stresses exist in this direction [1].

2.2.1. Equations of motion

This section will describe the equations of motion governing fluid filled pipes of infinite length. The materials of the shell and the fluid are assumed to be homogeneous. The equations describe the linear behavior of the system.

2.2.1.1. Equation of motion for the shell

Figure 2.2 shows the geometry and the coordinate system for circular cylindrical shell. The radius of the curvature along the mean-radius of the shell is denoted by *a*, the shell thickness is denoted by *h*, the cylindrical coordinates are denoted by *z*, *r*, and θ, and the orthogonal displacement components are denoted by *u*, *v*, and *w*. Figure 2.3 shows the stresses on an infinitesimal shell element.

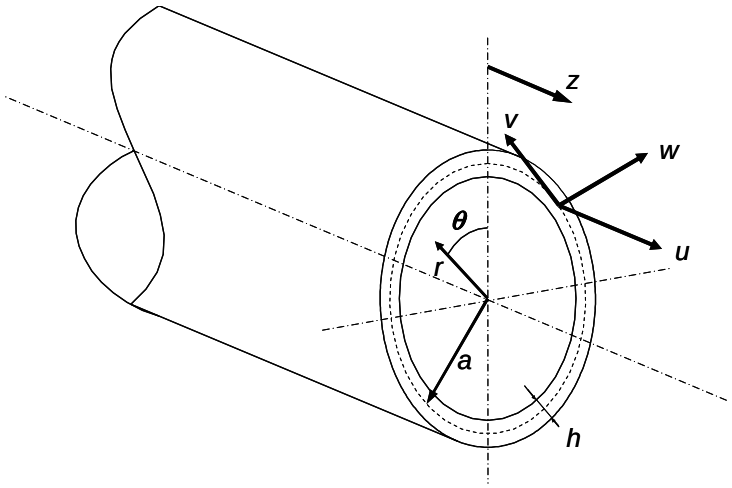

Figure 2.2. Cylindrical coordinate system and modal displacements

The displacement variations through the shell are given by:

$$u \approx u_a - (r-a)\frac{\partial w_a}{\partial z}, \quad v \approx v - \frac{r-a}{a}\left(\frac{\partial w_a}{\partial \theta} - v_a\right), \quad w \approx w_a \tag{2.1}$$

where the subscript a denotes the mean radius of the shell [1]. The remaining strain-displacement equations are:

$$\varepsilon_z = \frac{\partial u}{\partial z}, \quad \varepsilon_\theta = \frac{1}{a}\frac{\partial v}{\partial \theta} + \frac{w}{a}, \quad \gamma_{z\theta} = \gamma_{\theta z} = \frac{\partial v}{\partial z} + \frac{1}{a}\frac{\partial u}{\partial \theta} \tag{2.2}$$

with ε and γ denoting the strains with the matching stress-strain equations as:

$$\sigma_z = \frac{E}{1-\nu^2}(\varepsilon_z + \nu\varepsilon_\theta), \quad \sigma_\theta = \frac{E}{1-\nu^2}(\varepsilon_\theta + \nu\varepsilon_z), \quad \tau_{z\theta} = \frac{E}{2(1+\nu)}\gamma_{z\theta} \tag{2.3}$$

where *E* denotes the Young's modulus of elasticity, ν denotes the Poisson's ratio, σ denotes the normal stresses, and τ denotes the shearing stresses (figure 2.3).

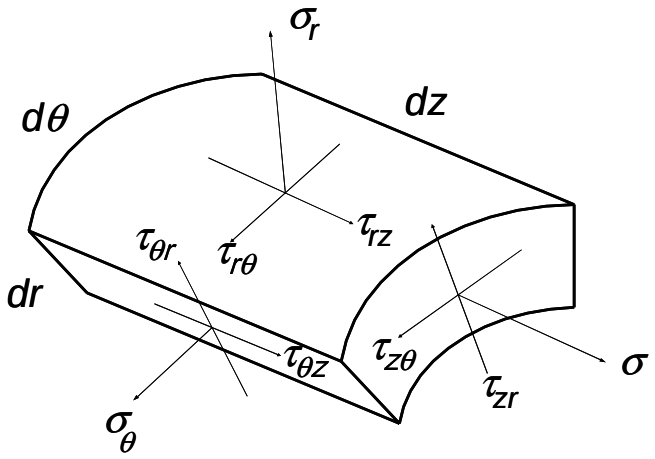

Figure 2.3. Stresses on an infinitesimal shell element

The equations of motion for an infinitesimal element of the shell are:

$$\frac{\partial \sigma_z}{\partial z} + \frac{1}{r}\frac{\partial \tau_{z\theta}}{\partial \theta} + \frac{1}{r}\frac{\partial}{\partial r}(r\tau_{zr}) = \rho_s \frac{\partial^2 u}{\partial t^2}$$

$$\frac{1}{r}\frac{\partial \sigma_\theta}{\partial \theta} + \frac{1}{r}\frac{\partial \tau_{z\theta}}{\partial z} + \frac{1}{r}\frac{\partial}{\partial r}(r\tau_{\theta r}) + \frac{\tau_{\theta r}}{r} = \rho_s \frac{\partial^2 v}{\partial t^2} \qquad (2.4)$$

$$\frac{1}{r}\frac{\partial}{\partial r}(r\sigma_r) + \frac{\partial \tau_{zr}}{\partial z} + \frac{1}{r}\frac{\partial \tau_{\theta r}}{\partial \theta} - \frac{\sigma_\theta}{r} = \rho_s \frac{\partial^2 w}{\partial t^2}$$

Application of boundary conditions for the normal and shear stresses at the inner and outer surfaces of the shell make up for the lack of radial stress-strain equations:

$$\sigma_r(r = a_i) = p_i(r = a_i), \qquad \tau_{zr}(r = a_i) = \tau_{\theta r}(r = a_i) \approx 0,$$

$$\sigma_r(r = a_e) = -p_e(r = a_e), \qquad \tau_{zr}(r = a_e) = \tau_{\theta r}(r = a_e) \approx 0 \qquad (2.5)$$

a_i and a_e represent the inner and outer radii of the shell and p_i and p_e represent the internal and external fluid pressures. Equation 2.6 shows how these boundary conditions are applied to the shell.

$$\int_{a_i}^{a_e} \frac{1}{r}\frac{\partial}{\partial r}(r\sigma_r)\frac{r}{a}dr = \left(1 - \frac{h}{2a}\right)p_i - \left(1 + \frac{h}{2a}\right)p_e \qquad (2.6)$$

The resulting moments and forces on a shell can be derived by integration of the equations of motion over the shell dimensions. The different thin shell approximations that have been applied to these integrations have led to different sets of equations that differ by only 1% [1].

Reciprocally, the equations of motion can be expressed in terms of the force and moment resultants by integration of equations 2.4 over the shell thickness.

The integration of the equations of motion over the shell thickness and neglecting higher order terms yields the Love equations [11]:

$$\frac{\partial N_z}{\partial z}+\frac{1}{a}\frac{\partial N_{z\theta}}{\partial \theta}=\rho_s h\frac{\partial^2 u_a}{\partial t^2}, \quad \frac{\partial N_{\theta z}}{\partial z}+\frac{1}{a}\frac{\partial N_\theta}{\partial \theta}+\frac{Q_\theta}{a}=\rho_s h\frac{\partial^2 v_a}{\partial t^2},$$

$$\frac{a_i}{a}p_i-\frac{a_e}{a}p_e+\frac{\partial Q_z}{\partial z}+\frac{1}{a}\frac{\partial Q_\theta}{\partial \theta}-\frac{N_\theta}{a}=\rho_s h\frac{\partial^2 w_a}{\partial t^2}, \tag{2.7}$$

$$\frac{\partial M_z}{\partial z}+\frac{1}{a}\frac{\partial M_z}{\partial \theta}=-Q_z, \qquad \frac{\partial M_{z\theta}}{\partial z}+\frac{1}{a}\frac{\partial M_\theta}{\partial \theta}=-Q_\theta$$

where *N* and *Q* denote the resultant forces and *M* denotes resultant moments (see figure 2.4). Rotary inertia can be included, but this effect is generally negligible unless the shell becomes too thick. In this case, it becomes equally important to include the effects of shear deformation and this requires a complete new formulation of shell theory and this results in differential equations of a tenth order set [1].

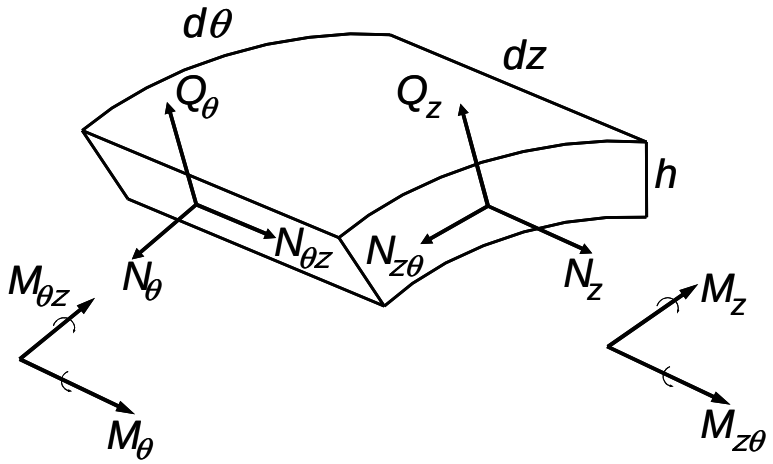

Figure 2.4. Resultant forces and moments on pipe wall

2.2.1.2. Equation of motion for fluid

By assuming external source for flow, the orthogonal fluid displacement components and fluid density fulfill the linearized equation of continuity for a homogeneous, compressible fluid:

$$\frac{\partial \rho_f}{\partial t} + \rho_f \left[\frac{\partial^2 \xi_z}{\partial z \partial t} + \frac{1}{r}\frac{\partial}{\partial r}\left(r \frac{\partial \xi_r}{\partial t} \right) + \frac{1}{r}\frac{\partial^2 \xi_\theta}{\partial \theta \partial t} \right] = 0 \qquad (2.8)$$

Because the flow is subsonic, effects of mean flow can be neglected. The Mach number will usually be very low ($M = u/a << 1$), in a heavy fluid like water. The isentropic equation of state relates the fluid density and pressure as:

$$\frac{\partial \rho_f}{\partial p} = \frac{\rho_f}{K_f} \qquad (2.9)$$

In this equation the fluid bulk modulus is related to the velocity of sound in free field as $K_f = \rho_f c_f^2$. Bubbles in the fluid will reduce the speed of sound in the fluid due to increased damping and diffraction through homogeneously distributed small bubbles.

The fluid motion is described by Euler equations:

$$\frac{\partial p}{\partial z} = -\rho_f \frac{\partial^2 \xi_z}{\partial t^2}, \qquad \frac{1}{r}\frac{\partial p}{\partial \theta} = -\rho_f \frac{\partial^2 \xi_\theta}{\partial t^2}, \qquad \frac{\partial p}{\partial r} = -\rho_f \frac{\partial^2 \xi_r}{\partial t^2} \qquad (2.10)$$

Combining equations 2.8, 2.9, and 2.10 yields the acoustic wave equation for pressure p:

$$\frac{1}{c_f^2}\frac{\partial^2 p}{\partial t^2} = \frac{\partial^2 p}{\partial z^2} + \frac{1}{r}\frac{\partial}{\partial r}\left(r \frac{\partial p}{\partial r} \right) + \frac{1}{r^2}\frac{\partial^2 p}{\partial \theta^2} \qquad (2.11)$$

Fluid pressure and wall motion are related through the equation of continuity:

$$\xi_r \approx w_a \tag{2.12}$$

The equations 2.7 and 2.11 describe the wave propagation in an infinitely long fluid filled circular pipe.

2.2.2. Coupled modes

The responses that satisfy the equations of motion for shell wall with an axial wavenumber k_{nm} can be assumed of the form [39]:

$$u = \sum_{m=0}^{\infty}\sum_{n=0}^{\infty} U_{nm}\cos(n\theta)e^{\left[ik_{nm}z - i\omega t + i\pi/2\right]} \tag{2.13a}$$

$$v = \sum_{m=0}^{\infty}\sum_{n=0}^{\infty} V_{nm}\sin(n\theta)e^{[ik_{nm}z - i\omega t]} \tag{2.13b}$$

$$w = \sum_{m=0}^{\infty}\sum_{n=0}^{\infty} W_{nm}\cos(n\theta)e^{[ik_{nm}z - i\omega t]} \tag{2.13c}$$

The pressure field in the fluid which satisfies the acoustic wave equation in cylindrical coordinates is given by:

$$p = \sum_{m=0}^{\infty}\sum_{n=0}^{\infty} P_{nm}\cos(n\theta)J_n\left(k_m^r r\right)e^{[ik_{nm}z - i\omega t]} \tag{2.14}$$

where J_n denotes the Bessel function of order n, k_m^r is the radial wavenumber and is related to the free wavenumber $k_f = \omega/c_f$ by:

$$\left(k_m^r\right)^2 = k_f^2 - k_{nm}^2 \tag{2.15}$$

Boundary conditions at the shell inner surface dictate that the radial velocity of the pressure field must equal to the radial shell velocity *w*:

$$w = -\left(\frac{1}{i\rho_f \omega}\right)\frac{\partial p}{\partial r} = -\frac{k_m^r J_n'\left(k_m^r(a-h/2)\right)}{i\rho_f \omega} P_{nm}\cos(n\theta) J_n\left(k_m^r(a-h/2)\right) e^{[ik_{nm}z - i\omega t]} \tag{2.16}$$

Equating equation 2.16 and 2.13c enables us to relate the fluid pressure amplitude to the shell radial amplitude of vibration as:

$$P_{nm} = \left\{\frac{\omega^2 \rho_f}{k_m^r J_n'\left(k_m^r(a-h/2)\right)}\right\} W_{nm} \tag{2.17}$$

where ρ_f is the density of the fluid and the prime in the Bessel function denotes derivation with respect to the argument $k_m^r r$.

The pressure loading in the infinite circular pipe can thus be expressed as:

$$p(\theta, z)\big|_{r=a-h/2} = \sum_{n=0}^{\infty}\sum_{m=0}^{\infty} W_{nm} \frac{\omega^2 \rho_f J_n\left(k_m^r(a-h/2)\right)}{k_m^r J_n'\left(k_m^r(a-h/2)\right)} P_{nm}\cos(n\theta) J_n\left(k_m^r(a-h/2)\right) e^{[ik_{nm}z - i\omega t]} \tag{2.18}$$

2.2.3. Dispersion equation

The equations of free vibration of the infinite coupled fluid-filled pipe can be represented in the matrix form as follows:

$$\begin{bmatrix} L_{11} & L_{12} & L_{13} \\ L_{21} & L_{22} & L_{23} \\ L_{31} & L_{32} & L_{33} \end{bmatrix} \begin{Bmatrix} U_{nm} \\ V_{nm} \\ W_{nm} \end{Bmatrix} = \begin{pmatrix} 0 \\ 0 \\ 0 \end{pmatrix} \tag{2.19}$$

U, *V*, and *W* are the modal amplitudes of displacement for the shell. The matrix *L* given in 2.19 yields non-trivial solutions only if the determinant of *L* is equal to zero. Substitution of appropriate shell equations and setting the determinant equal to zero gives the dispersion equation, which is the frequency-wavenumber relationship of free waves in a fluid-filled pipe. The elements of the matrix [L] are different for different shell theories. The terms of the matrix [L] for the Donnell-Mushtari shell theory are given as:

$$L_{11} = -\Omega^2 + \left(k_{nm} a_i\right)^2 + \tfrac{1}{2}(1-\nu)n^2, \quad L_{12} = \tfrac{1}{2}(1+\nu)n\left(k_{nm} a_i\right), \quad L_{13} = \nu\left(k_{nm} a_i\right), \tag{2.20a-c}$$

$$L_{21} = L_{12}, \quad L_{22} = -\Omega^2 + \tfrac{1}{2}(1+\nu)\left(k_{nm} a_i\right)^2 + n^2, \quad L_{23} = n, \tag{2.20d-f}$$

$$L_{31} = L_{13}, \quad L_{33} = -\Omega^2 + 1 + \beta^2\left[\left(k_{nm} a_i\right)^2 + n^2\right]^2 - FL, \quad L_{32} = L_{23} \tag{2.20g-i}$$

where Ω is the non-dimensional ring frequency and is given by $\Omega = \omega a / c_L$. β is the shell thickness parameter and is given by $\beta = h^2/12a^2$. *FL* is the fluid loading term due to the presence of the acoustic field. For the *in vacuo* system the fluid loading term is zero. Fluid loading term is given by:

$$FL = \Omega^2 \frac{\rho_f}{\rho_s} \frac{a}{h} \frac{1}{\left(k_m a\right)} \left\{ J_n\left(k_m^r a\right) \Big/ J_n'\left(k_m^r a\right) \right\} \tag{2.21}$$

The non-dimensional radial wavenumber $k_m^r a$ can be written in the form of non-dimensional shell frequency and axial wavenumber as:

$$k_m^r a = \pm\left[\Omega^2\left(c_L \big/ c_f\right)^2 - \left(k_{nm}a\right)^2\right]^{1/2} \tag{2.22}$$

The non-trivial solutions to the dispersion equation yield the dispersion curves of the system.

2.2.4. Dispersion curves

Several authors [ref] have analyzed and presented dispersion curves in detail for a fluid-filled steel pipe. Our frequency range of interest is well below the ring frequency. Hence the figures presented are for the low non-dimensional frequencies (Ω<1). The solutions of the dispersion equation will yield waves that are either propagating ($\kappa_{nm} = \pm k_{nm}a$), near-field ($\kappa_{nm} = \pm ik_{nm}a$), or propagating waves with decaying amplitudes ($\kappa_{nm} = \pm k_{nm}a \pm ik_{nm}a$). Fuller has shown that waves with complex wavenumbers occur in pairs and produce an attenuated standing wave along the pipe. Waves that have complex wavenumbers decay with a factor of $e^{k_{nm}x}$ and their amplitudes are negligible after a distance equal to one pipe diameter. The evanescent behavior of waves has to be taken into account at discontinuities such as a 90 degree bend.

Figures 2.5 and 2.6 show solutions to the dispersion equation for circumferential modal order of n=0 and n=1 respectively. The real branches correspond to waves carrying energy and the imaginary branches represent evanescent behavior of fluid-filled pipes.

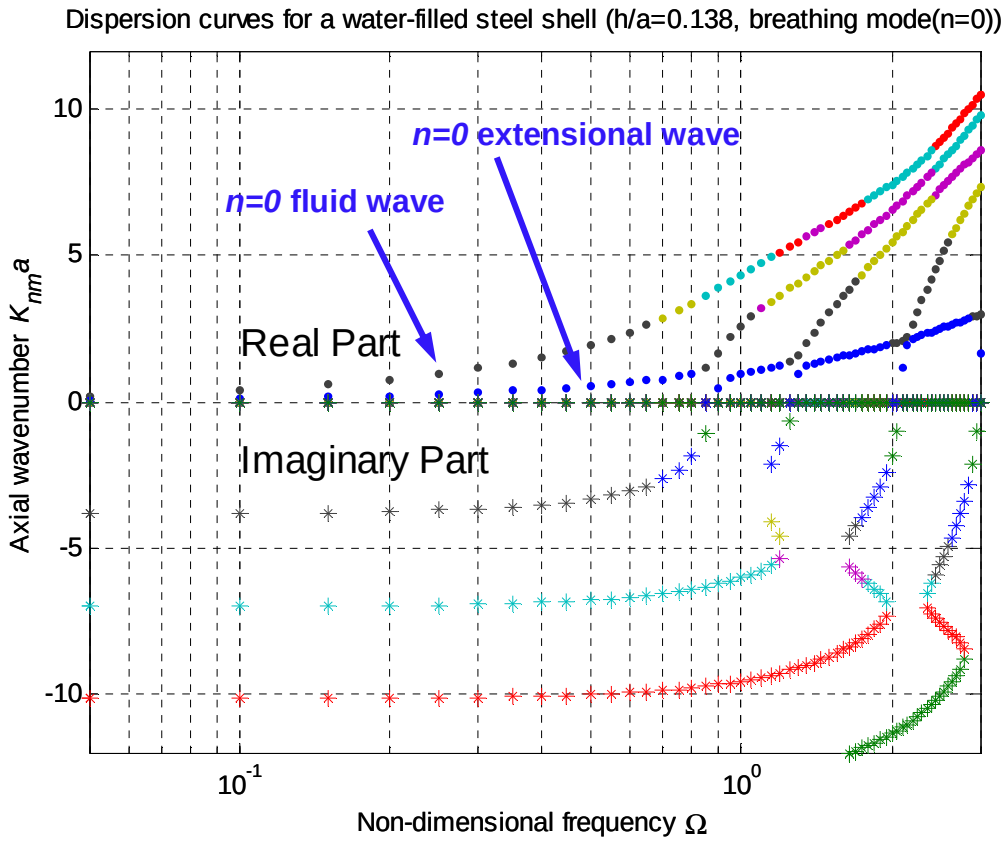

Figure 2.5. Dispersion curves for a water-filled steel shell of h/a=0.138 with n=0

Figure 2.5 shows typical dispersion curves for waves propagating with a circumferential modal order of *n=0* in a steel shell of *h/a=0.138*. The real solutions are shown as dots and the imaginary solutions are indicated with stars. The torsional mode has not been plotted as it is uncoupled from all other motions. The first branch named fluid wave is close to that representing a fluid wave in a rigid walled tube. The second branch named extensional wave is close to that representing the *in vacuo* shell wave at lower frequencies. These two branches are the only two real branches that exist at lower frequencies. The shell resonates as a ring with increasing frequency and the shell and the fluid motions become strongly coupled. Other branches seen in figure 2.5 belong to higher order modes, which have cut-on frequencies and are beyond the scope of this study.

Figure 2.6 shows typical dispersion curves for waves propagating with a circumferential modal order of *n=1* or the beam mode in a steel shell of *h/a=0.138*. The real solutions are shown as dots and the imaginary solutions are indicated with stars. Only one solution exists at lower frequencies, which corresponds to beam type shell motion and has been labeled as bending wave.

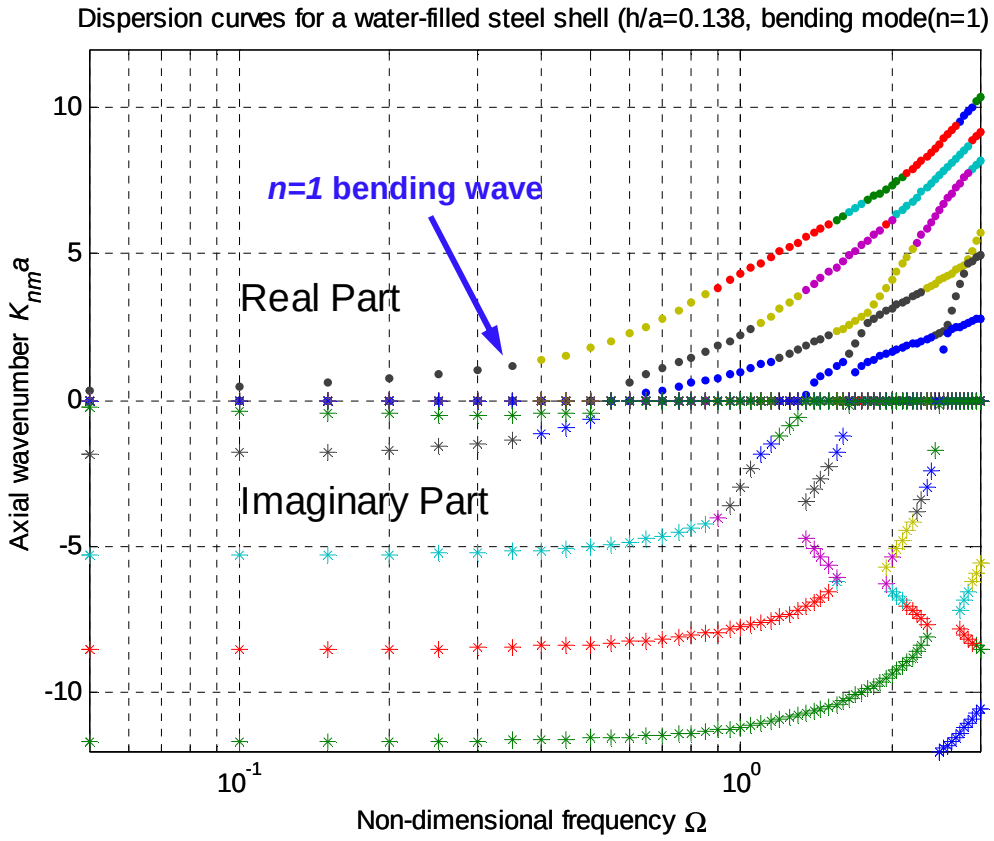

Figure 2.6. Dispersion curves for a water-filled steel shell of h/a=0.138 with n=1

The *n=0* shell displacement is independent of the circumferential angle θ. The wave speed for the *n=1* bending wave is given by:

$$c_b = \sqrt[4]{\frac{E_s I_s \omega^2}{m_a}} \tag{2.23}$$

where $I_s \approx \pi a^3 h$ is the second moment of inertia of the pipe cross-section and m_a is the mass per unit length of pipe cross-section and is given as $m_a = \rho_s 2\pi a h + \rho_f \pi a_i^2$. The wave speed for the bending wave is used in experimental determination of wave amplitudes, which will be discussed in detail in chapter 3. The cross-section of the pipe remains unchanged for the *n=0* and *n=1* modes. Higher order modes show lobar mode shapes and also exhibit a cut-on frequency, below which no real wavenumber solution exists. Approximate expressions for the *n=0* compressional wave, *n=1* bending wave, *n=0* torsional wave, and *n=0* fluid wave are given as:

$$k_l = \pm\Omega\sqrt{\left[1 + \frac{\nu^2(\Psi - 1)}{\left[(\Psi - 1)(1 - \nu^2) + 2\eta + \nu^2\right]}\right]} \tag{2.24}$$

$$k_b = \pm\sqrt{\Omega}\sqrt[4]{2 + \eta} \tag{2.25}$$

$$k_t = \pm\Omega\sqrt{\frac{2}{1 - \nu}} \tag{2.26}$$

$$k_f = \pm\Omega\sqrt{\left(\Psi + \frac{2\eta + \nu^2}{1 - \nu^2}\right)} \tag{2.27}$$

where $\eta = {}^{a\rho_f}\!/_{h\rho_s}$ is the fluid-shell mass ratio and $\Psi = \left({}^{c_l}\!/_{c_f}\right)^2$ is the speed factor. These wave numbers were derived by Pavic [56]. Figure 2.7 shows a plot of the wavenumbers mentioned above versus the non-dimensional frequency Ω. It should be noted that the dispersion curves plotted in figure 2.7 show only the real wavenumber solutions as these are the waves that carry energy along the system.

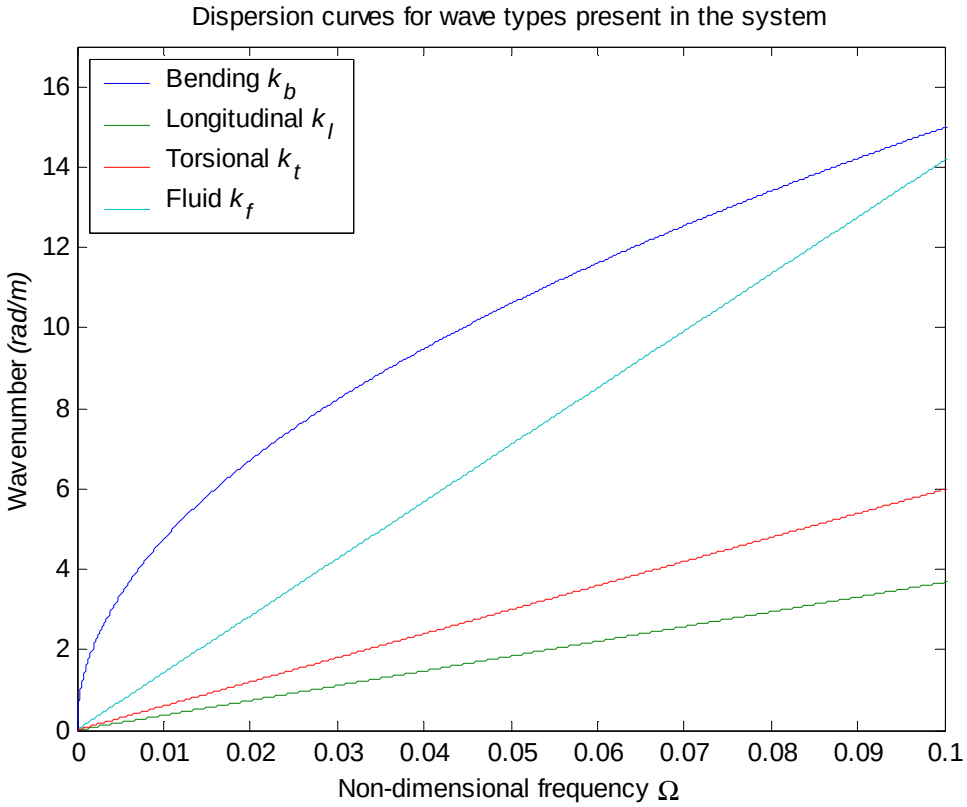

Figure 2.7. Dispersion curves of wave types that carry energy

The dispersion curves for the longitudinal wave and the fluid wave correspond to the curves seen in figure 2.5 and the dispersion curve for the bending wave corresponds to the curve seen in figure 2.6. The dispersion curves for a broad range of non-dimensional wavenumbers are presented in figures 2.5 and 2.6 and the dispersion curves presented in figure 2.7 can be considered as the zoomed in version of these previous plots for very low non-dimensional wavenumbers.

2.3. Energy flow

The equations that describe energy flow in a fluid-filled pipe have been derived by Fuller & Fahy [11] and by Pavic [56]. These equations will be reviewed and approximate equations that will later be employed to characterize the piping systems used for the work described here will be presented.

At small Mach numbers, where the effect of the flow is negligible, fluid-borne energy flow can be obtained by the integration of the time averaged acoustic intensity of the fluid wave, which is the product of the acoustic pressure and particle velocity, over the pipe cross-section:

$$P_{zf} = -\int_0^{2\pi}\int_0^{a_i} \langle p v_z \rangle r dr d\theta \tag{2.28}$$

where p denotes the acoustic pressure and v_z denotes the particle velocity. The particle velocity is related to the axial gradient of pressure via the Euler's equation presented in equation 10. Taking the Fourier transform of equation 2.28 will give us the following equation in the frequency domain:

$$\hat{p}_{zf}(z,\omega) = -\frac{1}{2\rho_f \omega}\int_0^{2\pi}\int_0^{a_i} \mathrm{Im}\left(\left(\frac{\partial \hat{p}}{\partial z}\right)^* \hat{p}\right) r dr d\theta \tag{2.29}$$

where the karat denotes Fourier amplitudes and * denotes the complex conjugate.

The axial energy flow can be described using the axial component of the structural intensity vector. The axial structural intensity of a thin shell consists of the contributions of longitudinal extension ($N_z \dot{u}$), tangential shear ($N_{z\theta} \dot{v}$), radial shear ($Q_z \dot{w}$), bending

($M_z\left(\partial\dot{w}/\partial z\right)$) and twisting ($M_{z\theta}\left(\dot{v}-\partial\dot{w}/\partial\theta\right)/a$). The spectrum of the structure-borne energy flow is given by:

$$\hat{P}_{zs}(z,\omega)=\frac{\omega}{2}\int_0^{2\pi}\mathrm{Im}\left(\hat{N}_z^*\hat{u}+\hat{N}_{z\theta}^*\hat{v}+\hat{Q}_z^*\hat{w}+\hat{M}_z^*\frac{\partial\hat{w}}{\partial z}+\hat{M}_{z\theta}^*\frac{1}{a}\left(\hat{v}-\frac{\partial\hat{w}}{\partial\theta}\right)\right)ad\theta \tag{2.30}$$

The three latter parameters are proportional to the shell thickness parameter and therefore are negligible for the low-frequency behavior of pipes. Using Donnell-Mushtari equations the first two terms can be written in terms of the shell mean radius displacement as:

$$N_z=\frac{E_s h}{1-\nu^2}\left(\frac{\partial u}{\partial z}+\nu\left(\frac{1}{a}\frac{\partial v}{\partial\theta}+\frac{w}{a}\right)\right) \tag{2.31}$$

$$N_{z\theta}=\frac{E_s h}{2(1-\nu)}\left(\frac{\partial v}{\partial z}+\frac{1}{a}\frac{\partial u}{\partial\theta}\right) \tag{2.32}$$

The total axial energy flow can be found from the summation of the structure-borne energy flow and fluid-borne energy flow over the circumferential and axial modes. The total axial energy flow can be expanded in circumferential modes as:

$$\hat{P}_z=\sum_n\left(\left(\hat{P}_{zs}\right)_n+\left(\hat{P}_{zf}\right)_n\right) \tag{2.33}$$

Structure borne energy flow per mode can be determined experimentally if the system can be excited in such a way so that only one wave type is excited. The spatial derivatives that exist in equation 2.30 can be approximated by a finite difference method and the approximate equations are given as:

$$\left(P_{zs}\right)_L=\frac{1}{\zeta_s^{\,2}}\frac{\pi aD}{\omega^3\Delta z}\mathrm{Im}\left[S\left(\ddot{u}_0(z_1),\ddot{u}_0(z_2)\right)\right] \tag{2.34}$$

$$\left(P_{zf}\right)_F = \frac{2}{\left(\zeta_f^2 - \Psi\right)^2} \frac{\pi a^2 \rho_f c_L^2}{\omega^3 \Delta z} \mathrm{Im}\left[S\left(\ddot{w}_0(z_1), \ddot{w}_0(z_2)\right)\right] \tag{2.35}$$

$$\left(P_{zs}\right)_T = \frac{1-\nu}{2} \frac{\pi a D}{\omega^3 \Delta z} \mathrm{Im}\left[S\left(\ddot{\upsilon}_0(z_1), \ddot{\upsilon}_0(z_2)\right)\right] \tag{2.36}$$

$$\left(P_{zs}\right)_B = \pi a h E_s \left(1 - k_B^2\right) \frac{k_B^2}{\omega^3 \Delta z} \mathrm{Im}\left[S\left(\ddot{w}_1(z_1), \ddot{w}_1(z_2)\right)\right] \tag{2.37}$$

In these equations $\Psi = \left(c_L / c_F\right)^2$ and $k_B^2 = \sqrt{(2+\eta)\cdot\Omega}$. c_L and c_F are the speeds of the longitudinal and fluid waves, respectively. η is the fluid-shell mass ratio and ρ_F is the density of the fluid. E_s is the Young's modulus for the shell. Non-dimensional frequency is Ω and ζ_S & ζ_F are wave number factors and are expressed as:

$$\zeta_s = \sqrt{\left[1 + \frac{\nu^2(\Psi - 1)}{\left[(\Psi - 1)(1 - \nu^2) + 2\eta + \nu^2\right]}\right]} \tag{2.38}$$

$$\sqrt{\left(\Psi + \frac{2\eta + \nu^2}{1 - \nu^2}\right)} \tag{2.39}$$

where ν is Poisson's ratio and $\eta = a\rho_f / h\rho_s$ is the fluid-shell mass ratio. The S in equations 2.34-2.37 denotes the cross spectral density (explained in measurement methods) between axial locations z_1 and z_2. The reader is encouraged to refer to Verheij [32] for further reference.

Chapter 3

Measurement Methods

This chapter describes the measurement techniques used in this study. The processing of time domain data to obtain modal acceleration signals and the vibro-acoustic energy flow is described.

The wave decomposition technique is the estimation of complex amplitude spectra of the separate wave types present in the system from acceleration signals and pressure fluctuations. The decomposition method uses the governing equations of the system described in section 2. Through decomposition the positive and negative traveling wave amplitudes can be determined and quantities like energy flow through a section can be calculated, thus yielding a realistic understanding of the physical system.

The wave decomposition methods provide the means to analyze the fluid-filled piping system and the discontinuities that can be encountered on the system. Through wave decomposition passive components can be characterized and their interaction with the traveling wave types investigated.

3.1. Theoretical basis

The theoretical basis behind the wave decomposition methods is described in this section. Firstly, the decomposition of measured signals to obtain circumferential modes

will be described, followed by a discussion of axial wave decomposition. Description of the methods used in wave decomposition and their robustness to measurement errors will be given. The chapter concludes with the presentation of experimental results and validation of decomposition methods.

3.1.1. Wave decomposition

Chapter two showed that the model solutions to the vibration of a fluid-filled pipe can be decomposed into independent circumferential modes (*n=0, 1...*) where multiple axial modes (*m=1, 2...*) may exist for each circumferential mode n. Many of the waves associated with these modes are near-field waves and must be considered when evaluating pipes of short lengths or discontinuities. Wave decomposition can be restricted to a limited number of waves that carry energy along the system (when applied at locations greater than one diameter away from source where wave amplitude decays with e^{kz}). For this study, these waves are well below the ring frequency. It is assumed that waves associated with higher order modes (modes that have a cut-on frequency) do not interact with waves that carry energy.

3.1.1.1. Circumferential wave decomposition

By applying an array of transducers to the pipe enough information can be measured to allow the decomposition method to be successfully applied. The orthogonal displacement variables can be written as:

$$q(z,\theta,\omega)=\sum_{n=0}^{\infty} q_n(z,\omega)\cos(n\theta+\alpha_n(z,\omega)) \qquad (3.1a)$$

which, for our case, can be simplified to:

$$q(z,\theta,\omega) = q_0(z,\omega) + q_1(z,\omega)\cos(\theta + \alpha(z,\omega)) \qquad (3.1b)$$

The two amplitudes q_0, q_1 and the polarization angle α can be obtained from the signals output by four accelerometers in a pipe cross-section. The circumferential positions for the array of accelerometers were determined as $\theta_a = 0^\circ, \theta_b = 90^\circ, \theta_c = 180^\circ, \theta_d = 270^\circ$ (shown in figure 3.1). These positions allow the signals to be decomposed using simple subtractions or additions of transducer signals. These operations can be performed in real time by using analog circuits or digitally during the post-processing of data.

3.1.1.2. Transducer placement

The wave decomposition procedures in this study make use of a combination of accelerometers and pressure transducers. The accelerometers were placed on brass studs mounted on the pipe at regular intervals and at ninety degree angles (figure 3.1). Verheij [35] has established methods for selection of accelerometers with matched sensitivities and phase characteristics. The mounting of the accelerometers in radial, tangential, and axial directions allows us to acquire the wave type of interest. Application of piezo-electric transducers have been analyzed by Briscoe and Pinnington [38]. PVDF film strips were used to sense the breathing mode, but this approach was discarded as these sensors can only detect the *n=0* acoustic wave or waves associated with the *n=0* breathing mode in the shell depending on the pipe physical characteristics. However, the application of PVDF sensors is easy and allows for measurements where intrusion is not possible.

Figure 3.1. Sensor positions and placement

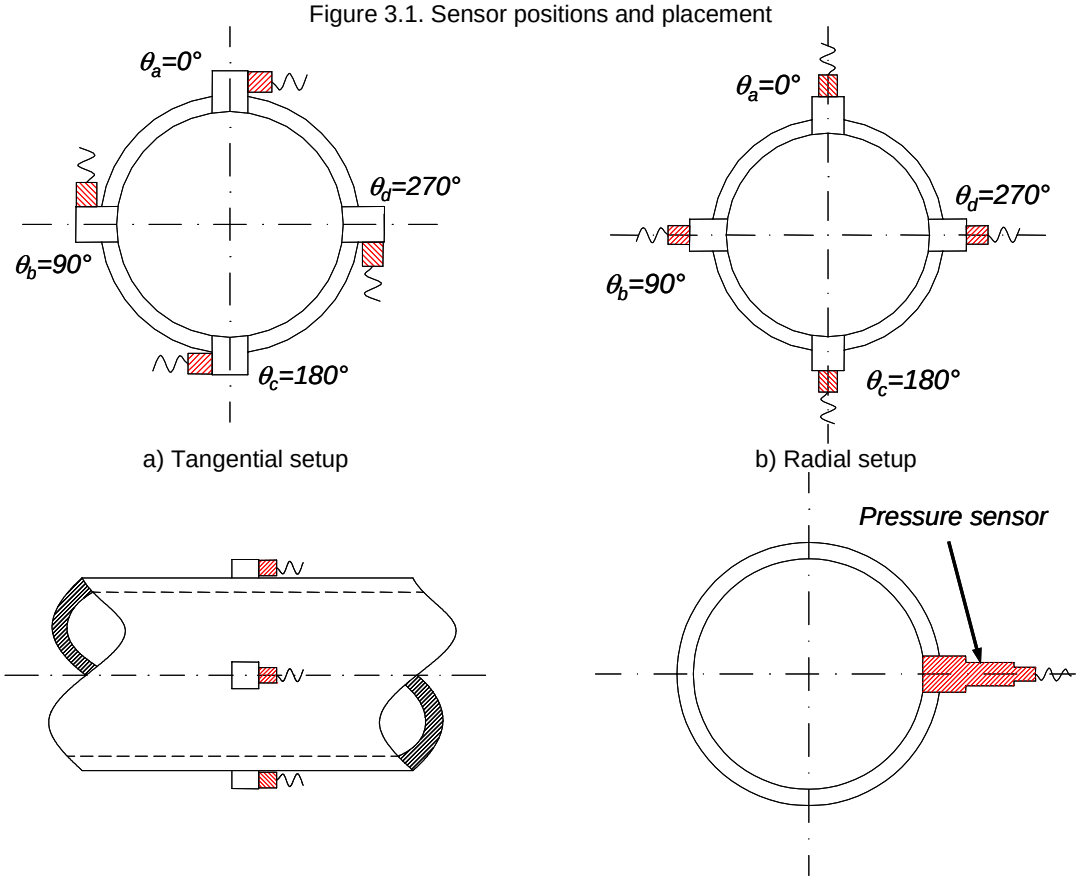

The pressure sensors were mounted flush with the pipe wall inner surface (figure 3.1d). Since the acoustic wave propagates as a plane wave in the frequency range of interest, application of one transducer per pipe cross-section was adequate. Four accelerometers were used to acquire shell displacement signals. Accelerometers mounted perpendicular to the pipe axis, are in phase for the *n=0* breathing mode, hence their signals can be summed. The accelerometers at opposing sides of the pipe are out-of-phase for the *n=1* bending mode. The polarization angle for the *n=1* bending mode can also be determined from this application. The accelerometers placed as shown in figure 3.1a to acquire torsional displacements and accelerometers placed as shown in figure 3.1c to acquire axial displacements will be in-phase. Hence these signals can be summed to obtain a single signal that can later be used in axial wave decomposition.

The following equations are used in circumferential decomposition to obtain accelerations in the axial (*u*), tangential (*v*), and radial (*w*) directions:

$$\ddot{u}_0 = \tfrac{1}{4}\left(\ddot{u}_a + \ddot{u}_b + \ddot{u}_c + \ddot{u}_d\right) \tag{3.2}$$

$$\ddot{v}_0 = \tfrac{1}{4}\left(\ddot{v}_a + \ddot{v}_b + \ddot{v}_c + \ddot{v}_d\right) \tag{3.3}$$

$$\ddot{w}_0 = \tfrac{1}{4}\left(\ddot{w}_a + \ddot{w}_b + \ddot{w}_c + \ddot{w}_d\right) \tag{3.4}$$

$$\ddot{w}_1 \cos(\alpha) = \tfrac{1}{2}\left(\ddot{w}_a - \ddot{w}_c\right) \qquad \ddot{w}_1 \sin(\alpha) = \tfrac{1}{2}\left(\ddot{w}_b - \ddot{w}_d\right) \tag{3.5}$$

In these equations α denotes the polarization angle, the subscript 0 denotes the *n=0* waves and the subscript 1 denotes the *n=1* bending wave.

3.1.1.3. Axial wave decomposition

The axial modes corresponding to the circumferential orders *n=0,1* can be obtained once the circumferential modes are decomposed by selecting appropriate accelerometer configurations at selective axial positions along the pipe. The modal amplitude for generalized displacement variable can be expressed in the form:

$$q_n(z,\omega) = \sum_{m=1}^{M} A_{nm}^{+}(\omega) e^{-ik_{nm}z} + A_{nm}^{-}(\omega) e^{ik_{nm}z} \tag{3.6}$$

where k_{nm} denotes the axial wavenumber. The complex wave amplitudes of the positive and negative traveling waves can be estimated by taking measurements at a minimum of two axial locations. The simplest form of amplitude estimation can be accomplished by taking measurements at two locations. This method does not take into account the coupling between different wave types. More measurements can be included to get a better understanding of the system. These methods will be discussed in later sections.

The relationship between measurements and wave amplitudes can be expressed in the simplest form as:

$$\{Q\} = [W]\{A\} \tag{3.7}$$

where the vector {*Q*} represents the measurements and the vector {*A*} represents the wave amplitudes. The coefficients of the wave decomposition matrix [*W*] will be determined from the wave propagation model, the number of waves included, and the physical locations of the transducers used in wave decomposition. The matrix [*W*] can be inverted to determine {*A*} provided that the matrix is not singular. The limitations of this approach will be discussed in later sections.

3.1.2. Two-channel method

The two channel method applies to all uncoupled waves in the system. This method was originally developed to determine acoustic waves in a duct by Chung and Blazer [29]. In fluid-filled pipes it is always valid for torsional waves, as these waves are uncoupled from the other wave types in the system. It also valid for bending waves at positions sufficiently far from discontinuities. The compressional waves in the shell and the plane waves in the fluid are coupled through Poisson contraction.

The two channel method involves two measurements of transfer functions between a reference sensor and transducer arrays located at two distinct axial positions z_1 and z_2. The equation for the two channel method in matrix form can be expressed as:

$$\begin{Bmatrix} q_{nm}(z_1) \\ q_{nm}(z_2) \end{Bmatrix} = \begin{bmatrix} e^{-ik_{nm}l_1} & e^{ik_{nm}l_1} \\ e^{-ik_{nm}l_2} & e^{ik_{nm}l_2} \end{bmatrix} \begin{Bmatrix} a_{nm}^{+} \\ a_{nm}^{-} \end{Bmatrix} \tag{3.8}$$

The wave amplitudes can be calculated via matrix inversion:

$$\begin{Bmatrix} a_{nm}^{+} \\ a_{nm}^{-} \end{Bmatrix} = -\frac{1}{2i\omega^2 \sin(k_{nm}\Delta)} \begin{bmatrix} e^{ik_{nm}l_2} & -e^{ik_{nm}l_1} \\ -e^{-ik_{nm}l_2} & e^{ik_{nm}l_1} \end{bmatrix} \begin{pmatrix} q_{nm}(z_1) \\ q_{nm}(z_2) \end{pmatrix} \tag{3.9}$$

where $\Delta = z_2 - z_1$ and l denotes the distance of the axial position to the reference sensor. The matrix will be singular when the transducer spacing is equal to zero or to multiples of half-wavelength, hence, making matrix inversion impossible. The accuracy of the wave amplitudes depends on the accuracy of the measurements (amplitude and phase), the accuracy by which the wave numbers are estimated, and the positioning of the transducer arrays.

The energy flow in each propagating wave can be expressed in terms of wave amplitudes as:

$$P_{nm}(\omega) = C_{nm}(\omega)\tfrac{1}{2}\left(\left|a_{nm}^{+}\right|^2 - \left|a_{nm}^{-}\right|^2\right) \tag{3.10}$$

where $C_{nm}(\omega)$ is a constant that depends on the type of transducer and the specific impedance of the wave type.

3.1.3. Cross-spectral density method

We can relate various wave descriptors to the auto and cross spectra that can be obtained from two-channel FFT analysis:

$$G_{11}(\omega) = \tfrac{1}{2} E\left[q_{nm}^{*}(z_1,\omega), q_{nm}(z_1,\omega)\right] \tag{3.11}$$

$$G_{12}(\omega) = \tfrac{1}{2} E\left[q^{*}_{nm}(z_1,\omega), q_{nm}(z_2,\omega)\right] \quad (3.12)$$

where the expected value is determined by averaging over a number of spectra and * denotes complex conjugate.

This method of measuring vibro-acoustic intensity supposes that the difference of the squared wave amplitudes is proportional to the imaginary part of the measured cross spectrum. The spectrum of the time averaged energy flow can be expressed as:

$$P_{nm}(\omega) = -\frac{C_{nm}(\omega)}{\sin(k_{nm}\Delta)} \mathrm{Im}[G_{12}(\omega)] \quad (3.13)$$

The simplified expressions for energy flow per wave type were presented in section 2.3.

3.1.4. Multi-channel methods

Wave types become coupled in short pipes and when waves encountering discontinuities. Therefore, it is necessary to include the coupling in the wave decomposition. This section will describe multi-channel methods that decompose multiple wave types simultaneously.

First the four channel method and its application to the analysis of coupled *n=0* acoustic waves and *n=0* compressional shell waves is presented. This method makes use of two accelerometer arrays and two pressure transducers. The relationship of acquired signals to the traveling wave amplitudes can be expressed as:

$$\begin{Bmatrix} \tilde{p}(z_1) \\ \tilde{p}(z_4) \\ \tilde{u}(z_2) \\ \tilde{u}(z_3) \end{Bmatrix} = \begin{bmatrix} e^{-ik_f l_1} & e^{ik_f l_1} & \Psi_e e^{-ik_l l_1} & -\Psi_e e^{ik_l l_1} \\ e^{-ik_f l_2} & e^{ik_f l_2} & \Psi_e e^{-ik_l l_2} & -\Psi_e e^{ik_l l_2} \\ \Psi_f e^{-ik_f l_3} & -\Psi_f e^{ik_f l_3} & e^{-ik_l l_3} & e^{ik_l l_3} \\ \Psi_f e^{-ik_f l_4} & -\Psi_f e^{ik_f l_4} & e^{-ik_l l_4} & e^{ik_l l_4} \end{bmatrix} \begin{Bmatrix} a_f^+ \\ a_f^- \\ a_l^+ \\ a_l^- \end{Bmatrix} \tag{3.14}$$

where $\tilde{p} = p/\rho_f c_f \omega$ and $\tilde{u} = -\ddot{u}/\omega^2$. The coefficients of coupling are given by:

$$\Psi_e = \frac{\pm i\tilde{\nu}\breve{k}_f \breve{k}_l^2}{k_l\left(k_l^2 - \breve{k}_f^2\right)} \qquad \text{and} \qquad \Psi_f = \frac{\pm i\sigma\tilde{\nu}k_f \breve{k}_f}{k_f^2 - \breve{k}_l^2} \tag{3.15}$$

where $\tilde{\nu} = 2\nu/a_i$ and $\sigma = \frac{A_f k_f}{A_s E_s}\left(1 + 2\frac{a}{h}\frac{k_f}{E_s}\right)^{-1}$. The frequency independent factors (Ψ_e, Ψ_f) contain both the exact solutions (k_f, k_l) of the dispersion equation and the approximate solutions ($\breve{k}_f, \breve{k}_l$) as defined in chapter 2. The latter are used to scale the data and Poisson coupling is responsible for the small difference between the two. The two wave types analyzed have different wave velocities. The elements of the inversion matrix will change depending on the waves being analyzed. The first two elements of the measurement vector can also be acceleration measurements, in which case the coefficients of the coupling will need to be changed.

Another method that will be analyzed is called the ten-channel method. This method incorporates all the analyzed wave types (*n=0* fluid, *n=0* compressional, *n=0* torsional, *n=1* bending) plus the effect of the near field. This method in matrix form can be expressed as:

$$\begin{pmatrix} p(\omega,z_1)/\psi_1 \\ p(\omega,z_4)/\psi_1 \\ a_u(\omega,z_2)/\psi_2 \\ a_u(\omega,z_3)/\psi_2 \\ a_w^0(\omega,z_2)/\psi_2 \\ a_w^0(\omega,z_3)/\psi_2 \\ a_w^1(\omega,z_2)/\psi_2 \\ a_w^1(\omega,z_3)/\psi_2 \\ a_v(\omega,z_2)/\psi_2 \\ a_v(\omega,z_3)/\psi_2 \end{pmatrix} = \begin{bmatrix} e^{-ik_f l_1} & e^{ik_f l_1} & e^{-ik_l l_1}\chi_{uf}/\psi_1 & e^{ik_l l_1}\chi_{uf}/\psi_1 & e^{-ik_b l_1}\chi_{bf}/\psi_1 & e^{ik_b l_1}\chi_{bf}/\psi_1 & 0 & 0 \\ e^{-ik_f l_4} & e^{ik_f l_4} & e^{-ik_l l_4}\chi_{uf}/\psi_1 & e^{ik_l l_4}\chi_{uf}/\psi_1 & e^{-ik_b l_4}\chi_{bf}/\psi_1 & e^{ik_b l_4}\chi_{bf}/\psi_1 & 0 & 0 \\ e^{-ik_f l_2}\chi_{fu}\psi_1 & e^{ik_f l_2}\chi_{fu}\psi_1 & e^{-ik_l l_2} & e^{ik_l l_2} & e^{-ik_b l_2}\chi_{bup} & e^{ik_b l_2}\chi_{bup} & 0 & 0 \\ e^{-ik_f l_3}\chi_{fu}\psi_1 & e^{ik_f l_3}\chi_{fu}\psi_1 & e^{-ik_l l_3} & e^{ik_l l_3} & e^{-ik_b l_3}\chi_{bup} & e^{ik_b l_3}\chi_{bup} & 0 & 0 \\ e^{-ik_f l_2}\chi_{fb}\psi_1 & e^{ik_f l_2}\chi_{fb}\psi_1 & e^{-ik_l l_2}\chi_{ub} & e^{ik_l l_2}\chi_{ub} & 0 & 0 & 0 & 0 \\ e^{-ik_f l_3}\chi_{fb}\psi_1 & e^{ik_f l_3}\chi_{fb}\psi_1 & e^{-ik_l l_3}\chi_{ub} & e^{ik_l l_3}\chi_{ub} & 0 & 0 & 0 & 0 \\ 0 & 0 & 0 & 0 & e^{-ik_b l_2} & e^{ik_b l_2} & 0 & 0 \\ 0 & 0 & 0 & 0 & e^{-ik_b l_3} & e^{ik_b l_3} & 0 & 0 \\ 0 & 0 & 0 & 0 & e^{-ik_b l_2}\chi_{bv} & e^{ik_b l_2}\chi_{bv} & e^{-ik_t l_2} & e^{ik_t l_2} \\ 0 & 0 & 0 & 0 & e^{-ik_b l_3}\chi_{bv} & e^{ik_b l_3}\chi_{bv} & e^{-ik_t l_3} & e^{ik_t l_3} \end{bmatrix} \begin{Bmatrix} A_p^+ \\ A_p^- \\ A_l^+ \\ A_l^- \\ A_b^+ \\ A_b^- \\ A_t^+ \\ A_t^- \end{Bmatrix}$$

(3.16)

where the subscripts denote transducer arrangement and superscripts denote the mode number. The amplitudes for each traveling wave can be calculated by pseudo matrix inversion. The coupling coefficients in equation 3.16 are:

$$\psi_1 = \rho_f \,\omega^2/k_f\,, \qquad \psi_2 = -\omega^2\,, \qquad \chi_{uf} = -\frac{2\rho_f c_l^2}{a_0\left(\Psi-\zeta_s^2\right)}\frac{\Omega}{i\nu\zeta_s\left(\zeta_s^2-1\right)},$$

$$\chi_{bf} = \frac{2\rho_f c_l^2\Omega^2}{\zeta_b a_0}\,, \qquad \chi_{fu} = -\frac{i\nu\zeta_f}{\left(\zeta_f^2-1\right)\Omega}\frac{a_0\left(\Psi-\zeta_f^2\right)}{2\rho_f c_l^2}\,, \qquad \chi_{bup} = -\frac{ik_b\left(1-\nu k_b^2\right)}{\left(1+k_b^2\right)^2}\,, \qquad (3.17)$$

$$\chi_{fb} = \frac{a_0^2}{E_s h}\,, \qquad \chi_{ub} = \frac{\Omega}{i\nu\zeta_s\left(\zeta_s^2-1\right)}\,, \qquad \chi_{bv} = -\left(1+\nu k_b^2\right)$$

Although it requires more measurements, the accuracy is better than the two-channel method. It should be noted that if the system were to have air as the fluid, the results would be the same as the two-channel method, because no fluid-shell coupling exists and each wave type is independent of the other wave types. The limitations of the decomposition methods presented will be discussed in detail at the end of this chapter.

3.2. Validation of measurement methods

This section presents the validation for various decomposition methods and where these measurements can be used is discussed.

Very large condition numbers indicate that a matrix is close to being singular. The decomposition methods are inaccurate near any singularity of the decomposition matrix. Hence, high values for condition numbers show regions where decomposition is not effective. Figures 3.2, 3.3, and 3.4 show the variation of condition numbers for various decomposition methods presented above.

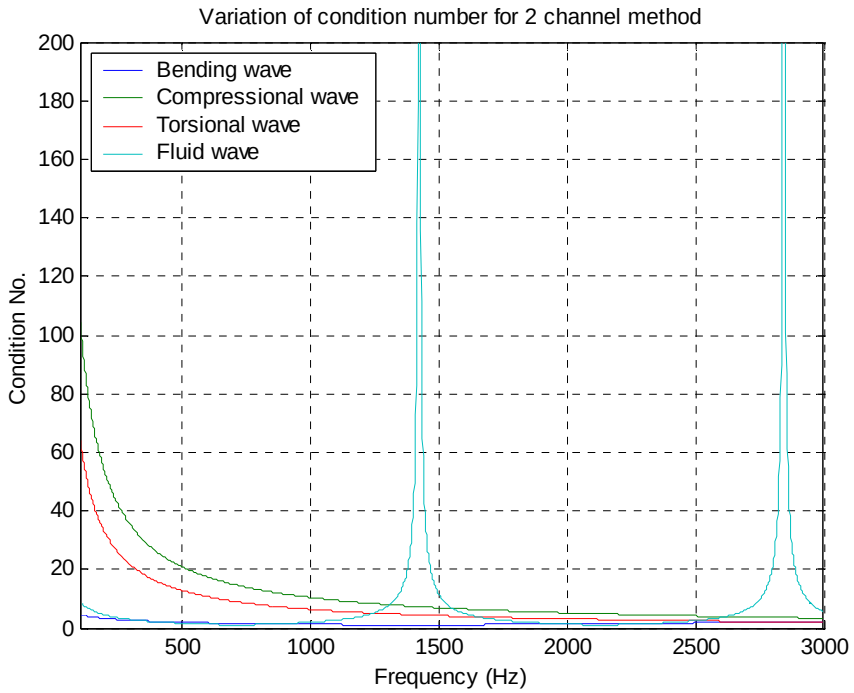

Figure 3.2. Condition number plot for all wave types using two channel method

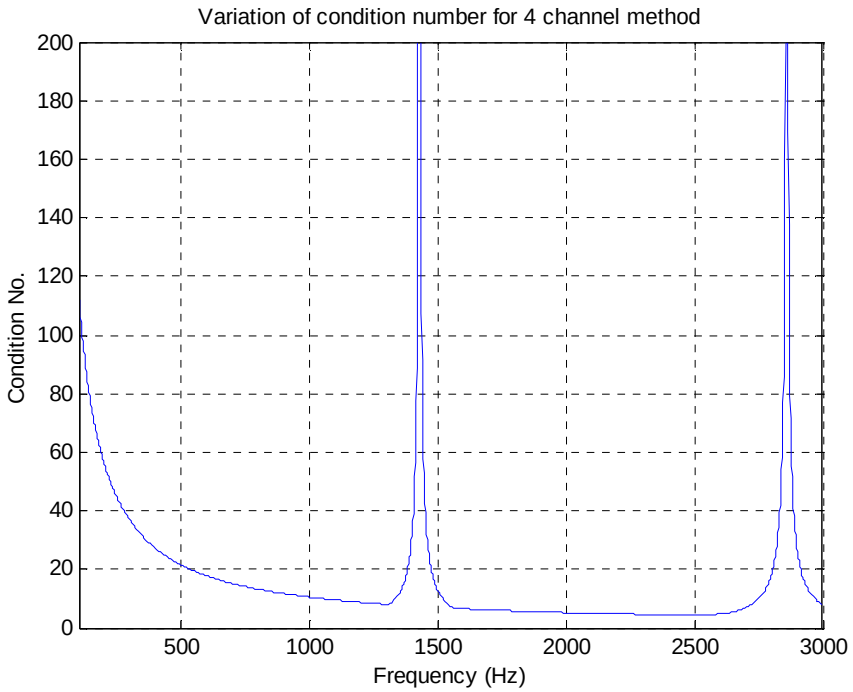

Figure 3.3. Condition number plot for four channel method

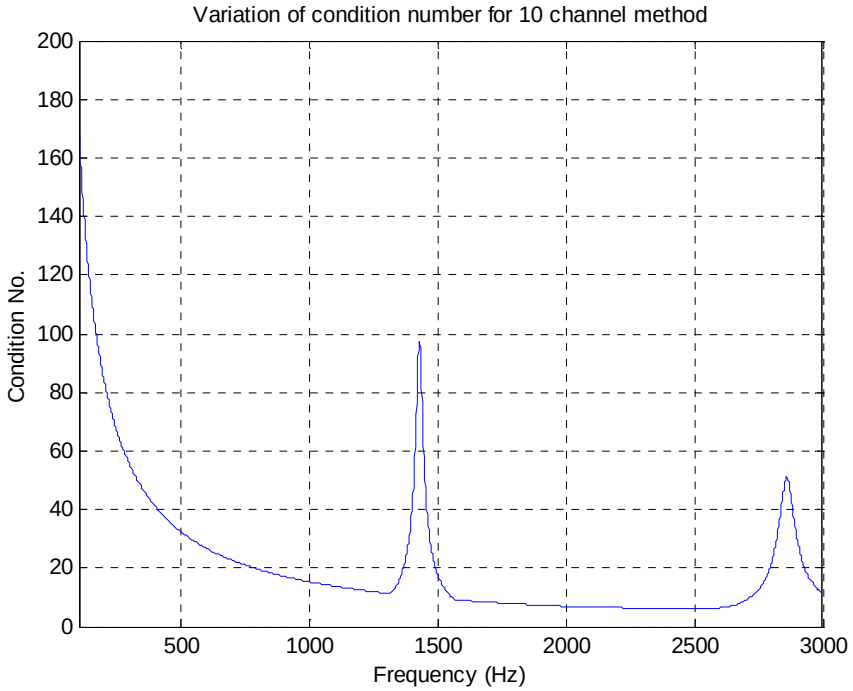

Figure 3.4. Condition number plot for ten channel method

Wave decomposition uses the phase difference of a traveling wave arriving at two distinct transducer locations to determine the amplitudes of positive and negative traveling waves. At low frequencies the wavelength of traveling waves are too large compared to transducer spacing so the signals are almost the same. The matrix rank is close to 1 and the decomposition matrix becomes singular. Therefore wave decomposition is not very effective at low frequencies.

A comparison of four-channel and ten-channel methods show that the four-channel method is more reliable at low frequencies due to lower condition numbers of the four-channel decomposition matrix compared with the ten-channel decomposition matrix, while the ten-channel method reduces the peaks of condition numbers at *1427 Hz* and *2846 Hz*. Singularities occur when the transducer spacing of pressure sensors is equal to multiples of one half the fluid wavelengths. The condition numbers for the two channel method for the wave types studied show that only the decomposition matrix for the fluid wave has a singularity at higher frequencies for our frequency range of interest. The most reliable results are for the decomposition of the bending wave.

Condition numbers for decomposition matrices are directly affected by sensor positioning. In general, the larger the spacing, the lower the frequency of the first singularity in the decomposition matrix. However, closer spacing of sensors will make the decomposition susceptible to errors at low frequency resulting from phase matching. A compromise based on the quality of available transducers and the frequency range of interest should be found.

Figure 3.5 shows the condition numbers for decomposition matrices with different transducer spacing. Singularities at *870 Hz*, *1740 Hz*, and *2610 Hz* correspond to

multiples of one half acoustic wavelengths. The last two columns of the decomposition matrix which correspond to the torsional wave are identical at the singularity of *2061 Hz*.

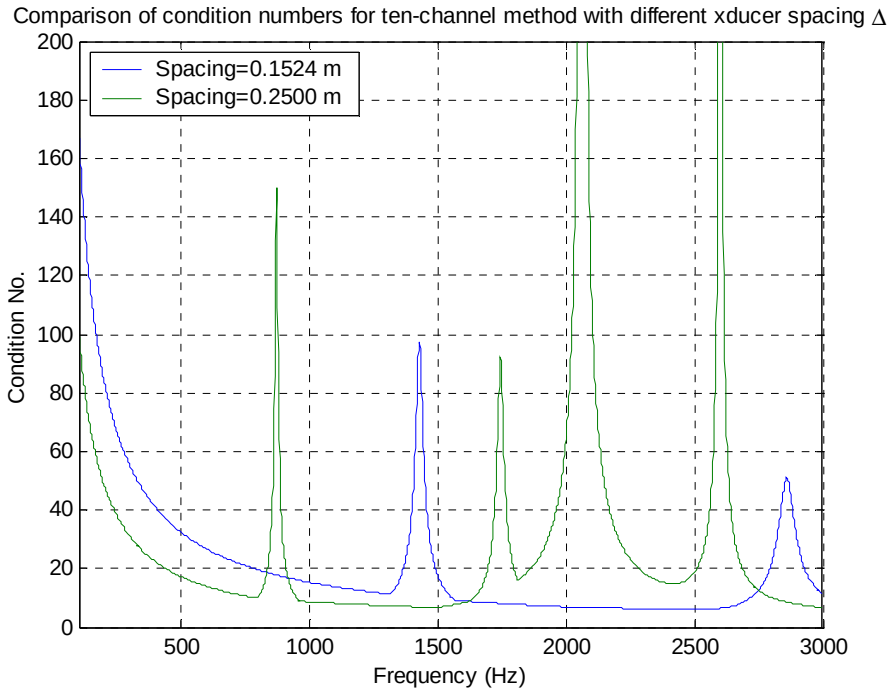

Figure 3.5. Comparison of condition numbers for different sensor placements

An important way of validating results obtained through wave decomposition is the insertion of simulated phase mismatch between transducer arrays. Transducer arrays are lined up as shown in section 3.1.1.2 for each of the wave types present in a fluid filled pipe. A phase mismatch of ±*20°* was applied during the post processing of data to the first elements of transducer arrays and the deviation of Fourier amplitudes from nominal results were observed. It should be noted that this mismatch of *20°* is far greater than phase mismatches that would normally be encountered during experimentation.

Figures 3.6 through 3.10 show the changes in Fourier amplitudes when a phase mismatch of $e^{\pm i\theta}$ is applied sequentially to transducer arrays. The results are compliant with what should be expected from a coupled system:

Phase mismatch in transducer arrays that pick up the *n=1* longitudinal wave yield changes in the calculation of Fourier amplitudes for the *n=0* fluid wave as well as the amplitudes of the *n=1* longitudinal wave.

Phase mismatch in pressure sensors that pick up the *n=0* fluid wave yield changes in the calculation of Fourier amplitudes for the *n=0* longitudinal wave as well as the amplitudes of the *n=0* fluid wave.

Phase mismatch in transducer arrays that pick up the *n=1* bending wave will show up in calculations of Fourier amplitudes for all wave types present in the system. While the bending wave does not carry the highest energy in the system, the motion of the shell for this particular wave is higher than the other waves present in the shell. Thus a small error will be multiplied and the result is large discrepancies in the calculated amplitudes from the ideal sensor case.

Phase mismatch in transducer arrays that pick up the *n=0* torsional wave will show up only in calculations of Fourier amplitudes for *n=0* torsional wave. The deviations in amplitudes of other wave types caused by mismatch in these transducer arrays are negligible.

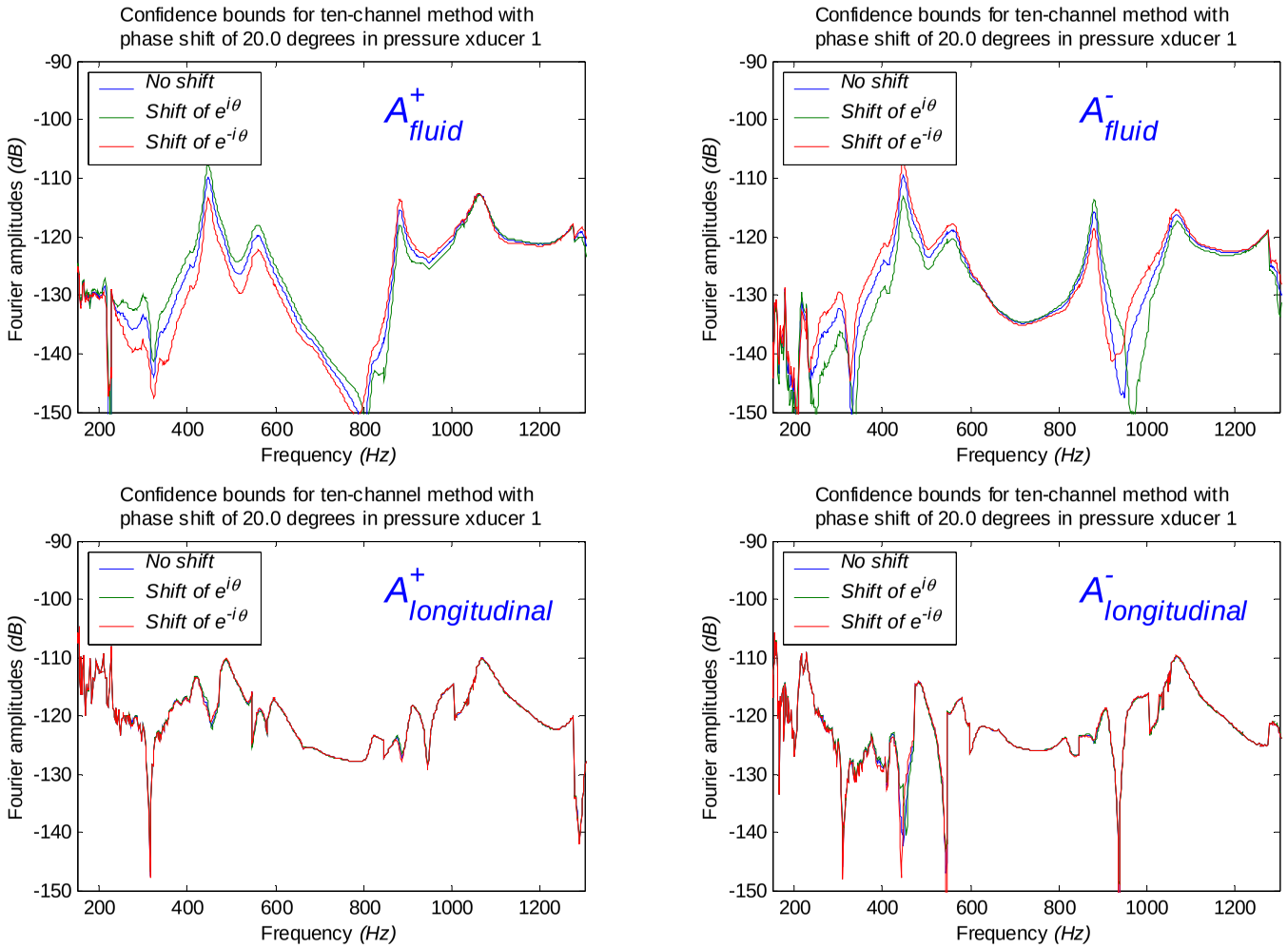

Figure 3.6. Confidence Bounds for n=0 fluid wave and n=0 longitudinal wave with a phase mismatch in pressure sensors

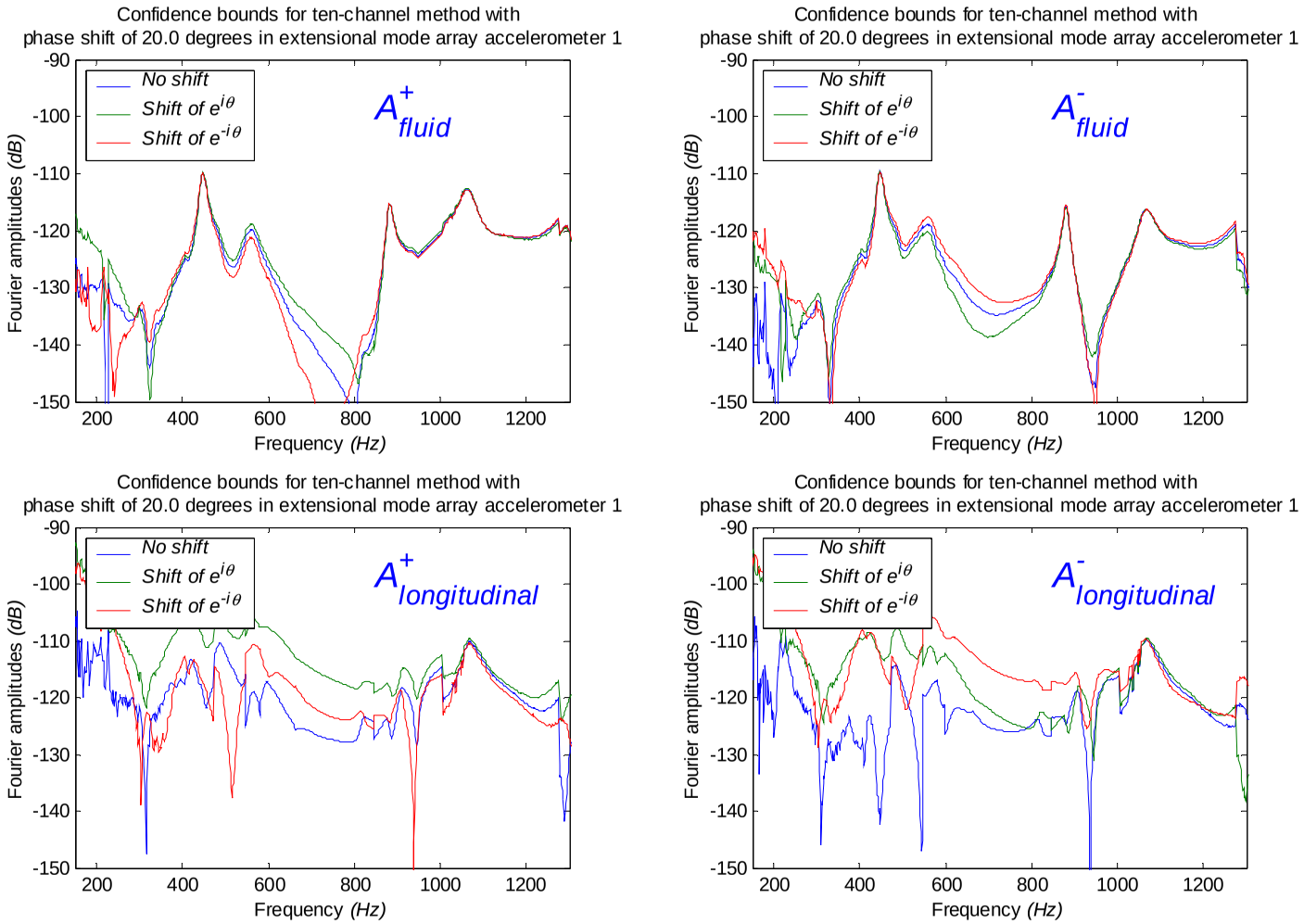

Figure 3.7. Confidence Bounds for n=0 fluid wave and n=0 longitudinal wave with a phase mismatch in longitudinal accelerometer arrays

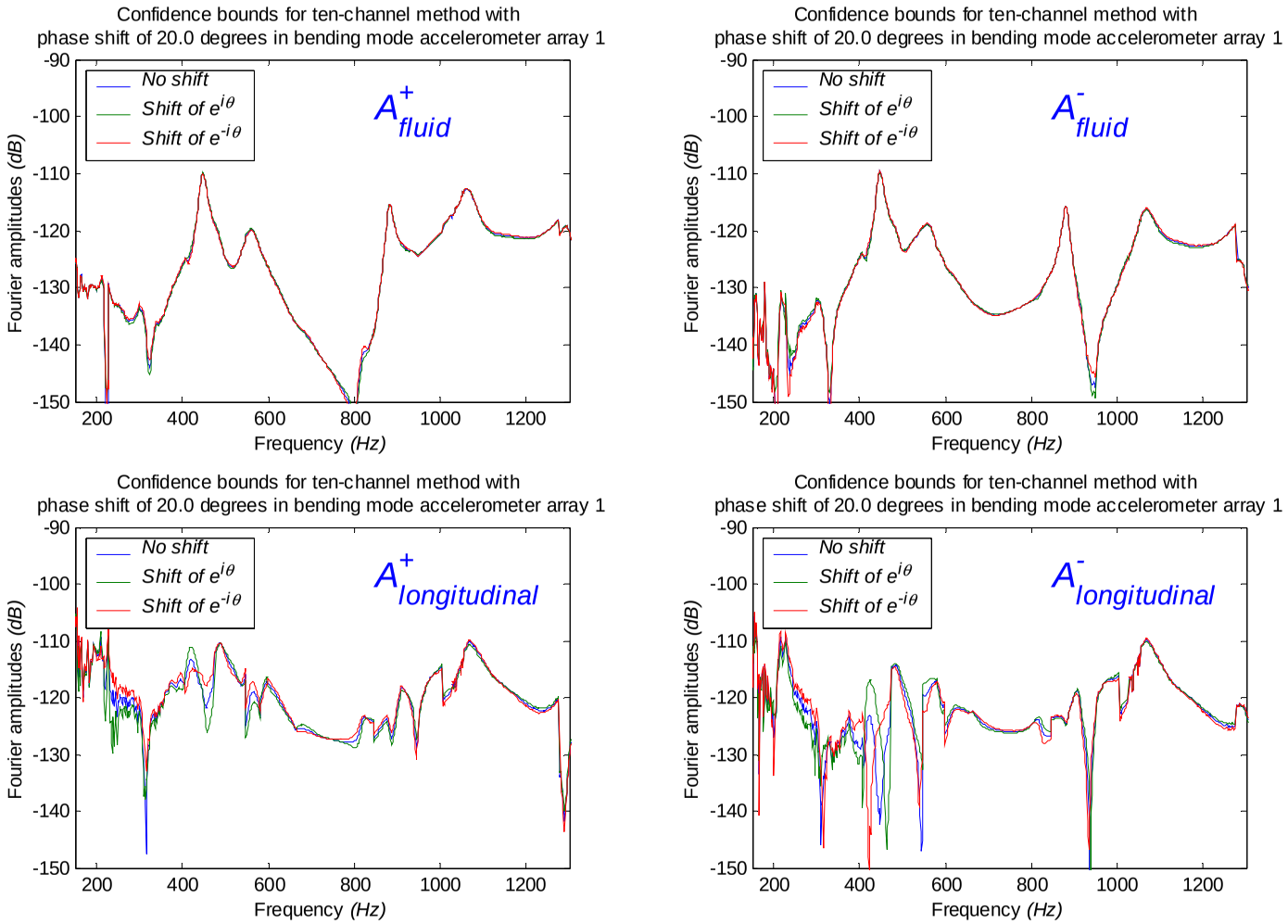

Figure 3.8. Confidence Bounds for n=0 fluid wave and n=0 longitudinal wave with a phase mismatch in bending accelerometer arrays

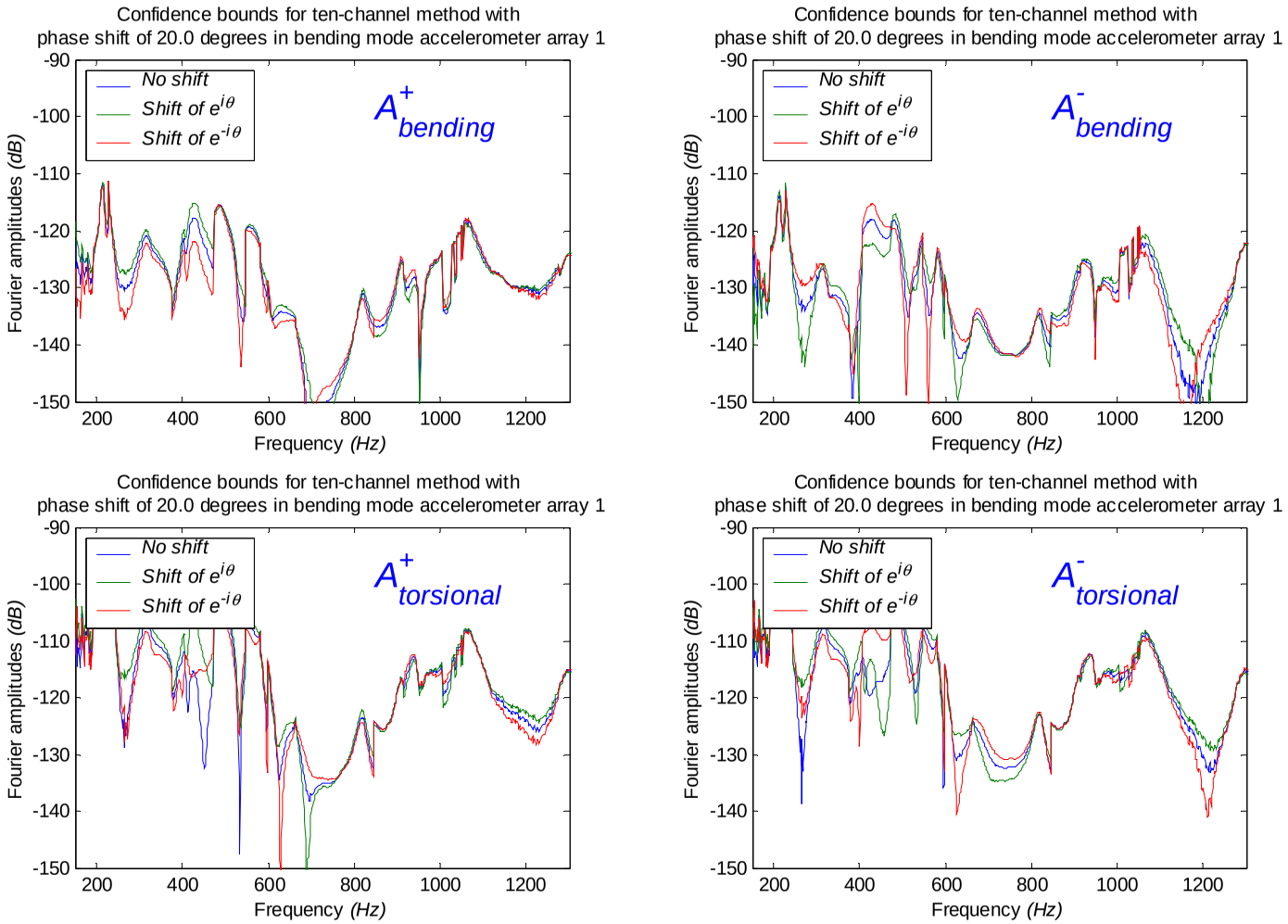

Figure 3.9. Confidence Bounds for n=0 torsional wave and n=1 bending wave with a phase mismatch in bending accelerometer arrays

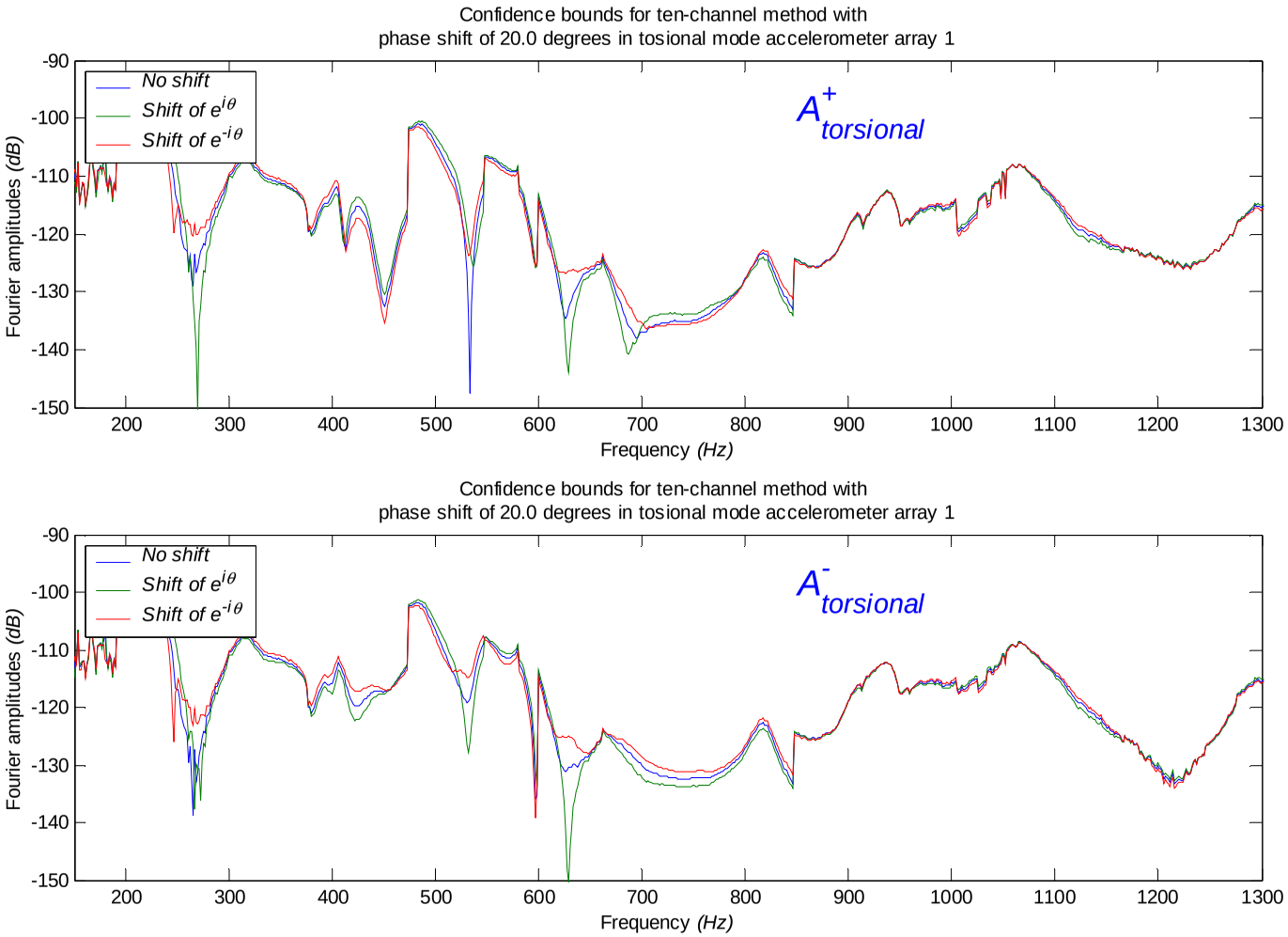

Figure 3.10. Confidence Bounds for n=0 torsional wave with a phase mismatch in torsional accelerometer arrays

3.3. Experimental results

The wavenumber is assumed to be known when applying wave decomposition. An accurate model is therefore required. Dispersion plots for the experimental system and dispersion curves for the theoretical model should be compared. Figures 3.11, 3.12, and 3.13 show dispersion curves for the experimental test rig for *n=1* bending wave, *n=0* longitudinal wave, and *n=0* fluid wave, respectively.

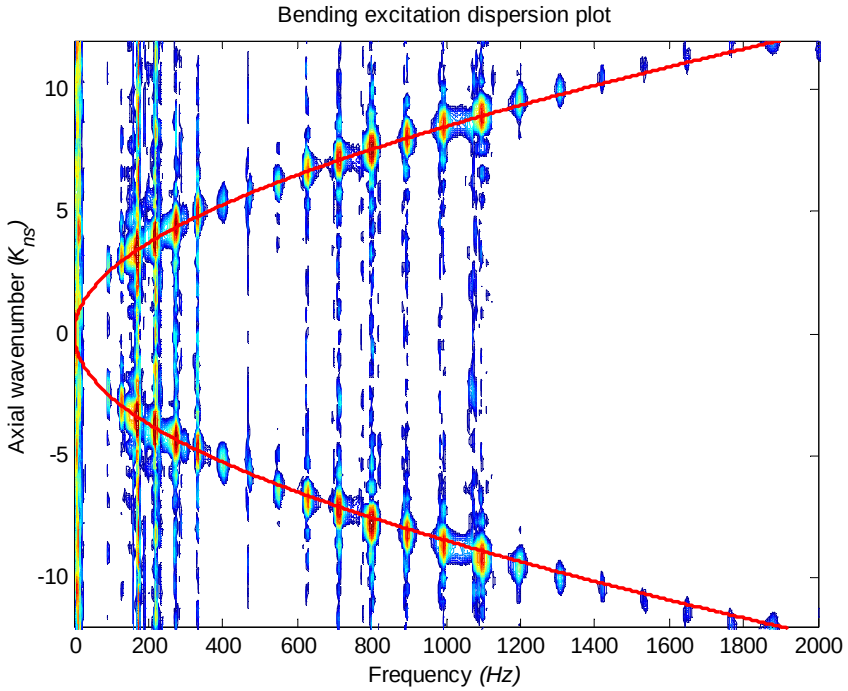

Figure 3.11. Dispersion plot for n=1 bending wave

Bending excitation was applied and accelerometers mounted in the radial direction were used to determine the dispersion plot for bending excitation. The longitudinal and fluid waves are still present, but *n=1* bending wave is dominant. The transfer functions between the input and accelerometer positions in 25 sections were evaluated using a Fourier transform. Figure 3.11 shows a 3D contour plot of these results. The negative traveling wave with negative wavenumbers can be seen below the frequency axis. The

fact that the dispersion line is not straight proves that bending waves are dispersive. This means that wave speeds are different for each frequency.

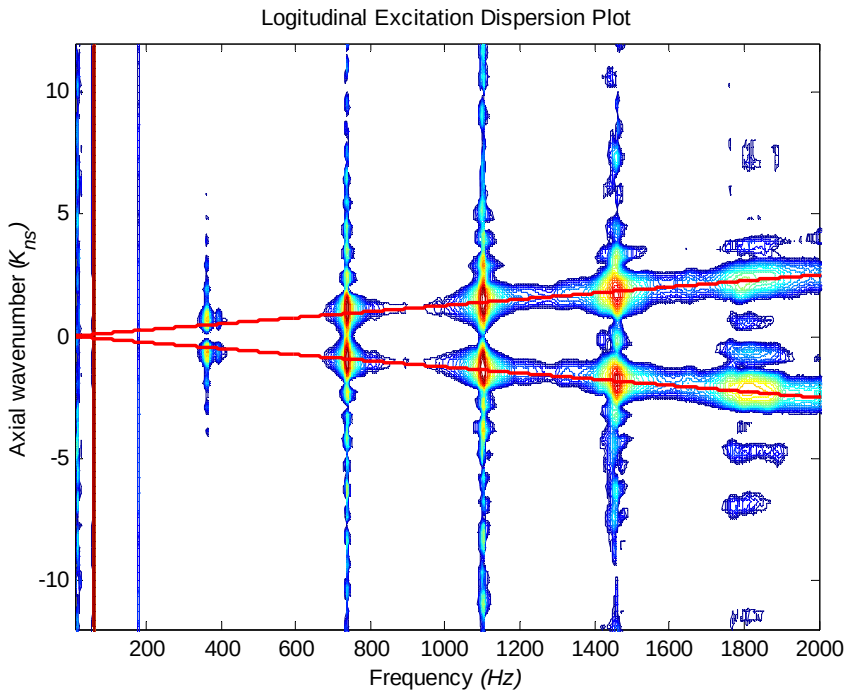

Figure 3.12. Dispersion plot for n=0 longitudinal wave

Longitudinal excitation was applied and accelerometers mounted in the axial direction were used to determine the dispersion plot for *n=0* longitudinal excitation. The transfer functions between the input and accelerometer positions in 25 sections were evaluated using a Fourier transform. The 3D plot in figure 3.12 shows this result with the theoretical line superimposed. The wave number dispersion plot for longitudinal excitation shows that the longitudinal wave has the highest speed (*~5100 m/s*) of all the waves present in the system.

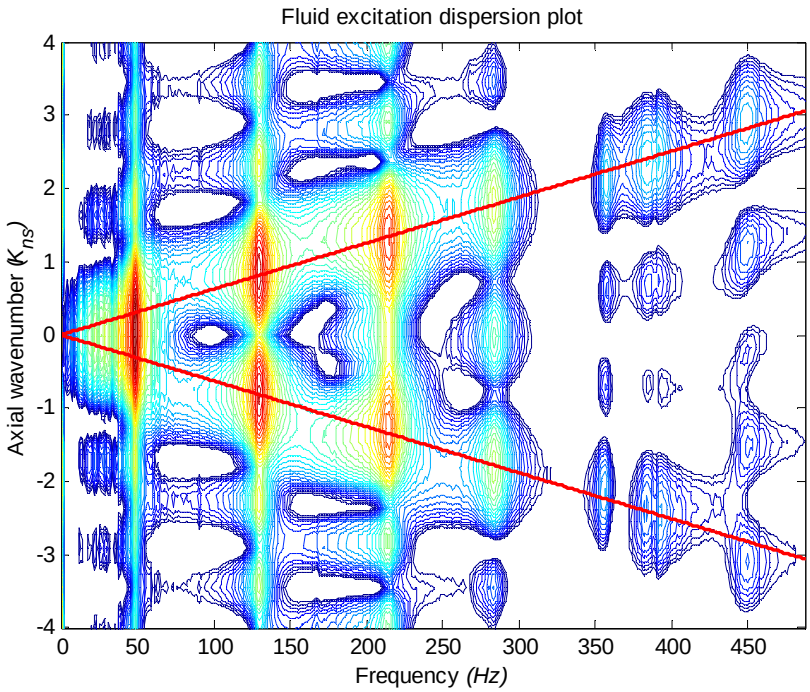

Figure 3.13. Dispersion plot for n=0 fluid wave

Fluid excitation was applied and pressure sensors mounted in the axial direction were used to determine the dispersion plot for bending excitation. The transfer functions between the input and pressure sensor positions in 8 sections were evaluated using a Fourier transform. The 3D plot in figure 3.13 shows this result of *n=0* fluid excitation with the theoretical line superimposed.

The peaks in the dispersion plots correspond to the modes for the specific wave type being studied. In an infinite pipe, the frequency components will show as single lines in a Fourier plot. These lines turn to peaks with minor lobes in a finite pipe. The amplitudes of the minor lobes are determined by amplitude of the major lobe. Hence, the amplitudes of the minor lobes will be larger at frequencies where the modal response is higher. The vertical smearing in the dispersion plots is caused by this phenomenon.

3.4. Limitations of approach

A number of various factors determine the effectiveness of wave decomposition. The accuracy with which the wavenumber is determined, the spacing between transducer arrays, the condition numbers (which tell us whether a matrix is singular or not) of decomposition matrices, and phase matching of transducer arrays all play a major role in wave decomposition.

Of these four parameters, the accuracy of wavenumber approximation has been shown in section 3.3 to be highly accurate. The ideal decomposition would make use of wavenumbers determined experimentally. The variance of experimentally determined wavenumbers and theoretic wavenumbers increases by frequency. We can therefore deduce that the error in determining wave amplitudes with decomposition methods increase with frequency.

The second parameter that has to be analyzed is the spacing between transducer arrays. Wave decomposition uses the phase variance of transducer arrays to approximate wave amplitudes. Therefore, wavelengths of analyzed wave types are equally important. Wave decomposition loses its effectiveness at very low frequencies, where the wavelengths are very large compared to spacing between transducer arrays.

The condition numbers of decomposition matrices describe if those matrices are singular or not. It can be seen that the decomposition matrices have singularities at frequencies that correspond to multiples of one-half wavelengths of fluid wave. Placing transducer arrays closer to each other will increase the interval at which singularities occur due to transducer placement. The condition numbers of decomposition matrices also increase

by decreasing frequency. Hence, Fourier amplitudes determined using these decomposition matrices are not reliable at very low frequencies and at frequencies where singularities occur.

The last parameter that affects the reliability of wave decomposition is matching the phase information of transducer arrays. The changes in Fourier amplitudes have been analyzed and phase mismatch between transducer arrays have been simulated. A phase mismatch between transducer arrays for a specific wave type will show up in the decompositions of the other wave types as well. The only exception is the *n=0* torsional shell wave which is uncoupled from the other wave types present in the system.

Chapter 4

Passive devices

Fluid filled piping installations have many applications. For example, they are an integral part of power transmission in ships and submerged vessels. They also find applications in processing plants, as well as in our daily life with heating systems. Noise caused by piping installations is of interest because of government regulations with regard to environmental noise levels and in military vessels where low noise levels are required. A piping installation will transmit unwanted energy in the form of acoustical and structural vibrations, due to the heavy coupling between the fluid, enclosing volume (pipe wall), and the supporting structure. Thus it is important to reduce the unwanted noise and vibration component in these systems, while maintaining their functionality.

While there are many different approaches to controlling unwanted vibrations and noise, in general passive devices are easier to apply and maintain, making them an integral part of any noise control solution. There are various devices and techniques used in vibration isolation and reduction. This chapter will describe various methods employed in controlling unwanted energy transmission in fluid filled piping installations.

The chapter will begin by explaining the experimental setup used for testing various control approaches. A sample simulation scenario of the effects of bubbles, which are a major problem during experiments, and some sample results for the 6m long test pipe will be presented. Commonly used passive devices such as quarter-wavelength tubes,

rigid stands, isolation stands, and Helmholtz resonators will be considered. These subsections will be followed by the presentation of passive control devices developed during the course of this study. A new and improved Helmholtz resonator design will be presented, followed by a presentation of a dynamic vibration absorber specifically designed to work with pipes. The presentation of a hybrid control device, which employs both the improved Helmholtz resonator and dynamic vibration absorber will be presented last. The performances of each device will be presented followed by a description of their limitations and shortcomings.

4.1. Experimental setup

Multiple passive control devices were studied during the course of this investigation. While these devices use different control mechanisms, their sole function is to control acoustic and shell waves present in a fluid filled piping installation. Therefore, it is necessary to set a reference point from where we can analyze and compare the effectiveness of each control device. This subsection will present the approaches taken to standardize experiments by describing experimental test rigs developed for this study.

4.1.1. Test rig #1

The basis of the analyses presented in this chapter derives from wave decomposition methods developed in the previous chapter. Wave decomposition is inherently dependant on the wavenumbers of the wave types being analyzed. It was important to first analyze and determine the wavenumbers of the waves under investigation. Initial tests for various excitation types (fluid, longitudinal, and bending) were carried out in an extended pipe system, which from this point on will be called test rig #1. The results of

the tests carried out on test rig #1 (wavenumbers, section 2.2) were used in the wave decomposition techniques applied to the analysis of the performance of the passive devices (see section 3).

Test rig #1 (figures 4.1 & 4.2) was built around a 21 ft. (~6m) long 2" galvanized steel pipe. The limiting factor in choosing the length of the pipe was the wavelength of the longitudinal wave. One wavelength of the fluid wave at *200 Hz* corresponded to the length of the pipe.

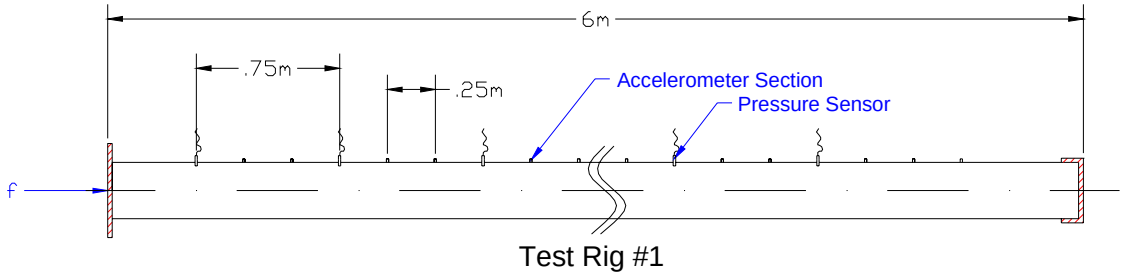

Figure 4.1. Test rig #1

This pipe was drilled and tapped every 25 cm with 1/8" holes. These holes were covered with brass plugs and these plugs served as mounting points for accelerometers and pressure transducers. One end of the pipe was closed with an iron cap and a diaphragm was attached between two flanges on the other end. This setup roughly fit the boundary conditions for the shell waves to free-free and fluid waves to rigid-rigid.

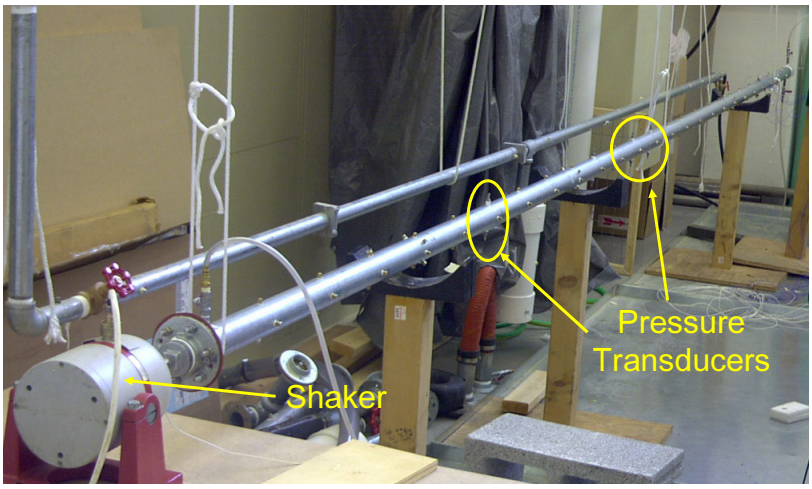

Figure 4.2. Picture of test rig #1

4.1.2. Excitation sources

This section will describe the excitation sources used during the course of this study. A total of three excitation sources were used. These are: “bending”, “longitudinal”, and “fluid” excitations. It should be noted, that due to wave coupling and imperfect force alignment any excitation type will in practice excite all wave types. The objective was to separate the waves being analyzed as much as possible.

Fluid excitation was implemented by attaching a shaker to a diaphragm on one end of the pipe (see figures 4.3 & 4.4). Rubber inserts were used to reduce the transmitted shell vibrations. A PCB force transducer, later replaced by a B&K impedance head, was used to measure the force input to the system.

A 2” cast iron cap with 10/32” holes drilled on the face and one side was used as a base for attaching a shaker for shell excitations. The face hole was used for longitudinal excitation and the side hole was used for bending excitation (figures 4.5, 4.6, & 4.7). A force transducer was again used to measure the input force. As with the case of fluid

excitation, an impedance head replaced the force transducer in the latter stages of this study.

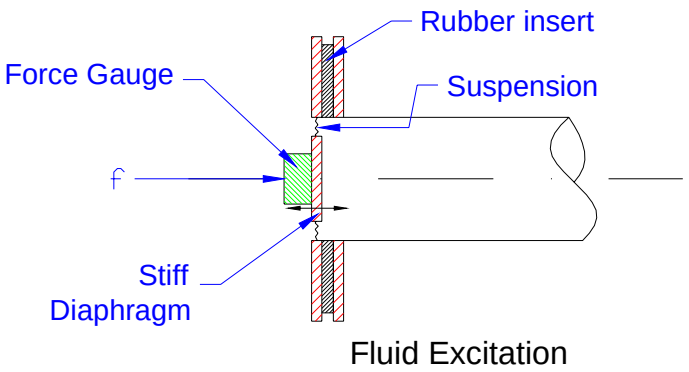

Figure 4.3. Schematic of fluid excitation

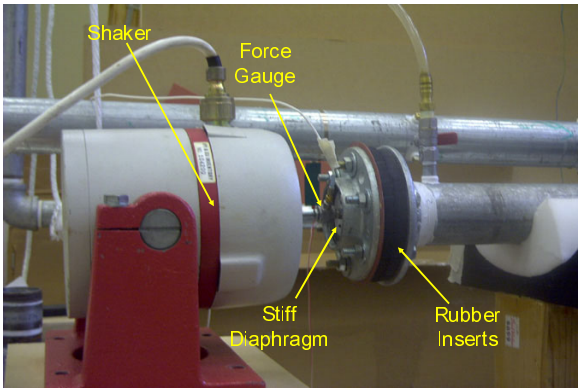

Figure 4.4. Implementation of fluid excitation

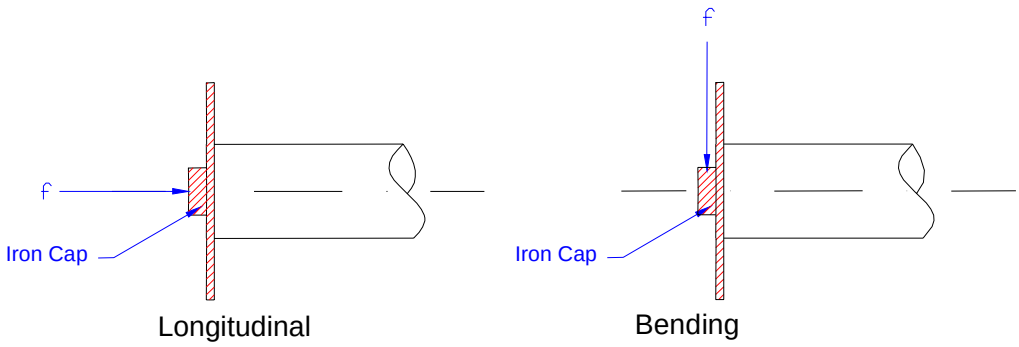

Figure 4.5. Schematic of shell excitations

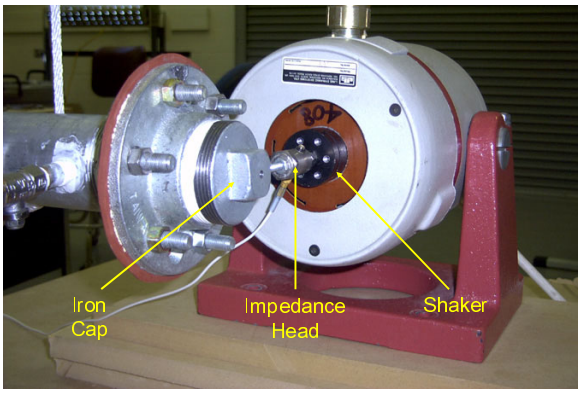

Figure 4.6. Implementation of bending excitation

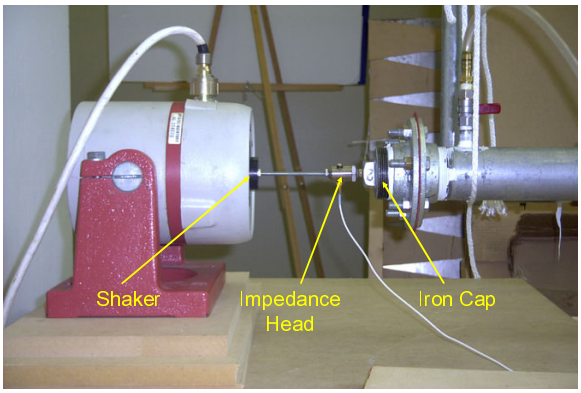

Figure 4.7. Implementation of longitudinal excitation

4.1.3. Test rig #2

Test rig #1 provided the tools (wavenumbers and wave decomposition) necessary to study the control devices. The next step was to develop a standard procedure, by which a comparison could be made between control devices and establish repeatability. Test rig #2 was built around this principle.

Test rig #2 (figures 4.9 & 4.10) was specifically designed to test the effect of devices that acted as discontinuities in the system. This rig had an absorptive termination to prevent

the system from being too resonant. The discontinuities were attached at the middle of the test rig between two flanges.

Four cross-sections, both upstream and downstream, were identified and two of these cross-sections were used for acceleration measurements, while the other two were used for pressure measurements (see figure 4.8). This setup allowed for easy application of decomposition methods. As in the case with test rig #1, an impedance head was used as a reference sensor.

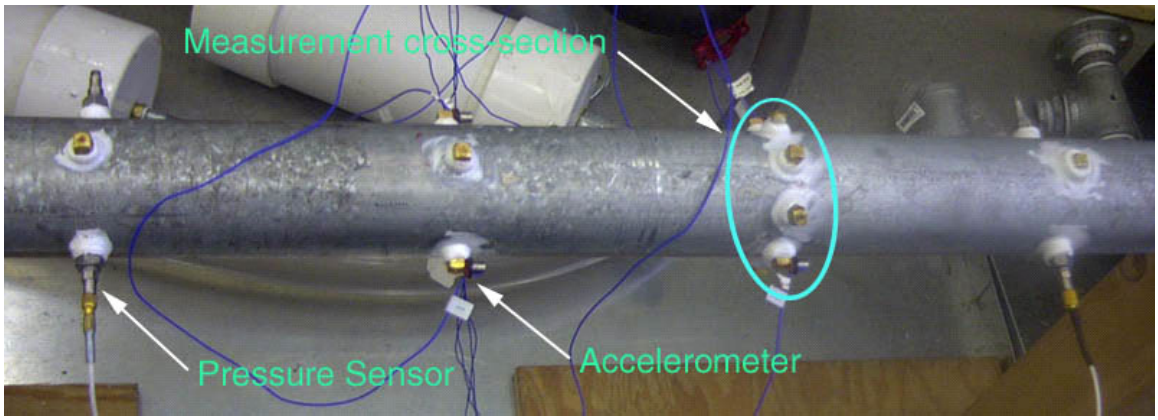

Figure 4.8. Sensor measurements

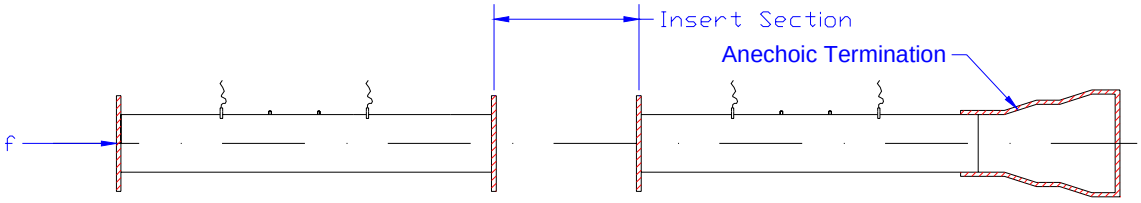

Test Rig #2

Figure 4.9. Schematic of test rig #2

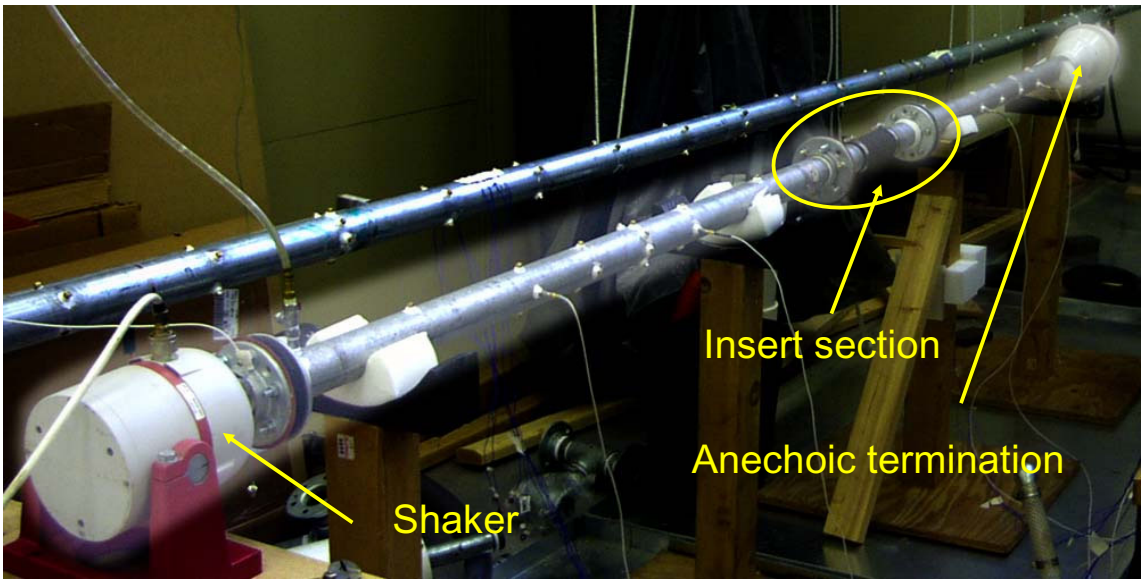

Figure 4.10. Picture of test rig #2

4.2. Simulation scenario – effect of bubbles

The results presented in this chapter show high energy and pressure values at low frequencies. At higher frequencies (from ~250 Hz) the system response exhibits a large drop in pressure and energy values. This section will try to shed some light on this phenomenon. Simulation scenarios where an impedance discontinuity is inserted in between two pipe sections will be presented. The section will start with a description of the simulation setup, followed by simulation scenarios. The section will end with sample results from test rig #1 (~6m long straight pipe) to put the results presented in the rest of this chapter in perspective.

4.2.1. Simulation setup

The simulation setup consisted of pipe sections, labeled upstream and downstream respectively, with a discontinuity inserted in the middle. Figure 4.11 shows a schematic

of this setup. A velocity distribution was applied at one end to create pressure fluctuations in the system. Three pressure values located at locations labeled one through three were calculated using transfer and input impedances for the combined pipe-driver system. The transfer and input impedances to sections one and three were kept the same and four different impedance values were applied at section two. These impedances were (i) a high impedance value to simulate a rigid walled condition, (ii) a low impedance value to simulate a pressure release boundary condition, (iii) exact input impedance for a quarter wavelength application, and (iv) frequency dependant impedance values for a small air bubble with a volume of $1cm^3$. Section 1 is $2m$ long and section 2 is $4m$ long. The reader is encouraged to refer to Appendix C for the formulation of the simulations.

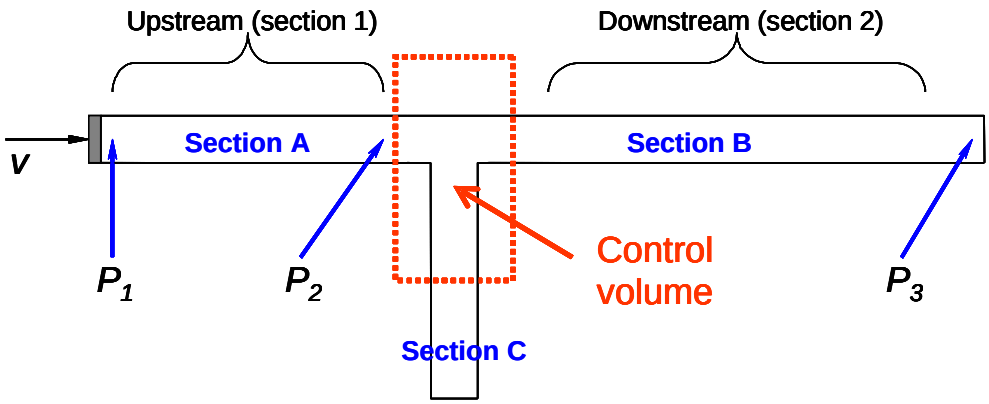

Figure 4.11. Schematic of simulation setup

4.2.2. Changes in pressure along the pipe with a high impedance insertion

The first simulation is carried out with a high impedance value. This is equivalent (or close) to a rigid boundary condition for the pipe wall. This is done to test the validity of

the assumptions. Since the boundary of the pipe is set to a rigid walled condition the plane waves traveling along the pipe should travel without hitting any discontinuities. The real impedance of a rigid wall boundary condition is infinity. This, however, cannot be accomplished with the current software that does finite precision arithmetic. The impedance value was therefore set on the order of 10^{18}. Figure 4.12 shows the input impedances of sections *A* and *B*. The input impedance of section *C* is $1x10^{18}$ *Pa.s/m* and is not plotted. Figure 4.13 shows the resultant pressure values from a constant velocity input through the diaphragm.

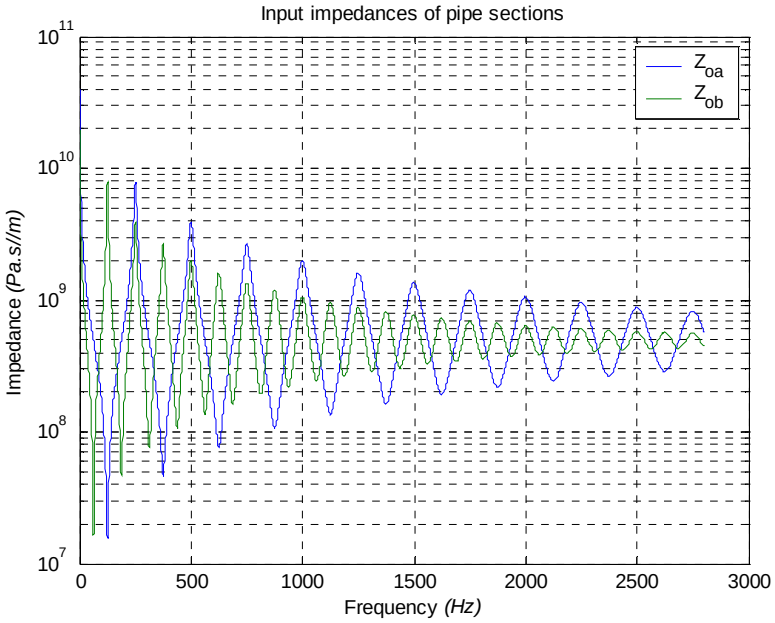

Figure 4.12. Input impedances of pipe sections

The pressure values on both ends of the pipe are of similar magnitude at lower and mid frequencies. The pressure amplitudes decay with frequency due to an introduction of a complex loss factor. This is to be expected since the high impedance boundary condition represents a continuous system.

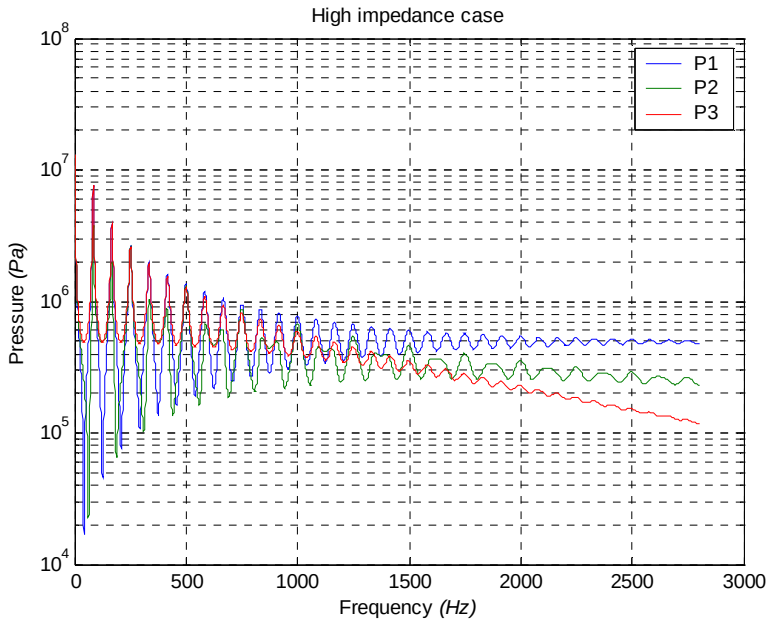

Figure 4.13. Pressure values along the pipe for rigid walled case

4.2.3. Changes in pressure along the pipe with a low impedance insertion

The second simulation is carried out with a low impedance value. This is equivalent (or close) to a pressure release boundary condition. The plane waves traveling in section 1 will be reflected back to the source. Hence, the pressure values downstream will be significantly lower. This simulation scenario is also carried out to test the validity of assumptions. The input impedances of sections A and B are shown in figure 4.12 and the input impedance for section C is taken as *0.1 Pa.s/m* and is not plotted. Figure 4.14 shows the resultant pressure values from a constant velocity input through the diaphragm.

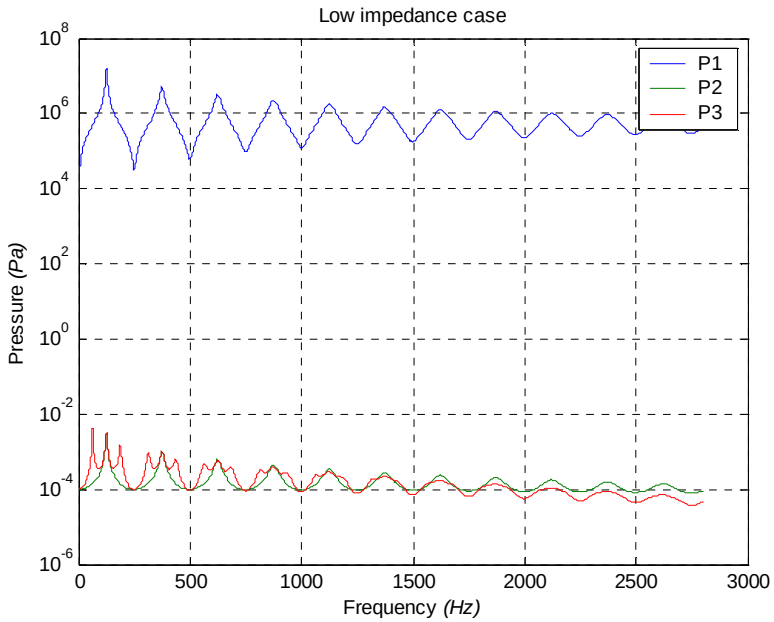

Figure 4.14. Pressure values along the pipe for a pressure release case

The pressure values seen in figure 4.14 closely follow the behavior of an open ended pipe. A significant system response can only be seen in the form of pressure at location 1. The input impedance for the control volume was set to a low value, but not zero due to limitations in software. Hence, there is still some interaction between sections 1 and 2.

4.2.4. Changes in pressure along the pipe with a quarter wavelength tube

A test case of a known passive control device was needed after the validation of assumptions. The quarter wavelength tube was selected because it is a widely used and characterized device. The impedances for sections one and two are kept identical to two previous simulation scenarios. The exact input impedance for a quarter wavelength tube of length *0.615m* is used. Experimental results for this setup will be presented later in this chapter. This tube will have resonances like a normal pipe-driver system. There will be a drop in pressure at this resonant frequency at and after the insertion.

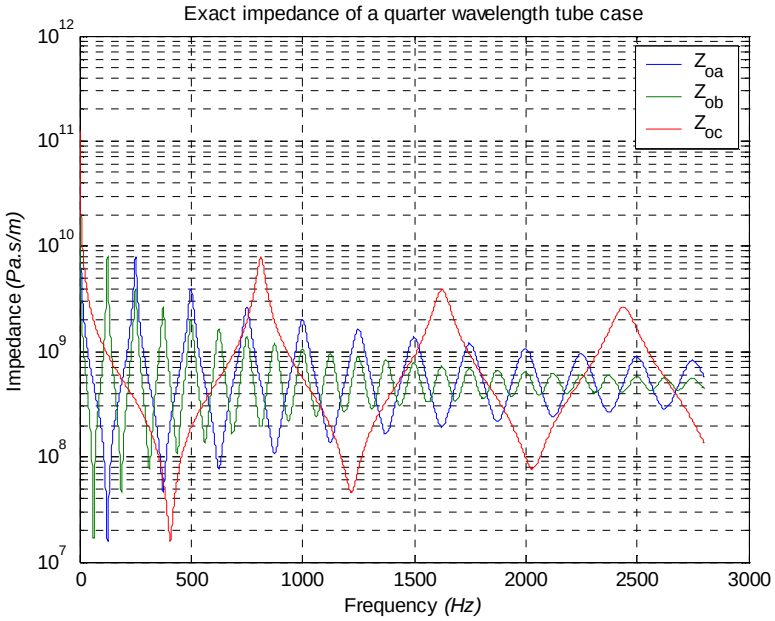

Figure 4.15. Input impedances for pipe sections and the quarter wavelength tube

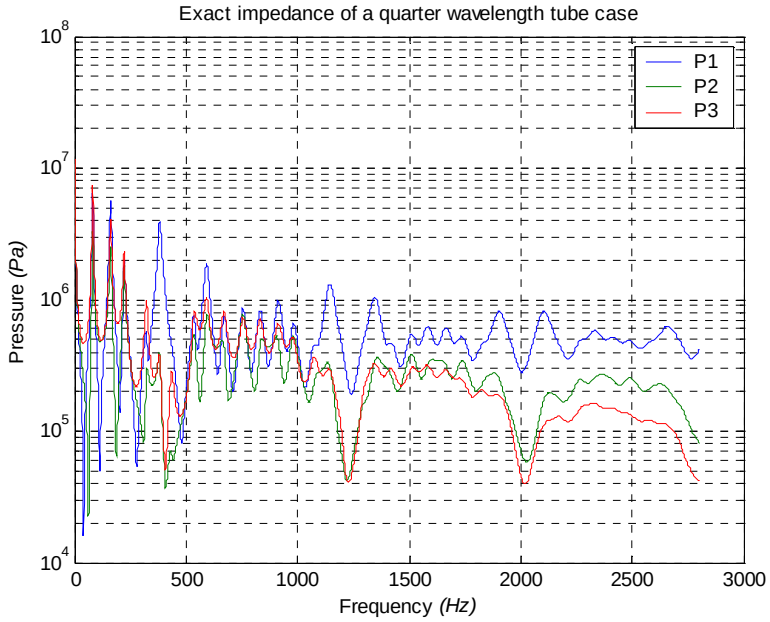

Figure 4.16. Pressure values along the pipe with a quarter wavelength tube.

A drop in pressure at and after the control volume around *430Hz* after the insertion of a quarter wavelength tube is seen. It can, therefore, be claimed that the quarter wavelength tube functions as expected.

4.2.5. Changes in pressure along the pipe with a bubble trapped in the system

The experiments carried out during the course of this study were plagued with problems stemming from the existence of bubbles and the lack of an efficient technique to remove them. It was, therefore, necessary to generate a simulation scenario to test the effect of bubbles on the system. This subsection presents a sample simulation scenario where a bubble is assumed to be trapped right after the upstream section. The lengths of the upstream and downstream sections are kept identical to the previous simulations and the effect of the bubble is investigated. Figure 4.17 shows the impedances for the upstream and downstream sections and the impedance of an air bubble. The impedance of the bubble is calculated from the stiffness of the bubble which is proportional to the change in volume due to a change in pressure.

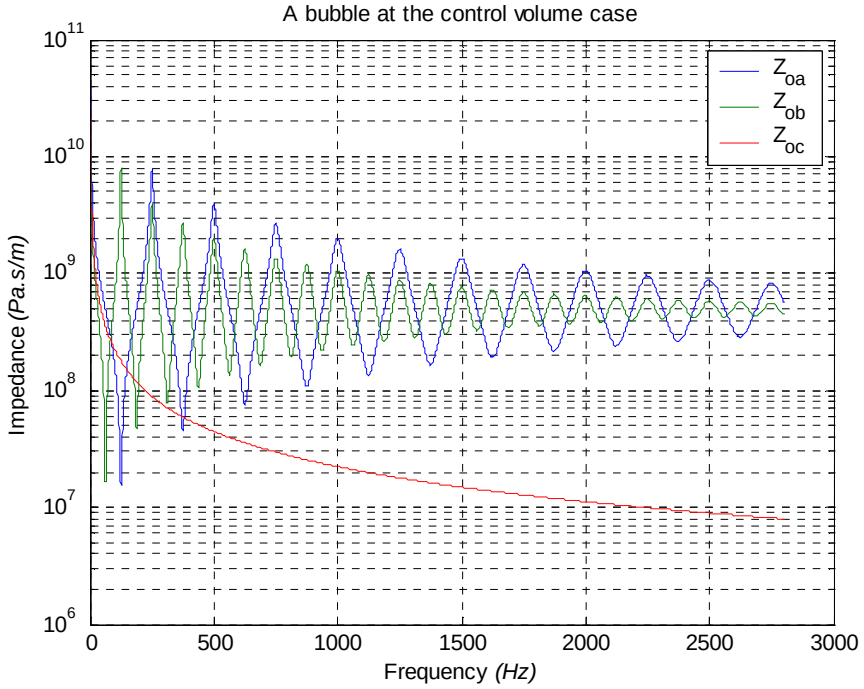

Figure 4.17. Impedances for pipe sections and an air bubble

Figure 4.18 shows the pressure distributions at selected locations along the pipe. An envelope of decay for P_2 and P_3 is superimposed for clarity. The pressure values are of similar order at lower frequencies (below *200Hz*). A sharp decay in pressure values downstream can be seen at higher frequencies. This phenomenon was encountered in all experiments.

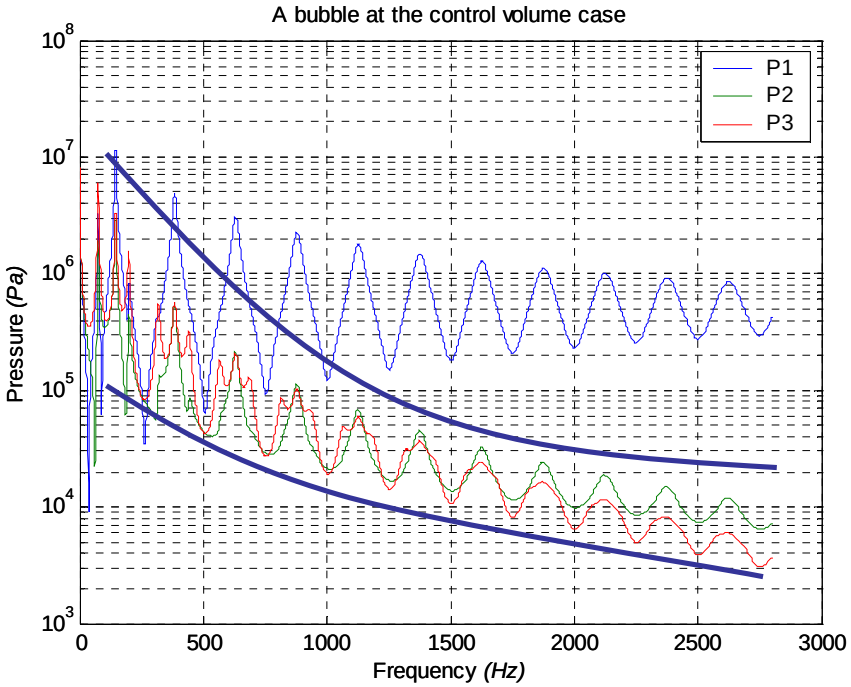

Figure 4.18. Pressure values along the pipe with a bubble trapped in the system

4.2.6. Sample results from test rig #1 to show the effect of bubbles

The initial tests to validate theory and assumptions were carried out in test rig #1 which was a long straight pipe without any discontinuities. Pressure values along the pipe were measured. This continuous (within its bounds) pipe should have, in theory, no decay in pressure amplitudes with increasing frequency. Figure 4.19 shows pressure values along the pipe axis at multiple locations. This case is slightly different from the

simulation presented above as there are probably multiple smaller bubbles at multiple locations, rather than a single big bubble lodged at one location. These bubbles may be located under the brass studs used for measurement mounts or at any location where an imperfection may exist in the pipe wall.

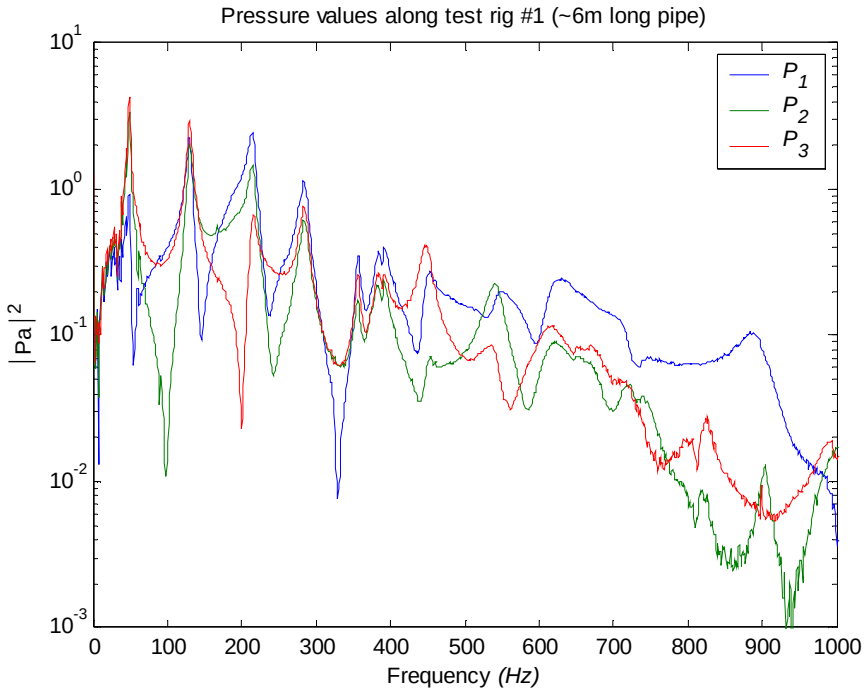

Figure 4.19. Pressure along pipe axis for test rig #1

The amplitude decay trend by increasing frequency seen in the previous section can also be seen in this setup. There is an order of magnitude difference in the response of the system. Net energy is calculated through the squares of the amplitude values. This, coupled with the ill-conditioning present in the decomposition matrix (all wave types are coupled and this results in unreliable overall amplitudes), generates lower than expected energy values at mid to high frequencies and along the axis of the pipe.

Bubbles are responsible for low coherence in transfer functions and lower than expected response for pressure and energy values. However, they can also be used as a passive control method. Bubbles reduce the response of the coupled system at higher frequencies. Passive control devices can therefore be designed to work at lower frequencies and bubbles can be introduced into the system to control pressure fluctuations at higher frequencies.

4.3. Pipe supports

4.3.1. Description

This section will present the behavior of various supporting structures and compare their response. Pipelines provide one of the most efficient transfer paths for vibrational energy from noise sources to the radiators like the structure and sheet metal. A noise source, like a pump, will transmit energy in the fluid it's used to convey and this vibrational energy will transfer into the structure where it's supported.

Pipelines are often supported by rigidly clamping them to the stiff parts of a supporting structure. This practice of rigidly clamping lines to stiff parts is used to keep the pipelines from resonating. However, this causes efficient transfer of energy into the structure. This energy, once in the structure, will excite all the efficient radiators of sound. A constraining support will limit the vibrations at low frequencies and provide for efficient transfer of energy at frequencies corresponding modes of the system. It will be shown that rigid mounts act as efficient conductors of vibrational energy from the pipe into the supporting structure.

Resilient mounts are also commonly applied to pipe lines. They can be found in forms of seismic control hangers or at installations where control of the transmission of vibration and sound to the frame of the structure is critical. A resiliently mounted line, in theory, will prevent energy transmission from the pipe into the structure. A resiliently mounted line not only will be isolated from the supporting structure, but flexing of the resilient material will also act as damping, limiting resonant vibration of the pipe.

There are a variety of resilient mounts available commercially. Their stiffness and isolation properties depend on the type and dimensions of the resilient mount used. For our experiments, B-Line HSL/HS type (HSL-1-105) vibration isolator systems (figure 4.22 & 4.23) were used to attach the pipe to the stands. These hangers function up to 1200 RPM, can support 250 – 350 lbs. (1.55 – 2.00 kN), have a maximum deflection of 1.1", and are generally utilized to minimize the vibrations from suspended low frequency equipment. They allow for a static deflection of 2" and thus can also be used for shock absorption.

4.3.2. Results / implementation

The supporting structures tests were conducted on the six-meter long pipe. The supports were placed at 1.5 meters from both ends, thus giving a simply supported region of 3 meters with two cantilever ends.

Rigid supports were designed from 3"x2" I-beams. They had a width of 26" and a height of 30" (see figure 4.20). I-beams were used to provide strength and decrease the deflections in the stand. The purpose of these stands was to simulate a ship's hull and thereby measure the transmission properties into supporting structures.

A ½" inch threaded stud bolt was used to attach the pipe holders to the stands. The pipe holders were for a nominal pipe size of 2 ½" and were lined with ¼" rubber to act as a low-pass filter (see figure 4.21).

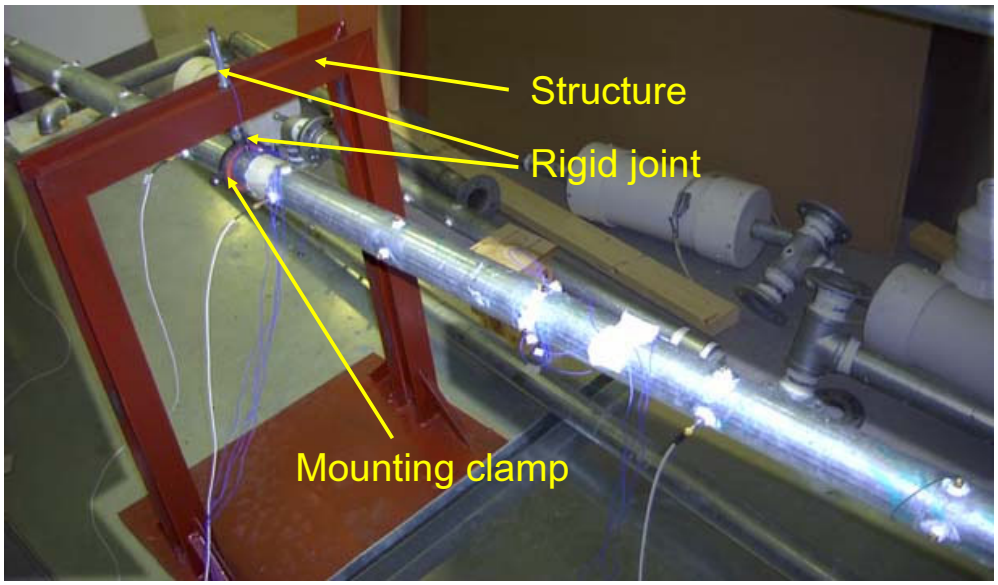

Figure 4.20. Rigidly supported pipe

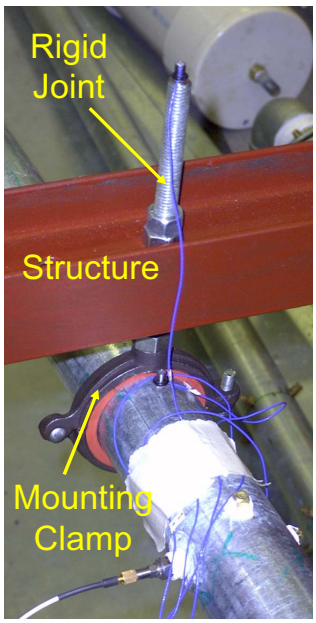

Figure 4.21. Rigid support

The setup to test the isolation hangers was the same as the setup used to test the rigid stand. The supports were placed at 1.5m from the ends and the rigid mounts were replaced with isolation hangers. Vibration levels on both the pipe and the stand were measured to test the transmission properties of the isolators.

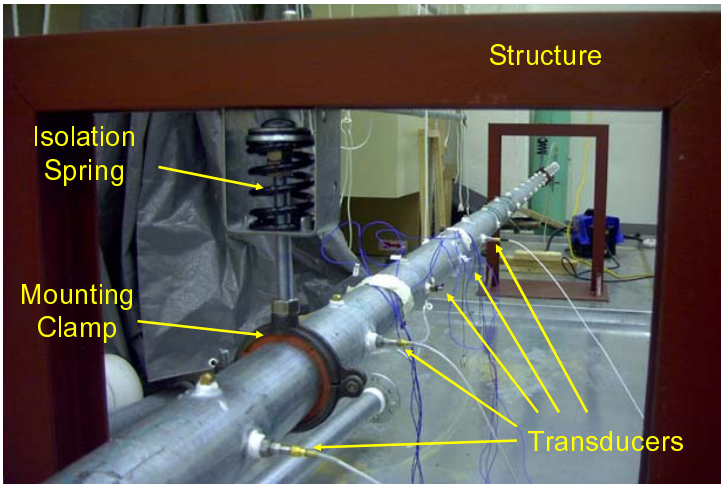

Figure 4.22. Pipe supported with isolation hangers

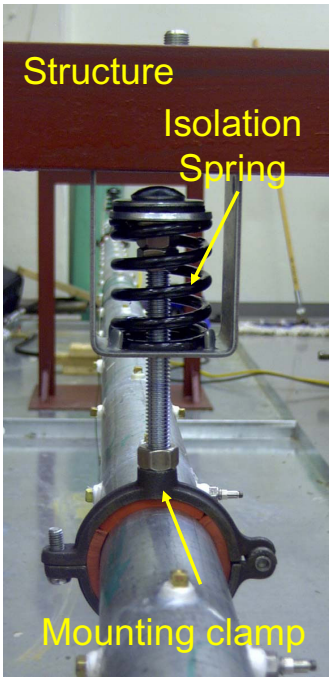

Figure 4.23. Resilient support

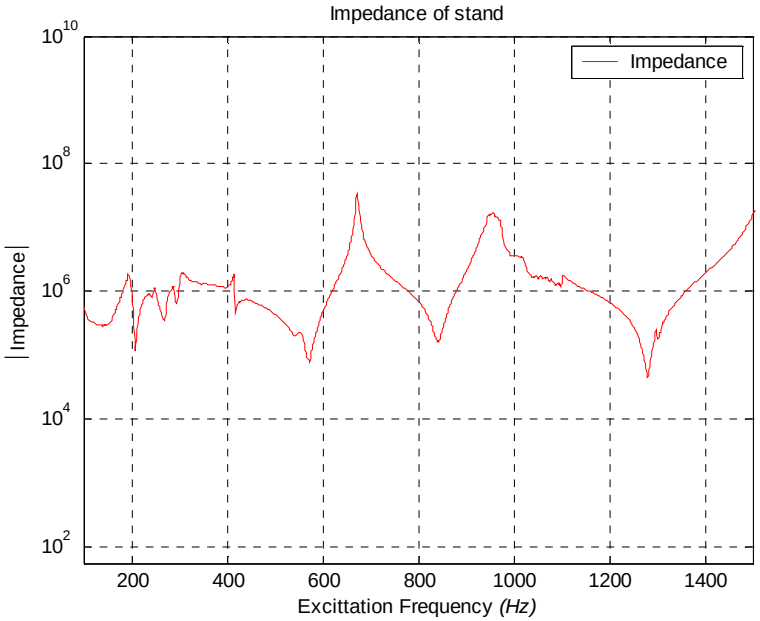

Figure 4.24. Mechanical impedance of rigid stand

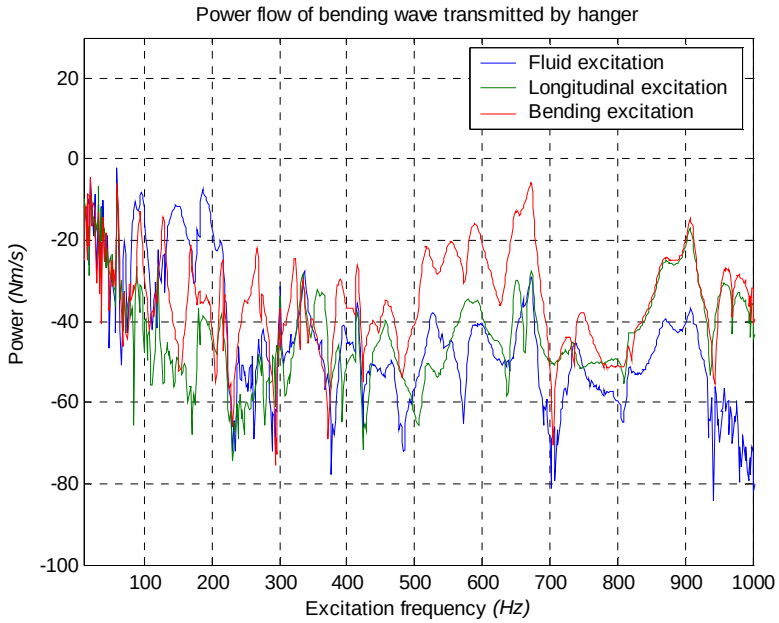

Figure 4.25. Power transmitted into the stand in the form of bending wave

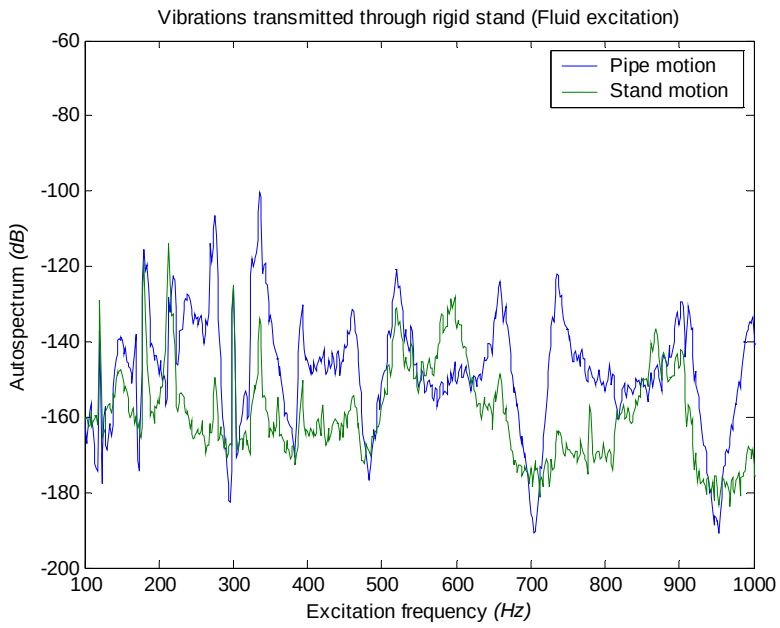

Figure 4.26. Vibrations transmitted into rigid stand

Figure 4.24 shows the mechanical impedance of the stand as seen by the pipe. Energy transmission will be higher at frequencies where the mechanical impedance of the pipe-fluid system matches the input impedance of the pipe stand. This correlation can be seen when figures 4.25 (energy of bending wave transmitted into stand) & 4.26 (vibrations of the stand and pipe) and figure 4.27 (mechanical impedance of the stand) are compared.

The rigid stand also works to couple wave types together. Figure 4.25 shows transmission of energy for the bending wave into the stand regardless of excitation type. The examination of figures 4.25 and 4.26 show the dominance of the bending modes. The clamping can be done in such a way that the modes of the pipe correspond with the frequencies where the impedance is low, in which case the energy transmission into the structure will be limited. As seen in figure 4.26 the pipe vertical motion is transmitted to the structure very well.

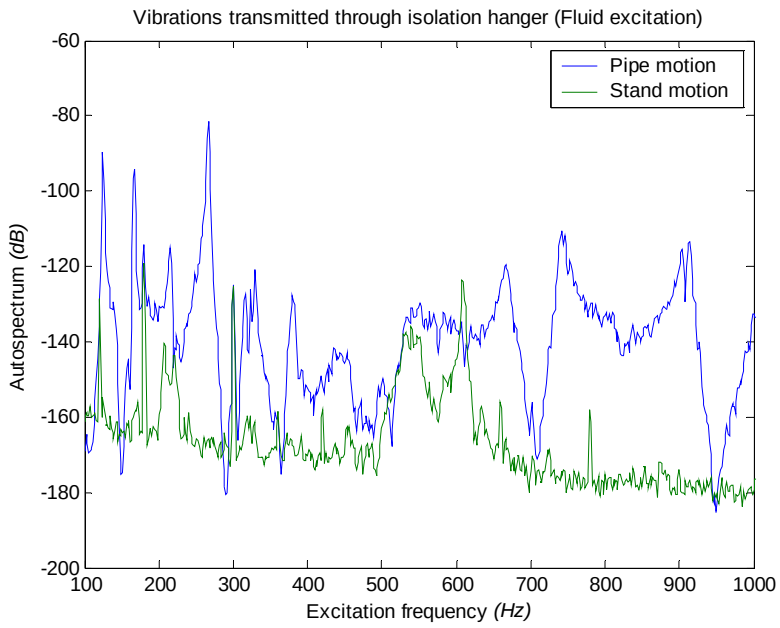

Figure 4.27. Vibrations transmitted through isolation hanger for fluid excitation

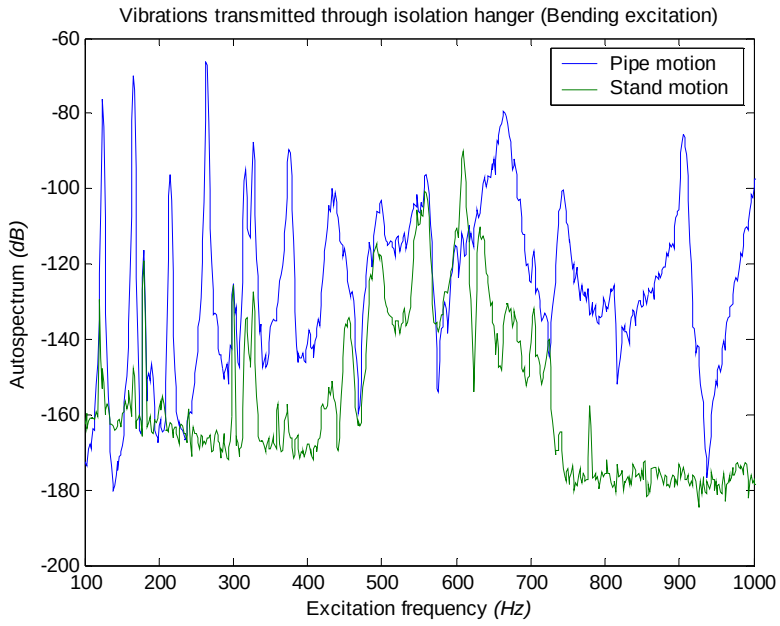

Figure 4.28. Vibrations transmitted through isolation hanger for bending excitation

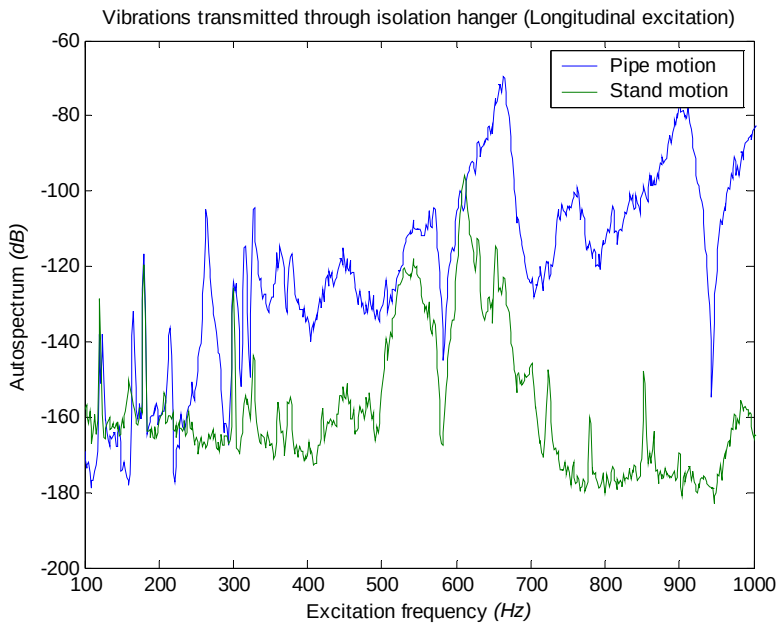

Figure 4.29. Vibrations transmitted through isolation hanger for longitudinal excitation

Isolation stands work on the principle of allowing free movement of pipe with respect to the mounting point. The benefit of using isolations stands is the reduction in the amount of vibrations transmitted into the structure. Figures 4.27, 4.28, and 4.29 show the transmission of vibrations into the structure from fluid excitation, bending excitation, and longitudinal excitation, respectively. The reductions can clearly be seen. Isolation stands can be considered as single degree of freedom systems with the pipe as the mass and structure as the base. As in the case of many single degree of freedom systems, isolation stands have natural frequencies and this corresponds to roughly *600 Hz* (which was calculated by determining the stiffness of the spring from its deflection vs. mass chart and the mass is assumed to be half the mass of the combined pipe-water system) for the system analyzed above. Around this frequency the vibrations of the pipe will be transmitted into the structure. The amount of vibration transmitted would be expected to be higher than the vibrations in the pipe, but it is limited by the damping in the isolation gear. The transmitted vibration levels are very close to the vibration levels in the pipe nonetheless.

4.4. Quarter wavelength tube

4.4.1. Description

The concept of quarter-wavelength tubes has been around since mid-nineteenth century. Quincke was the first to propose the use of unequal acoustic path lengths in a branched duct to cause the acoustic waves to destructively interfere with each other thus canceling propagating waves.

A quarter-wavelength tube makes use of this technique and works on the principle of superposition. When a traveling wave enters the control volume of a quarter wavelength tube (t-junction), waves travel both in the quarter wavelength tube and the control volume. A traveling wave along the quarter wavelength tube will hit the bottom of the tube, which acts like a rigid boundary, and reflect back to the control volume. When this wave reaches the control volume, it will be out of phase and superposition will cancel the traveling wave with a wavelength of quadruple the length L of the quarter wavelength tube. The quarter wavelength tube will cancel pulsations in the fluid at this resonant frequency. The zero impedance at the junction will cause total reflection in the incident wave P_i. Hence there will be no power transmitted at the resonant frequency of the quarter wavelength tube. This means that a quarter-wavelength tube will work well at a multiple harmonic tones, thus application of a quarter-wavelength tube in installations where the disturbance is mainly tonal will be very effective.

A shortcoming in the application of quarter-wavelength tubes is the limit of their operating bandwidth. The device loses its effectiveness if the disturbance signal moves out of this operating range. Another shortcoming of quarter-wavelength tubes is their

sizes for low frequencies. At low frequencies where the wavelengths are significantly larger, the quarter wavelength tube has to increase in length as well. Hence application of quarter-wavelength tubes will be limited by the design parameters, but probably the most important problem with the implementation of a quarter-wavelength tube is the lack of its symmetry, thus providing a secondary pathway for energy to travel via the structure. The incident *n=0* fluid wave on the cap of the quarter-wavelength tube will excite the structure and create a structural path for energy transmission into the *n=1* shell wave.

4.4.2. Implementation / results

Figure 4.31 shows the schematic of a typical quarter-wavelength tube. A quarter-wavelength tube is a reactive device. A traveling wave P_i will encounter a zero impedance section (t-junction) and the component of this incident wave which corresponds to the resonant frequency f_r (see figures 4.30 & 4.31) of the quarter-wavelength tube will be reflected back to the source and energy will be removed from the outgoing wave P_o at the resonant frequency. A standing wave out of phase with the traveling wave will occur inside the tube when the wavelength of the traveling wave is four times the length of the quarter-wavelength tube. A picture of the quarter wavelength tube used during the experiments can be seen in figure 4.32.

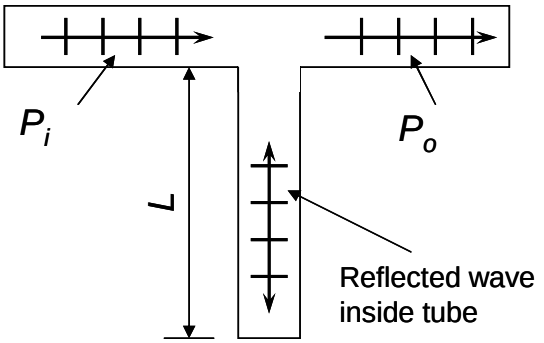

Figure 4.30. Schematic of a quarter-wavelength tube

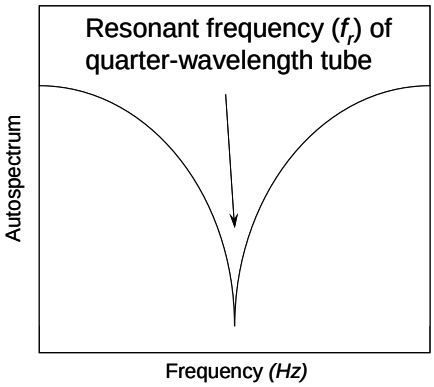

Figure 4.31. Expected behavior of a quarter-wavelength tube


Figure 4.32. Picture of quarter-wavelength tube used during this study

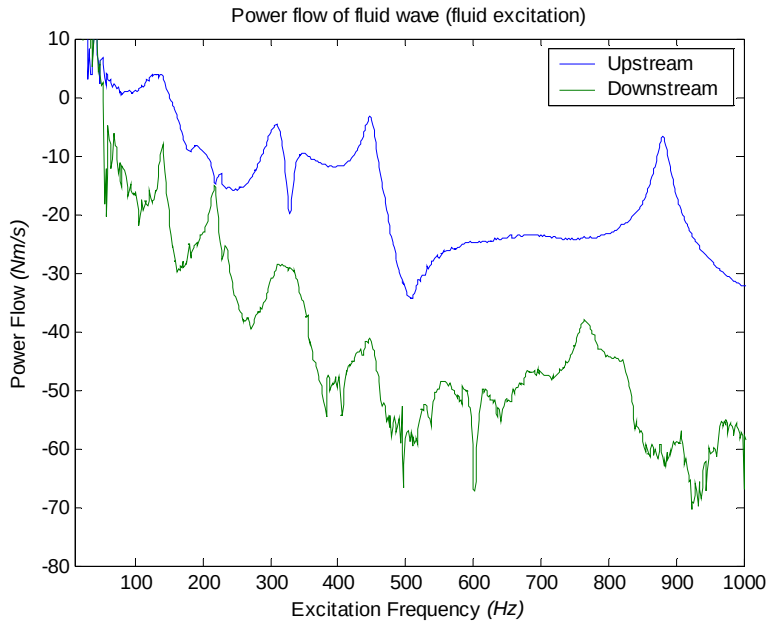

Figure 4.33. Comparison of power flow for fluid wave before and after quarter wavelength tube for fluid excitation

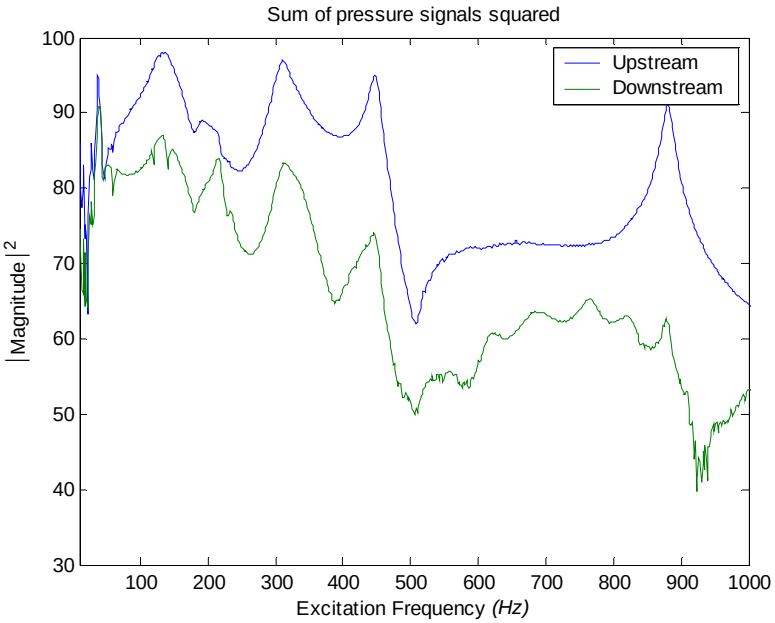

Figure 4.34. Sum of pressure signals before and after quarter wavelength tube for fluid excitation

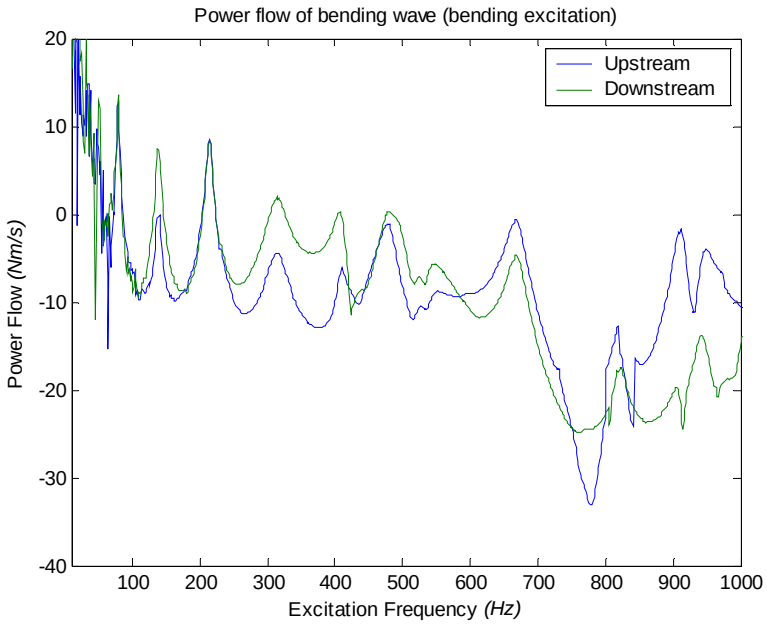

Figure 4.35. Comparison of power flow for bending wave before and after quarter wavelength tube for bending excitation

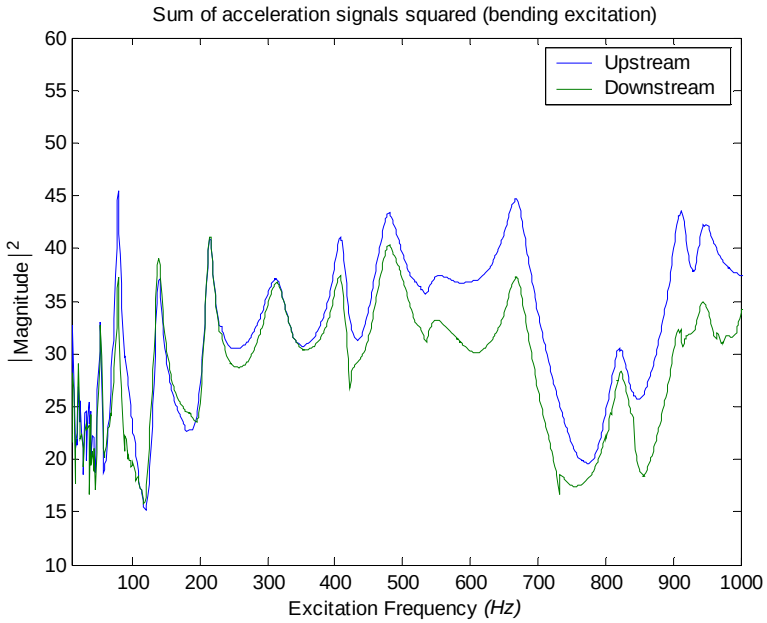

Figure 4.36. Sum of acceleration signals before and after quarter wavelength tube for bending excitation

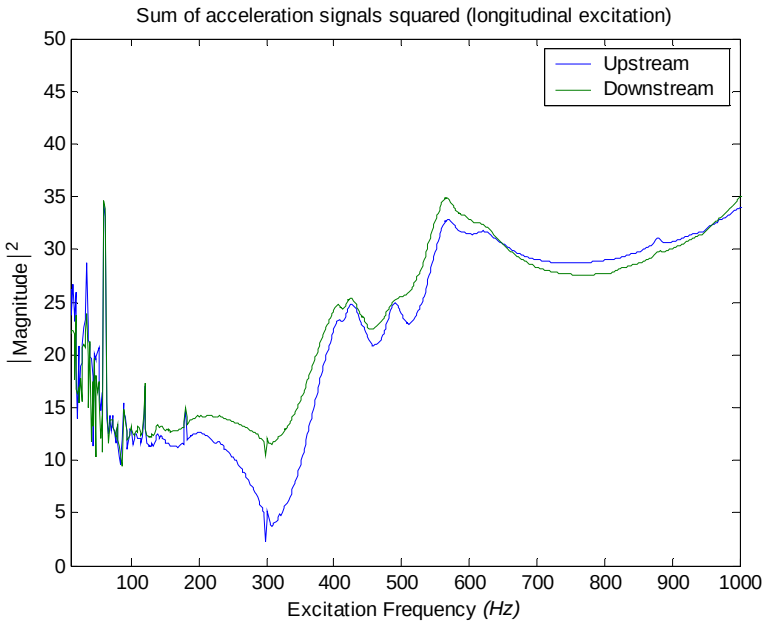

Figure 4.37. Sum of acceleration signals before and after quarter wavelength tube for longitudinal excitation

Figure 4.33 shows power flow in fluid wave before and after the quarter-wavelength tube and figure 4.34 shows the pressure signals upstream and downstream, respectively. The quarter-wavelength tube is designed to work at *400 Hz* and the reduction at this frequency is clearly visible. Reductions are also visible at frequencies higher than *400 Hz*. The broadband reduction may be the result of bubbles (see section 4.2) making the system compliant or the lack of fluid pressure in the system coupled with the imperfect interior surface of the pipe can be interfering with the propagation of the fluid wave. In either case, the fact that quarter-wavelength tubes are effective passive control devices for fluid waves can be concluded.

Figure 4.35 shows the power flow in bending wave before and after the quarter-wavelength tube and figure 4.36 shows the acceleration signals from where the power flow was determined. Although the acceleration signals are smaller after the tube, the

incident power coming out of the tube is higher than of the power coming into the device. Figure 4.37 shows the acceleration signals in those sections.

The quarter-wavelength tube itself works fine for fluid waves. For shell excitations, the tube acts as a cantilever beam and the motion of the fluid inside the tube excites the shell in bending mode, thus providing a flanking energy pathway. The wavelength requirement for fluid waves also limits the uses of quarter-wavelength tubes to higher frequencies where the tube can physically be fitted into the space provided for the piping installation.

4.5. Helmholtz resonator

4.5.1. Description

Helmholtz resonators are commonly found in piping installations. The Helmholtz resonator can be modeled as a lumped acoustic system. It can be represented with a neck area *S*, neck length *L* and rigid walled cavity of volume *V* (see figure 4.38).

The open end of the neck will radiate sound and will provide radiation resistance and a radiation mass. The fluid in the neck, moving as a unit, will provide an additional mass element and the losses at the neck walls will provide additional resistance. The compression of the fluid in the rigid walled cavity will provide stiffness. In this way, the Helmholtz resonator can be modeled as a single degree-of-freedom mass-spring system. The principle of a Helmholtz resonator is to act as an impedance “mismatching” device around its resonant frequency.

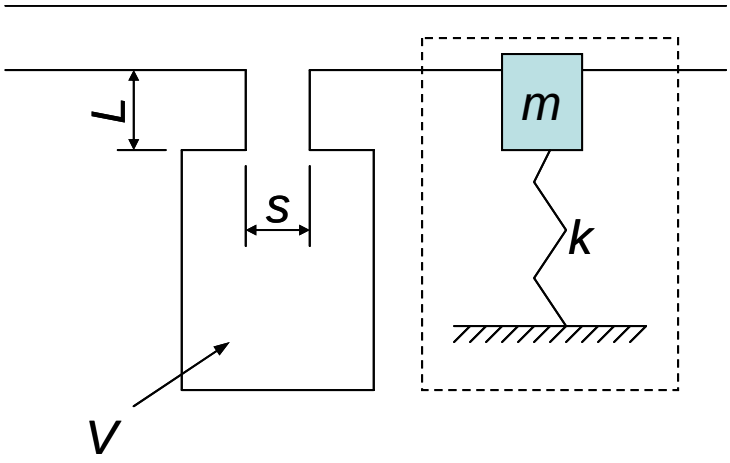

Figure 4.38. Mass-spring analog of Helmholtz resonator

4.5.2. Results / Implementation

The Helmholtz resonator, like the quarter-wavelength tube, is a reactive device and uses the low impedance that occurs at resonance to control sound transmission. Unlike the quarter-wavelength tube, it does not have the reoccurring resonances, but it has a much wider attenuation bandwidth.

The Helmholtz resonators behave like absorptive volumes below their resonant frequency. Above the resonance the mass of the fluid in the neck dominates the impedance. It is to be noted that the attenuations outside the resonance are not very significant; therefore, it can be modeled as a band-stop filter.

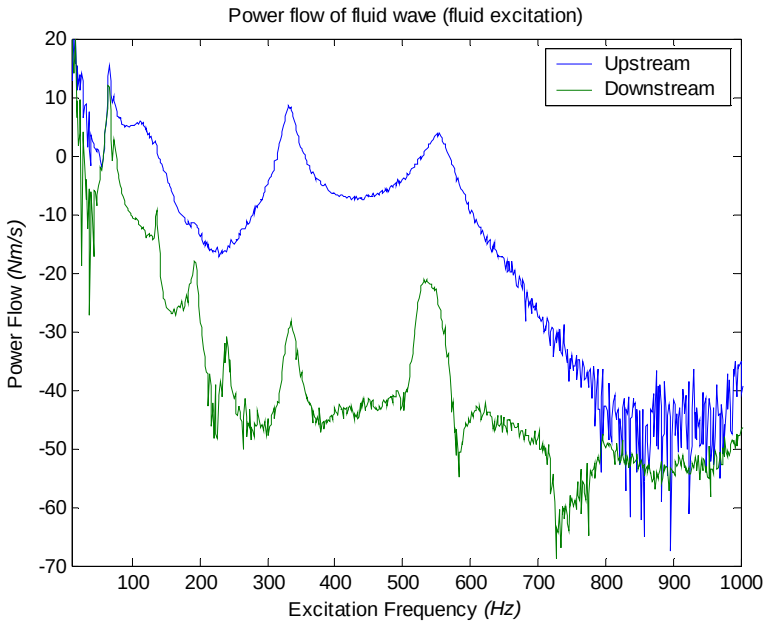

Figure 4.39. Comparison of power flow before and after Helmholtz resonator for fluid excitation

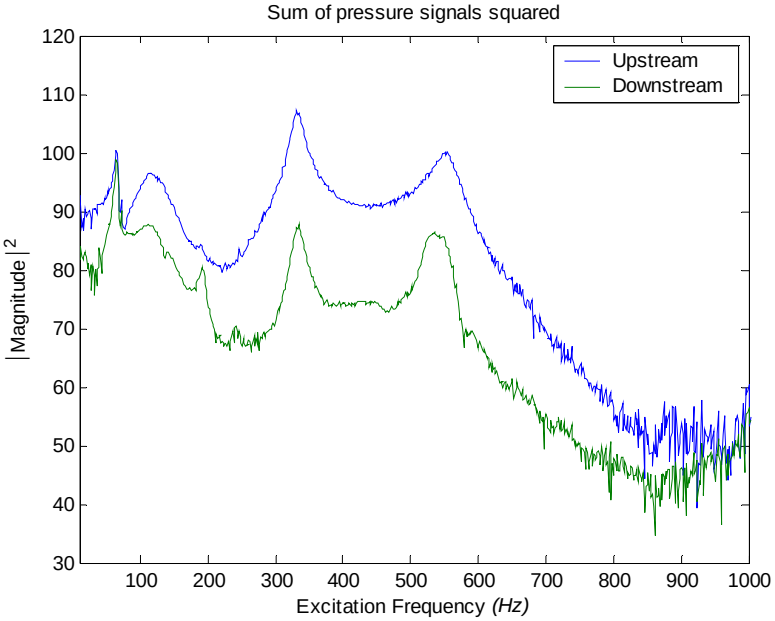

Figure 4.40. Sum of pressure signals before and after Helmholtz resonator for fluid excitation

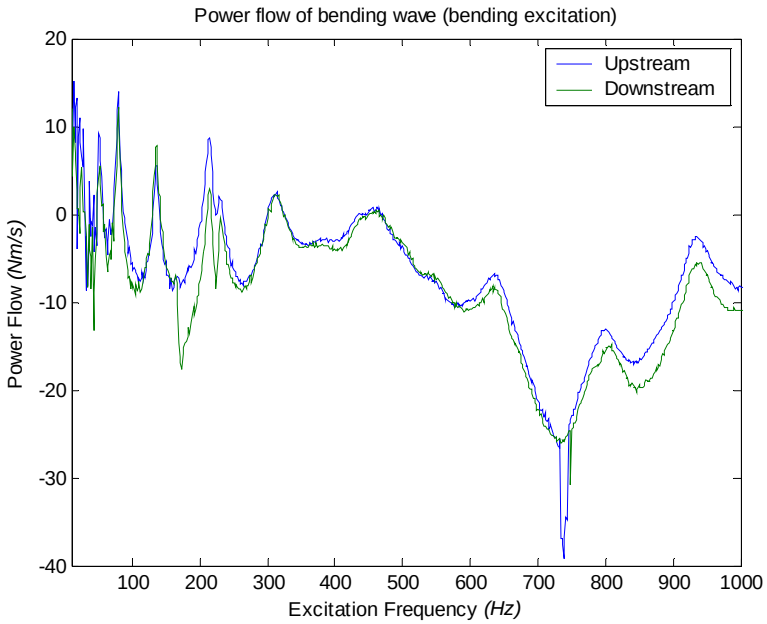

Figure 4.41. Comparison of power flow before and after Helmholtz resonator for bending excitation

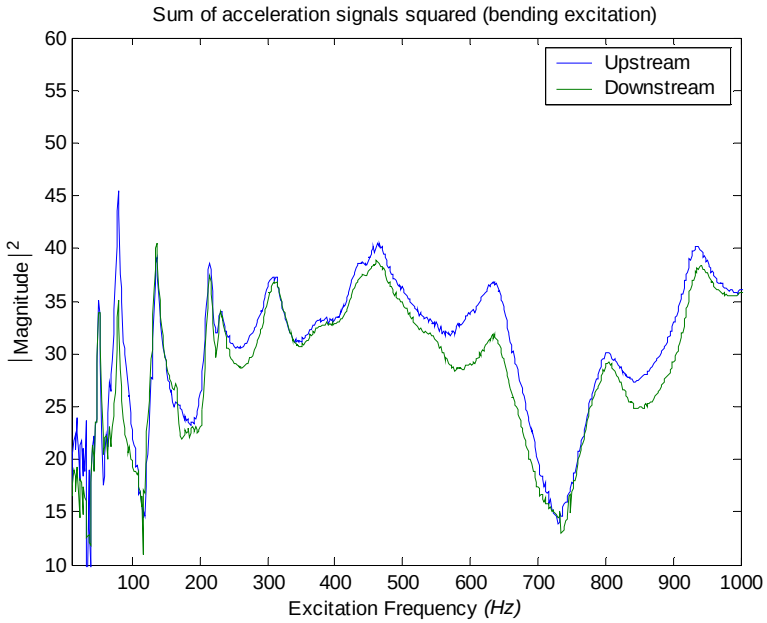

Figure 4.42. Sum of acceleration signals before and after Helmholtz resonator for bending excitation

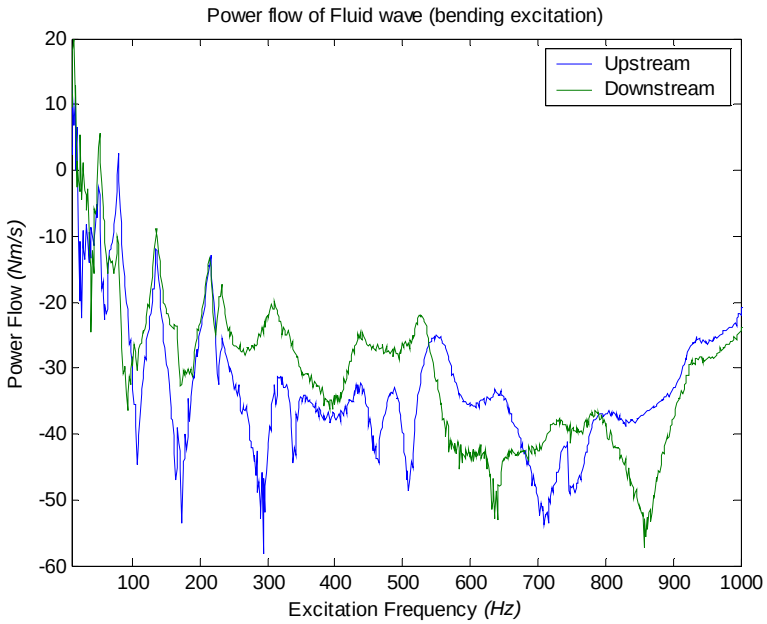

Figure 4.43. Comparison of power flow of fluid wave before and after Helmholtz resonator for bending excitation

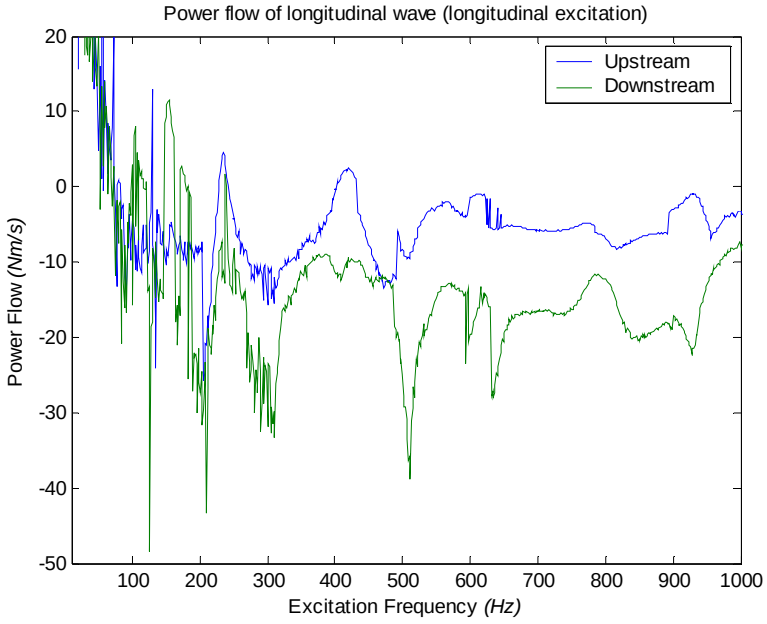

Figure 4.44. Comparison of power flow before and after Helmholtz resonator for longitudinal excitation

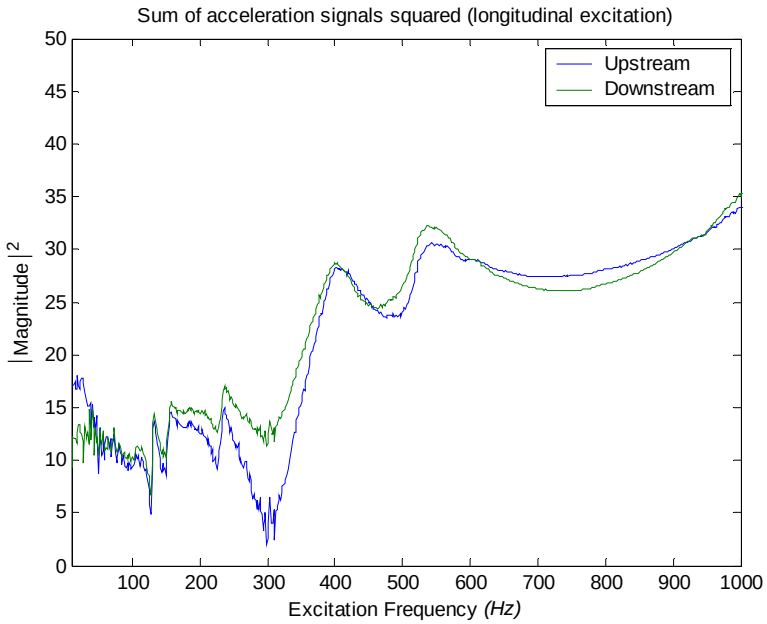

Figure 4.45. Sum of acceleration signals before and after Helmholtz resonator for longitudinal excitation

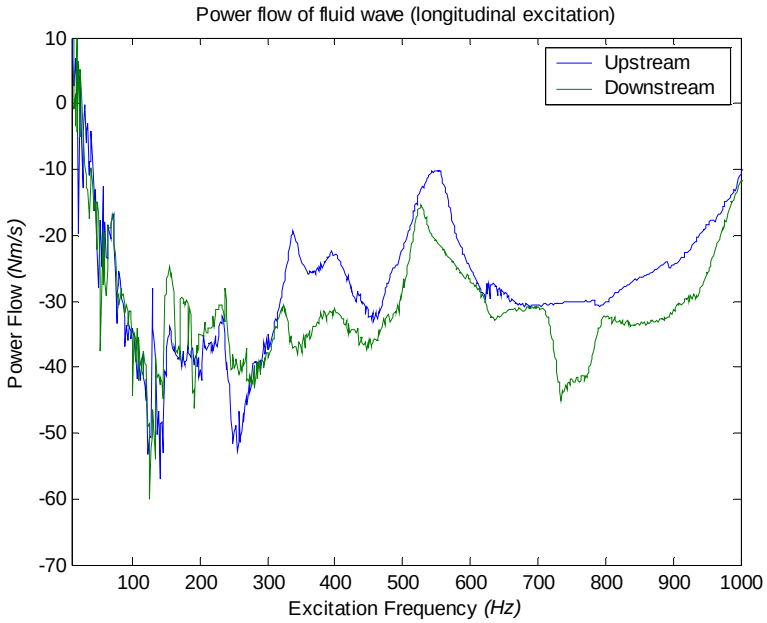

Figure 4.46. Comparison of power flow of fluid wave before and after Helmholtz resonator for longitudinal excitation

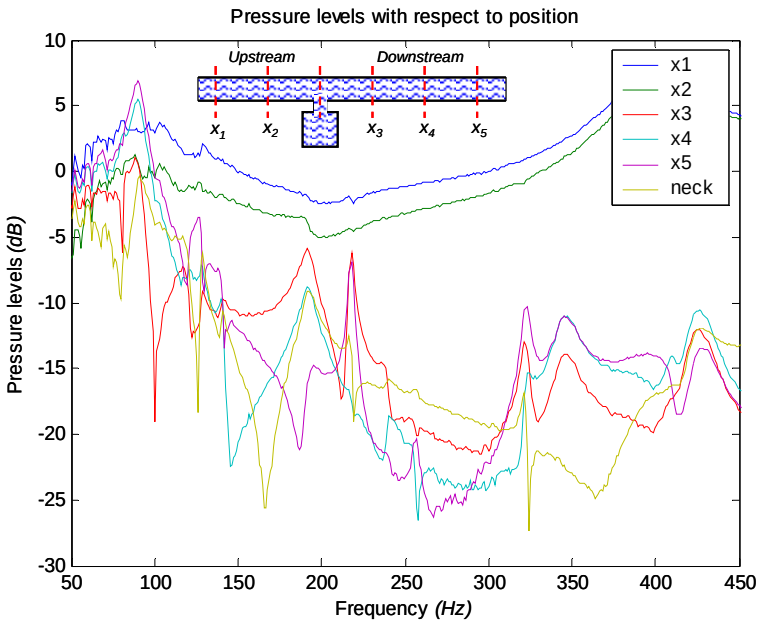

Figure 4.47. Pressure levels at various point along the pipe axis

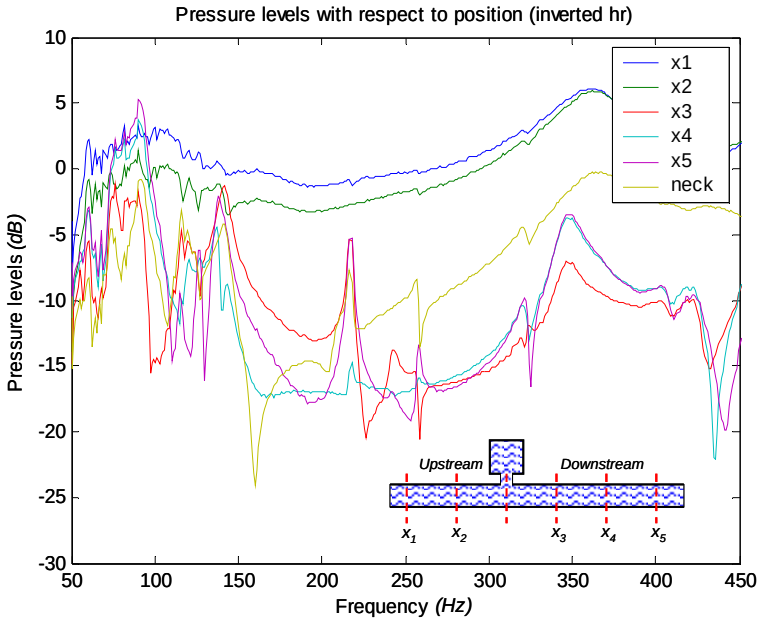

Figure 4.48. Pressure levels at various points along the pipe axis for inverted Helmholtz resonator

The Helmholtz resonator is commonly seen in piping installations. It has a broader bandwidth than the quarter wavelength tube and is effective in reducing pressure levels at t-junction. The resonator in these figures is designed to work around *160 Hz* and the reduction at this frequency can be observed in figures 4.39, 4.40 and 4.47. Figure 4.39 shows the comparison in incident power before and after the Helmholtz resonator and figure 4.40 shows the pressure levels downstream and upstream. The physical make-up of the Helmholtz resonator allows for multiple locations at which bubbles may be stuck. As seen in section 4.2, these bubbles create broadband attenuations at mid to high frequencies.

The mass of the resonator also works as mass impedance for the shell waves and reductions in incident power before and after the resonator can be expected. Under bending excitation the bending waves traveling through the resonator are reduced slightly, but the coupling between the bending wave and the fluid wave prevent reductions in fluid wave as seen in figure 4.43. The increase in levels is primarily due to local excitation of the fluid by the shell.

The same situation is valid for the longitudinal excitation as well. In this case, however, the coupling between the longitudinal wave and fluid wave is less than the case of bending wave and fluid wave and the fluid wave pressure levels are less downstream. Again, this is caused by the resonator acting as mass impedance rather than the principle of stopping transmission in a small frequency band.

The shortcoming of the Helmholtz resonator occurs due to the asymmetry of the design. The mass at the neck and the fluid inside the cavity will excite the bottom of the cavity and this excitation in turn will transmit into the shell, thus providing flanking energy

pathways (see appendix B for a sample graph of vertical motion in shell neck). The result will be good performance (reduction in pressure levels) right at the neck but no performance (reduction) as we get farther away from the resonator which can be seen in figures 4.47 & 4.48.

4.6. Improved Helmholtz resonator

4.6.1. Description

A classical Helmholtz resonator can couple waves because it's asymmetric. The vibrating mass at the neck will excite the rigid shell and thus couple into the structure. This is called a flanking transmission path and will reduce the effectiveness of the Helmholtz resonator in the downstream section of the installation. Section 4.5 demonstrated that the reduction in acoustic pressure right under the neck does not lead to reduction in acoustic pressure downstream.

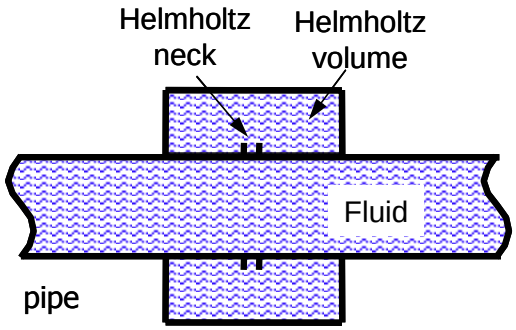

Figure 4.49. Classical Helmholtz resonator compared with symmetric Helmholtz resonator

The proposed solution is the use of a symmetric Helmholtz resonator (shown in figure 4.49). This design ensures that the shell excitation induced by the vibrating body at the

neck will not couple into the flanking transmission pathway and thus reduce the effectiveness of the resonator.

4.6.2. Results / Implementation

The improved Helmholtz resonator consisted of four symmetrically placed necks (see figure 4.50) with the cavity section wrapped around them. The cavity was made from 6" schedule 40 PVC pipe around a 2" internal pipe. An air relief valve was attached at one end to remove air bubbles collecting inside the cavity and pressure transducers were positioned on the cavity shell. The finished design can be seen in figure 4.51.

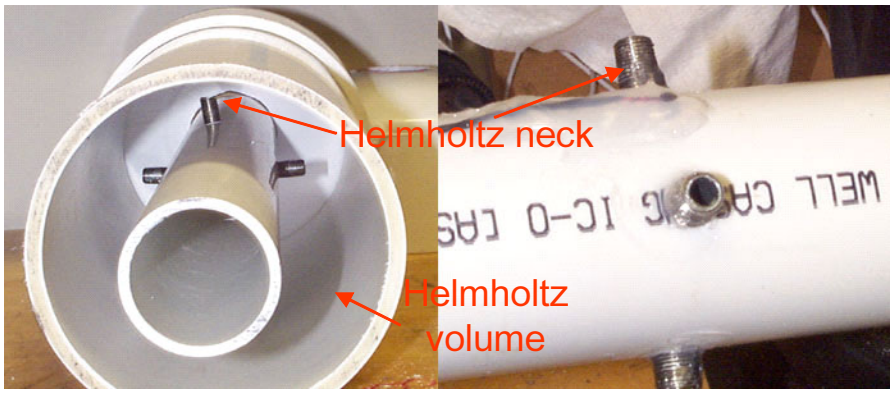

Figure 4.50. Neck section and internal view of Helmholtz resonator

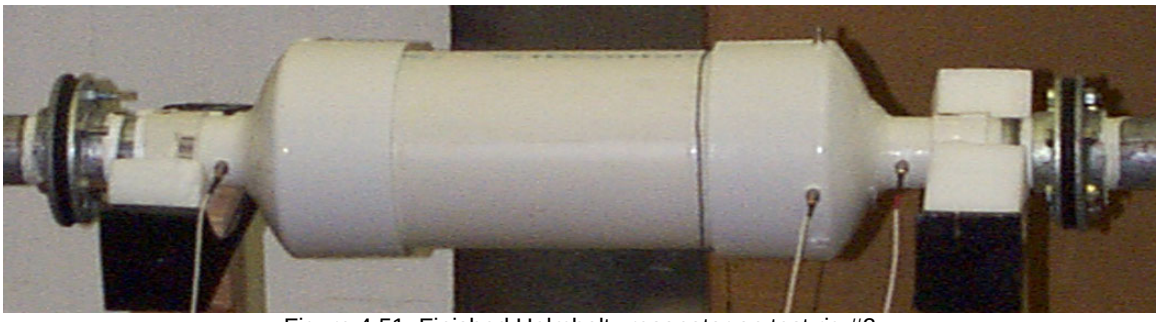
Figure 4.51. Finished Helmholtz resonator on test rig #2

The initial design for the Helmholtz resonators used PVC material for both the inner pipe and outer cavity pipe. This caused impedance mismatch because the traveling shell

waves in the steel upstream section encountered a lighter material resulting in reflected waves which interfered with measurements. The latter Helmholtz resonator designs were directly mounted on steel pipes to make sure traveling waves did not encounter any discontinuities in the axial direction (see figure 4.52).

The final resonator design didn't have the long necks used in the initial design stage and was designed to function at a higher frequency. The concept of tuning the resonator externally was also introduced at this stage. The idea behind this concept is to use external metal clamps to increase the stiffness of the cavity shell, thus shifting the frequency at which the resonator works (see figure 4.54).

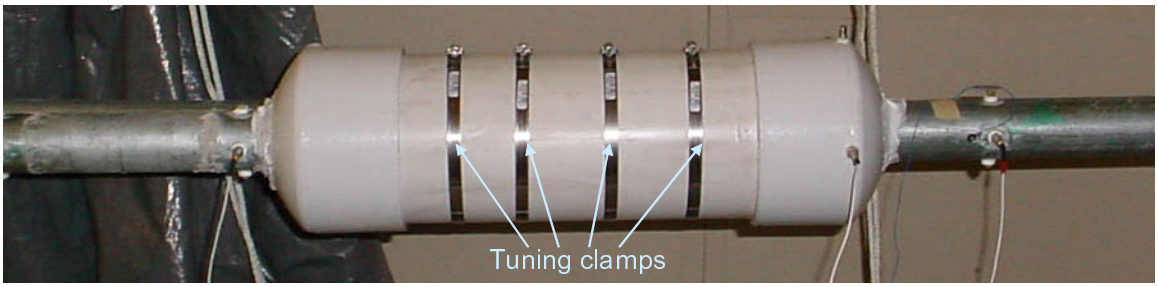

Figure 4.52. Final resonator design with tuning clamps

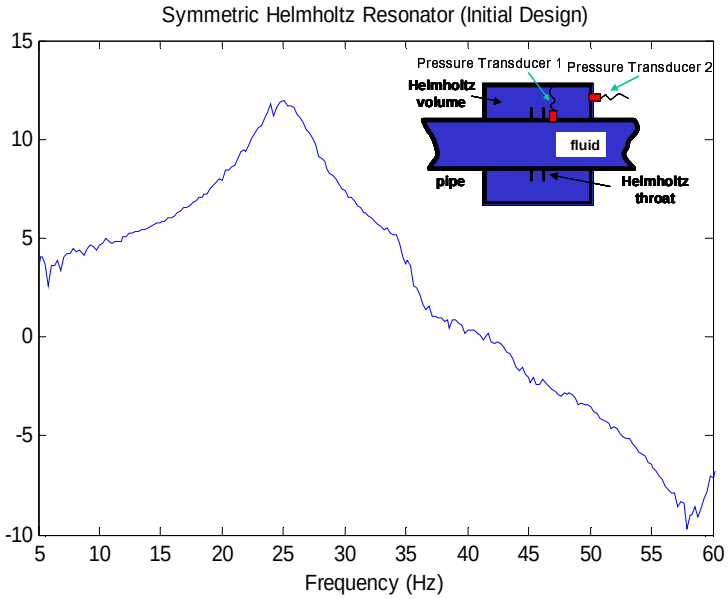

Figure 4.53. Frequency response of Helmholtz resonator

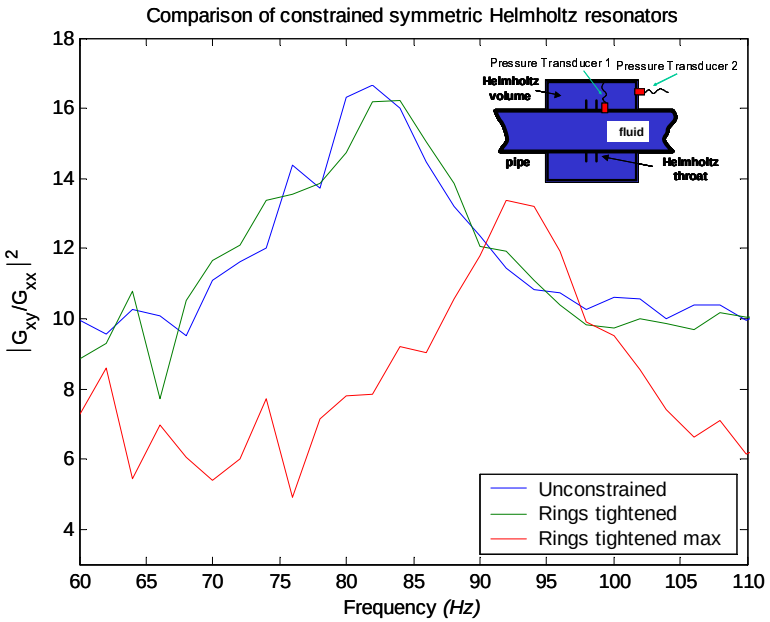

Figure 4.54. Comparison of resonant frequency changes with respect to changes in shell stiffness

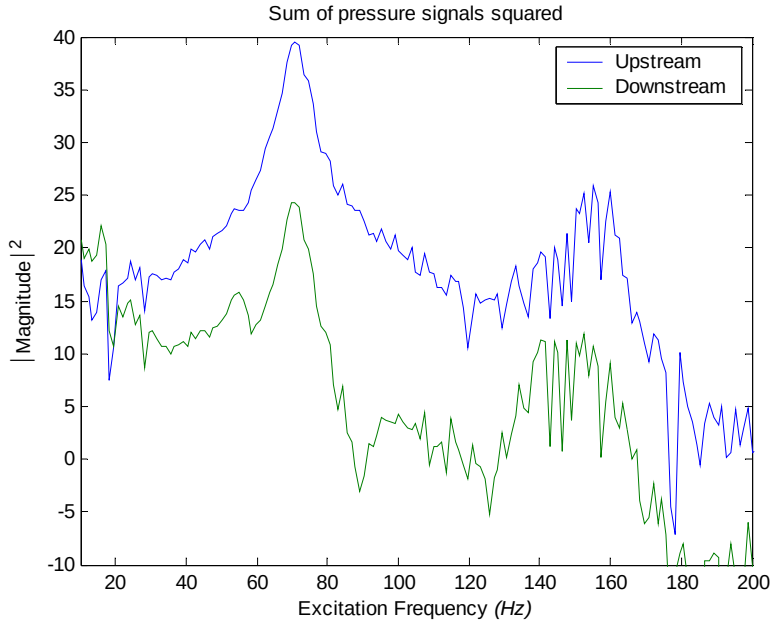

Figure 4.55. Sum of pressure signals squared

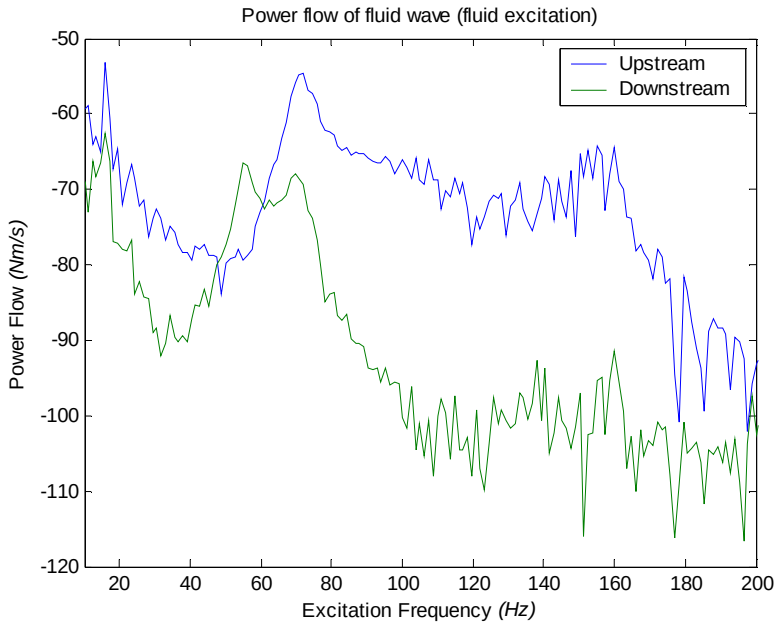

Figure 4.56. Power flow comparison

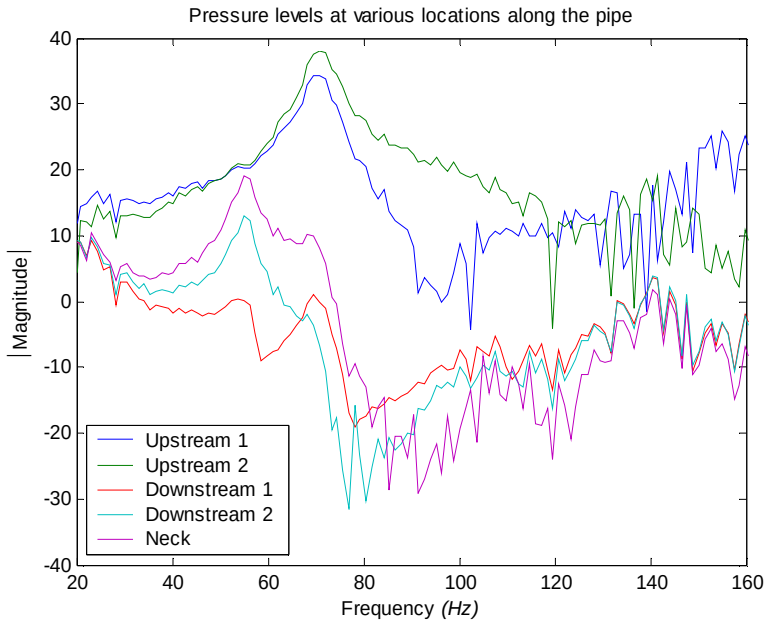

Figure 4.57. Pressure levels at various points along the pipe axis

The symmetric Helmholtz resonator design strives to correct the shortcomings of the classical Helmholtz resonator by removing the asymmetry of classical designs and thus

removing flanking energy pathways from the system. It has been shown in the previous section that the reduction in pressure levels at the neck of the Helmholtz resonator does not necessarily translate to pressure level reductions downstream.

The resonant frequency of the symmetric Helmholtz resonator is measured by taking the transfer function between a pressure sensor located at the neck of the resonator and a pressure sensor attached to the cavity shell. Figure 4.53 shows the transfer function of the first symmetric Helmholtz resonator obtained from this setup. Figure 4.54 shows the change in resonant frequency of the Helmholtz resonator with respect to the changes in the stiffness of the shell material.

Figures 4.55 and 4.56 show comparisons of pressure levels and incident power levels, downstream and upstream, respectively. The resonator was designed to function around *100 Hz* and is functioning as designed. The resonator was built around a PVC pipe capped with PVC caps. The shell is therefore more compliant than a steel shell. The physical make up also allows for bubbles to gather and the air relief valve attached to the resonator to remove bubbles isn't very effective. Hence, although the resonator wasn't designed to achieve broadband reduction, broadband reduction can also be seen. This outcome, seen previously with the other passive devices designed to control fluid waves, is due to compliance caused by bubbles as explained in section 4.2 and the softness of the shell.

The symmetric Helmholtz resonator places the necks opposing each other. This allows the excitation of the Helmholtz resonator cavity wall to cancel each other, hence removing the flanking pathway. This translates to reductions in pressure levels along

the axis of the pipe after the resonator and not just at the resonator junction. This is clearly seen in figure 4.57, which shows pressure levels along the pipe axis.

4.7. Dynamic vibration absorber

4.7.1. Description

Asymmetric passive control devices can lose their effectiveness if they act as asymmetric discontinuities and therefore couple wave types together. Figure 4.58 shows such a device attached to a piping system. This device can be utilized to control bending waves in one plane but will not be as effective in controlling bending waves traveling with different polarization angles. The control authority it will have over traveling fluid waves or compressive waves will also be limited.

A symmetric vibration absorber can be used to overcome this problem. The design utilizes a compliant stiffness layer wrapped with a mass layer. The device is symmetric, this it will not couple wave types together and the motion of the absorber will automatically adjust to control waves traveling with any bending polarization angle. If the stiffness layer is carefully designed (or chosen), then the device will also control axial waves by having a resonant frequency associated with axial motion. Therefore, two wave types can be controlled simultaneously using a single device (see figure 4.59).

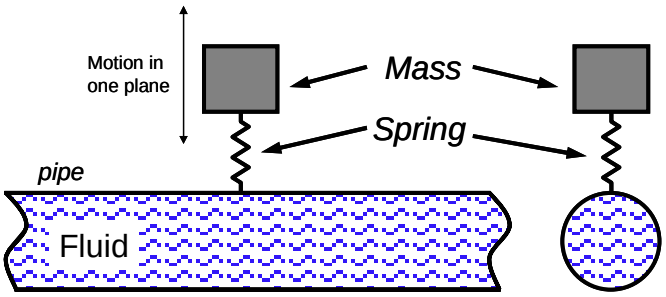

Figure 4.58. Classical vibration absorber attached to a pipe

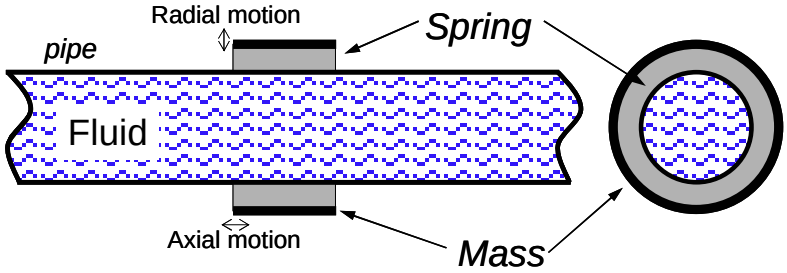

Figure 4.59. Symmetric distributed vibration absorber

4.7.2. Results / Implementation

The symmetric distributed vibration absorbers were tested on rig #1 (see section 4.1.1). An absorptive wedge termination (see figure 4.60) was added to the test rig at one end to dissipate energy thus increasing the ratio of energy flow into the wedge relative to the flow out of the wedge. The incident power before and after the DVA was then measured.

The first DVA was designed to control the bending waves present in the pipe. This DVA had a PVC mass layer and was found to have a natural frequency (out of plane motion) of *184 Hz*. The DVA was then loaded with mass to tune its natural frequency down to *148 Hz* (4th bending mode of the empty pipe) to demonstrate the effectiveness of this DVA in

controlling the bending waves. The initial design and the tuned version can be seen in figure 4.61.

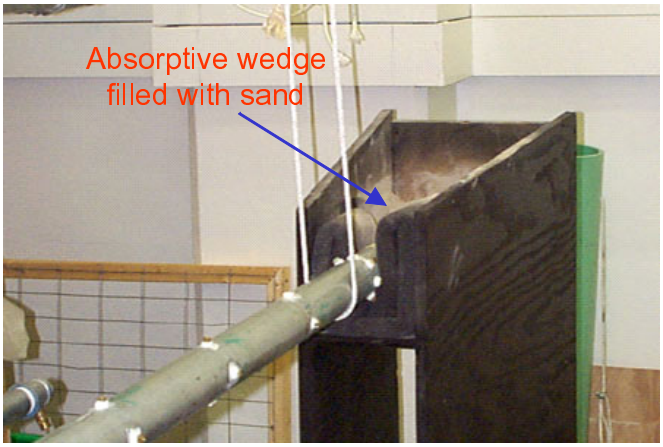

Figure 4.60. Absorptive wedge

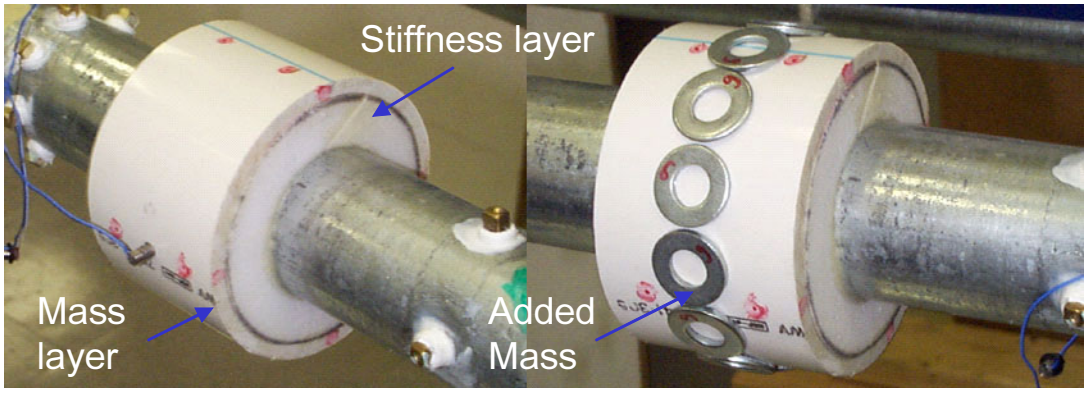

Figure 4.61. Initial and tuned DVA designs to control bending waves

The initial mass for the vibration absorber designed for bending waves was *222gr* and the tuned vibration absorber had a mass of approximately *348gr*. This mass, however, was not enough to cause a large impedance change to control extensional waves due to the weight ratio between the device and the pipe. The solution was to change the mass layer and the next vibration absorber was manufactured from a 3" schedule 40 steel pipe with a foam stiffness layer. This new vibration absorber had a natural frequency of *48 Hz* in the axial direction and can be seen in figure 4.62.

The last step in finalizing the design for the symmetric distributed vibration absorber was to design a DVA with matching or very close natural frequencies in both axial and radial directions. This would pin down the motion of the pipe at that chosen frequency. Figure 4.63 shows the last manufactured DVA. This DVA had a natural frequency of approximately 100 Hz in both axial and radial directions.

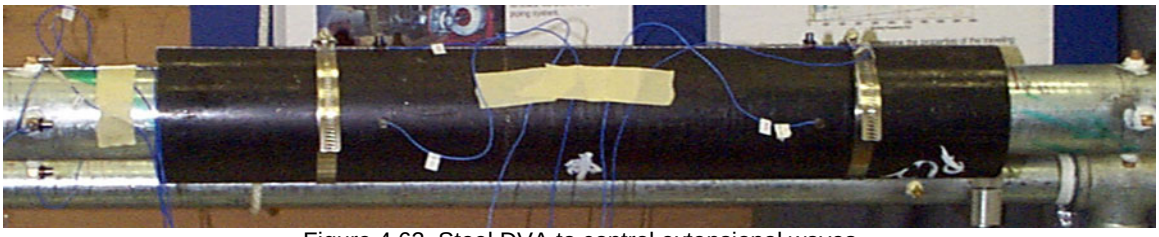

Figure 4.62. Steel DVA to control extensional waves

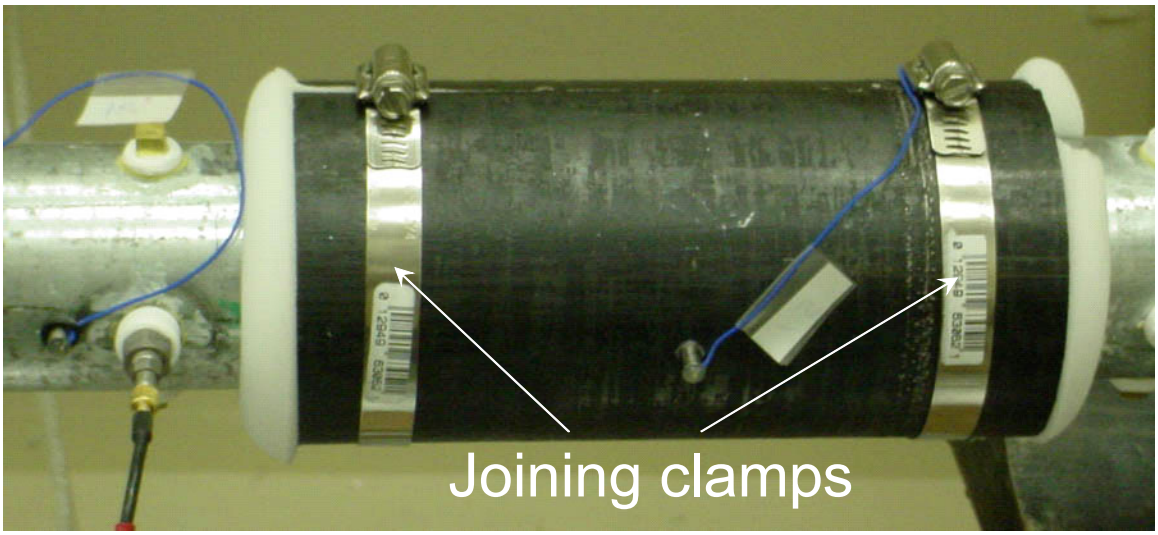

Figure 4.63. DVA with same natural frequencies in both radial and axial directions

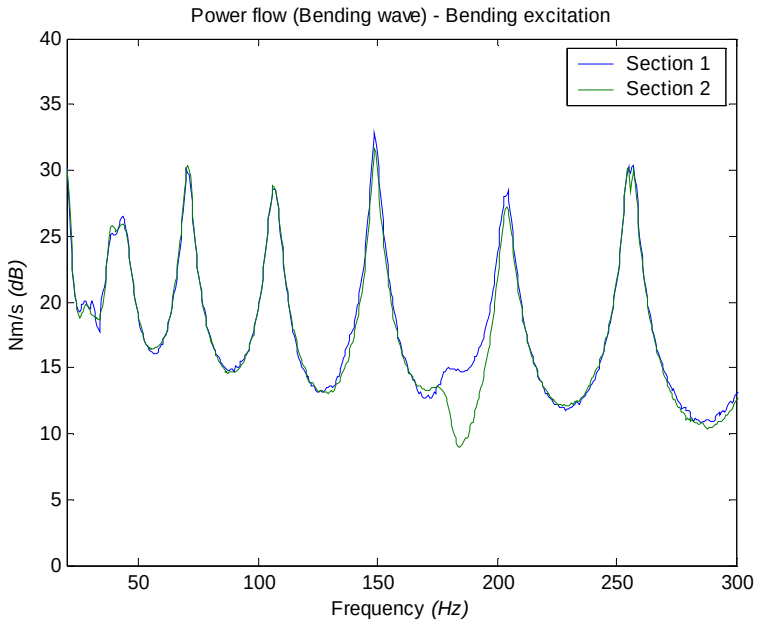

Figure 4.64. Power reduction in original DVA for bending wave

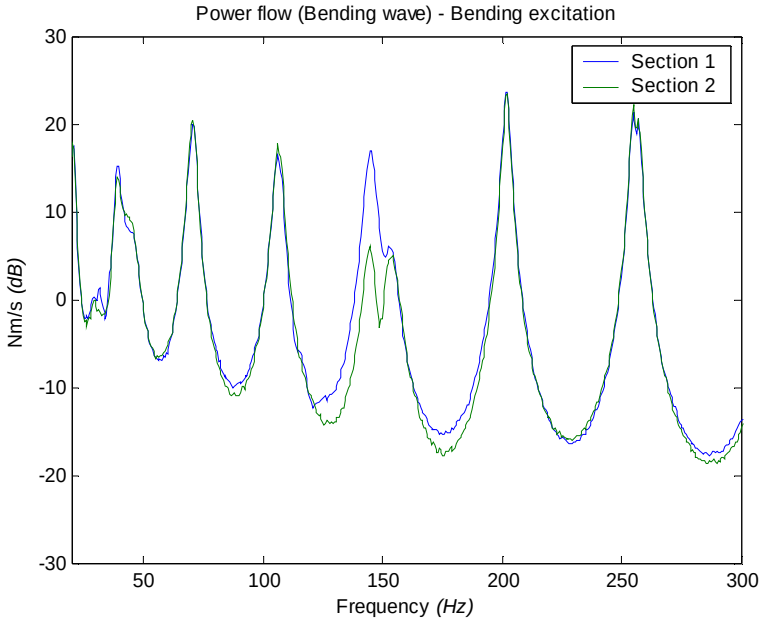

Figure 4.65. Power reduction in tuned DVA for bending wave

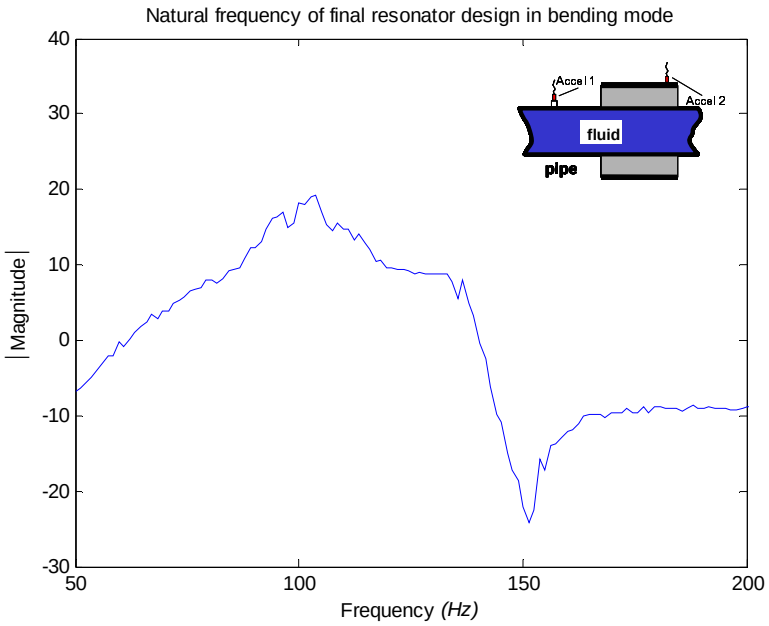

Figure 4.66. Frequency response of steel DVA in bending mode

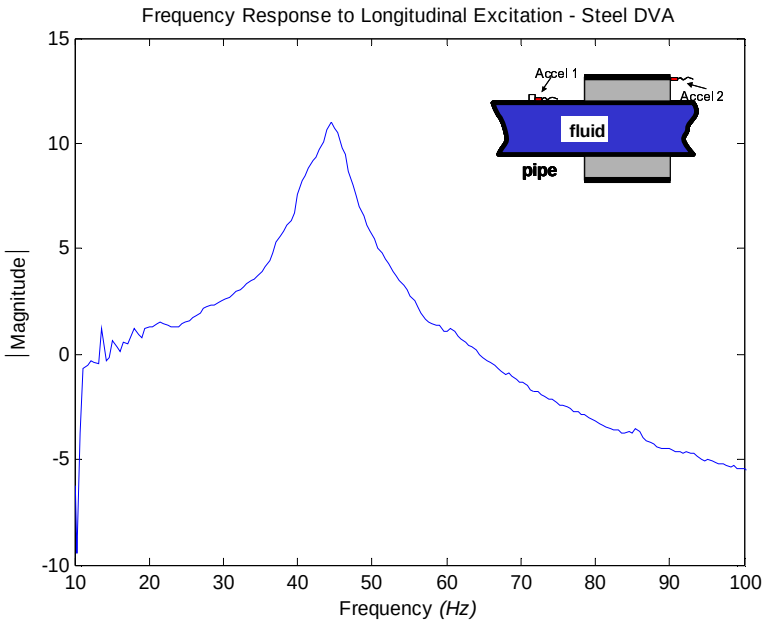

Figure 4.67. Frequency response of steel DVA

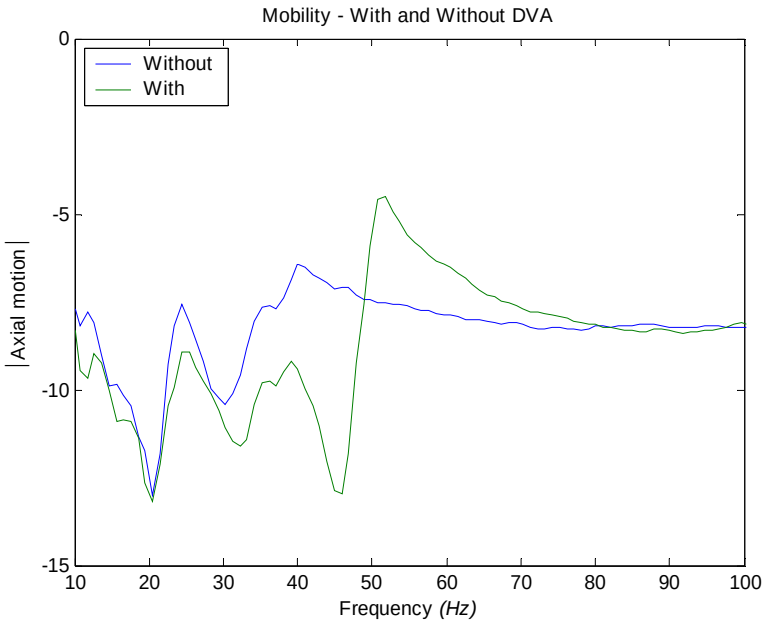

Figure 4.68. Mobility of pipe with and without the long steel DVA

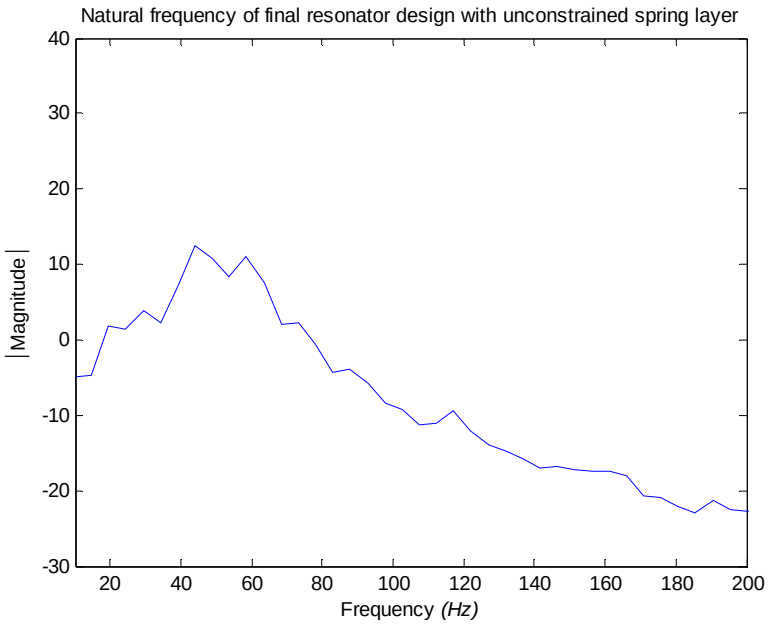

Figure 4.69. Natural frequency of final DVA design with unconstrained spring layer

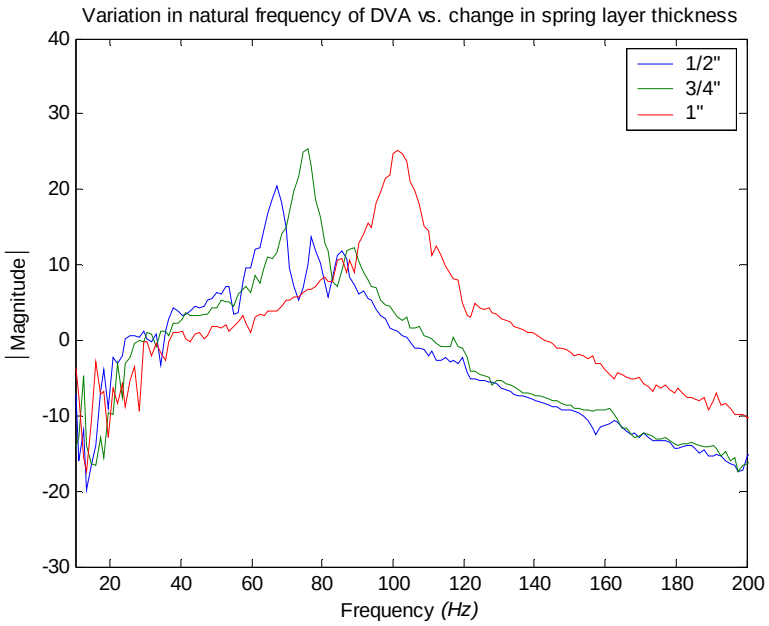

Figure 4.70. Variation of natural frequency with varying spring layer thickness

A classical dynamic vibration absorber attached to a pipe will not be very effective as it will work in one plane and waves traveling along a pipe often travel at different polarization angles. The symmetric dynamic vibration absorber overcomes this problem by removing the requirement for the absorber to work in a single plane. The absorber works in multiple planes via a continuous spring layer around the pipe and a continuous mass layer around that.

This device will not couple different traveling waves together and the polarization angle of the incoming bending wave does not matter. Furthermore, by changing the stiffness layer, we can change the normal and shearing properties and make the absorber have the same natural frequencies in both out of plane and axial directions. This allows for controlling of multiple wave types at the same frequency. The importance of flanking pathways in energy transmission has been shown by Kiyar, Johnson, & Fuller [53]. This

device targets the two shell waves that carry energy and the importance of this property will be evident later.

The performance of the vibration absorber in the bending mode is shown in figures 4.64 & 4.65. A reduction of about *5 dB* is achieved with the lighter PVC DVA and a reduction of about *8 dB* is achieved with the heavier PVC absorber. A shift in natural frequency from *184 Hz* to *148 Hz* is accomplished by increasing the mass of the absorber from *222gr* to *348gr* while keeping all other parameters the same, thus showing the ability to tune the resonator by changing the mass layer. The natural frequency of a dynamic vibration absorber is determined by placing a reference accelerometer right before the absorber and an accelerometer on the absorber and taking the transfer function between them. Figures 4.66 & 4.67 show the natural frequencies of the long steel DVA for the out of plane and axial modes, respectively.

It has been shown in section 3 that decomposing the longitudinal wave at low frequencies yields unreliable results. Therefore, the mobility of the system with and without the DVA was measured (see figure 4.68). The DVA pins down the total motion of the system at its design frequency which is *48 Hz*.

Another way of tuning the DVAs to different frequencies is to change the properties of the spring layer. Foam was used for the stiffness layer and the easiest way of changing the properties of spring layer is to squeeze thicker foam layers between the mass layer and pipe. Figures 4.69 and 4.70 show the changes in the natural frequency of the DVA with changing spring layer thicknesses. As expected, the natural frequency of the DVA increases with increasing stiffness of the spring layer.

4.8. Hybrid passive control device

4.8.1. Description

Sections 4.6 and 4.7 showed the principles and applications of symmetric Helmholtz resonators and symmetric distributed vibration absorbers, respectively. Both of these devices strive to overcome the energy transmission between different wave types through flanking energy transmission pathways. The symmetric Helmholtz resonator prevents the pipe shell from being excited through the motion of the mass in the neck area of a classical Helmholtz resonator and symmetric distributed vibration absorbers work to pin down the motion of the shell in the axial and radial directions, hence preventing energy transmission through flanking pathways.

In order to control the power flow in a fluid filled piping installation, all the wave types must be controlled simultaneously preventing energy transfer between wave types (see Kiyar, Johnson, & Fuller [54]). This is the concept behind the symmetric Helmholtz resonator – distributed vibration absorber combination (see figure 4.71). The design of the device ensures that all the wave types encounter a very large change in impedance at the design frequency.

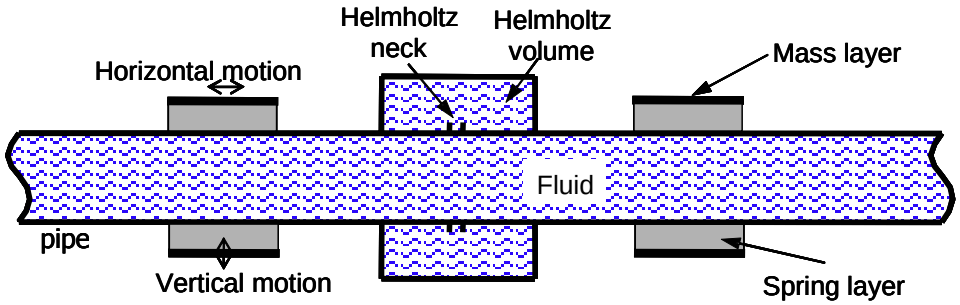

Figure 4.71. Hybrid (s-Helmholtz resonator + sDVA) control device

4.8.2. Results / Implementation

The Helmholtz resonator part of the passive control device was directly mounted on the steel pipe. A set of pre-drilled holes (test rig #1) used to mount studs were used for the neck section of the symmetric resonator.

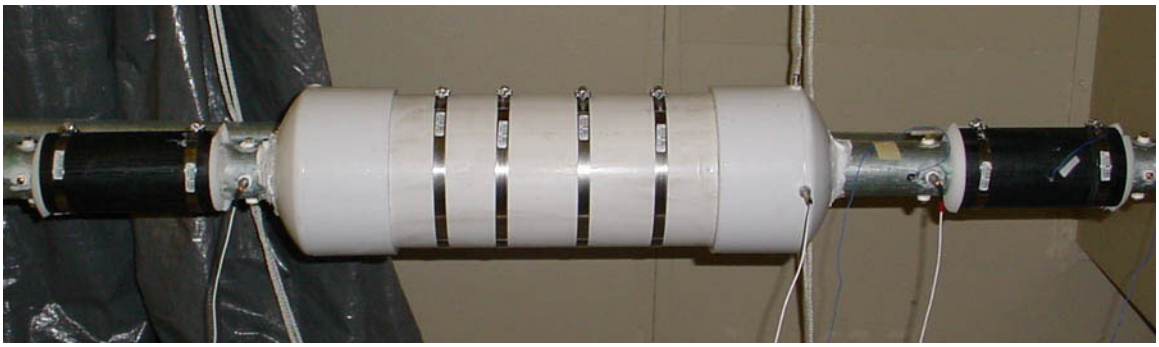

Figure 4.72. Hybrid control device incorporating s-Helmholtz resonator and sDVAs

The hybrid control device consists of a symmetric Helmholtz resonator flanked by symmetric-DVAs on both sides. The symmetric-DVAs had natural frequency of *100 Hz* in the axial direction (for the longitudinal wave) and natural frequency of *102 Hz* in the radial direction (for bending waves). The frequencies were matched by varying the thickness of stiffness layer (see section 4.7). The Helmholtz resonator had a slightly lower natural frequency than the natural frequency of the DVAs at *95 Hz*, but this was still close enough to the DVA's natural frequency that the device was able to target and control all traveling waves at the same time. Figure 4.72 shows the hybrid control device on test rig.

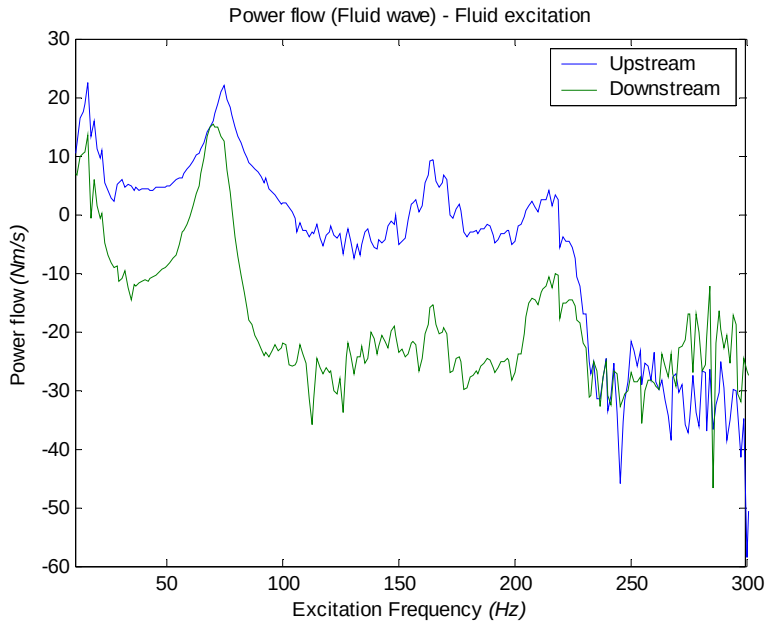

Figure 4.73. Comparison of power flow before and after hybrid control device

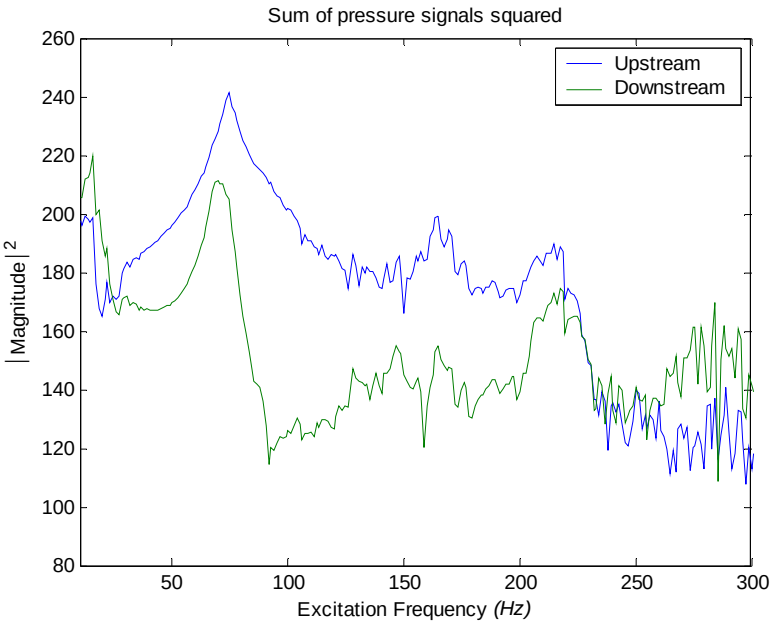

Figure 4.74. Comparison of pressure signals upstream and downstream

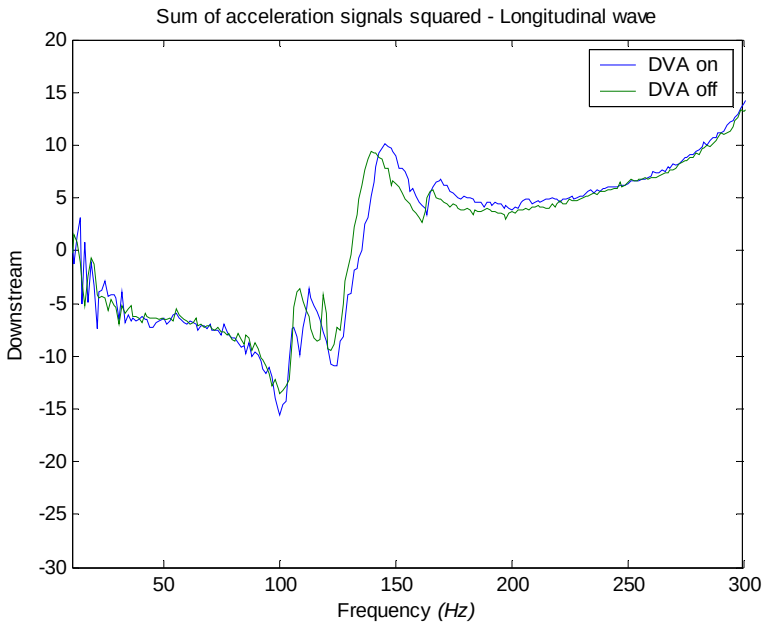

Figure 4.75. Comparison of axial acceleration signals downstream with and without DVAs

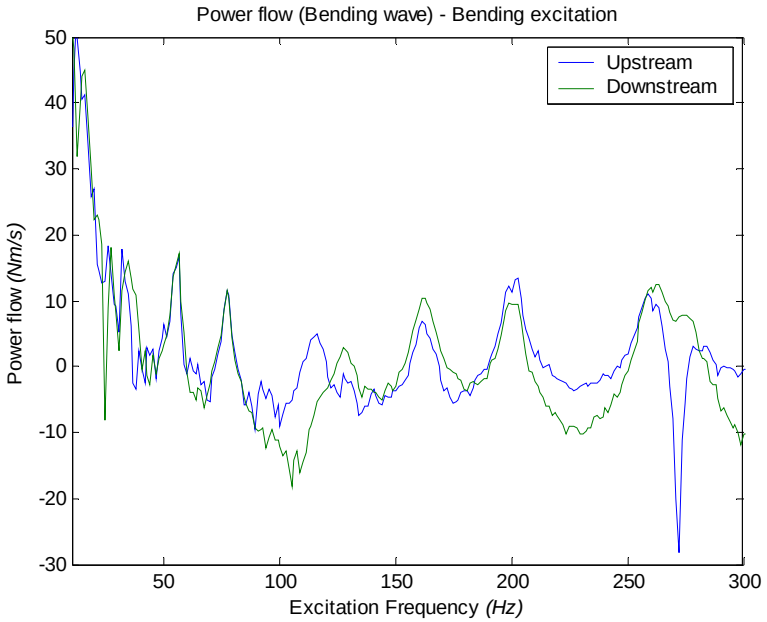

Figure 4.76. Comparison of power flow before and after hybrid control device

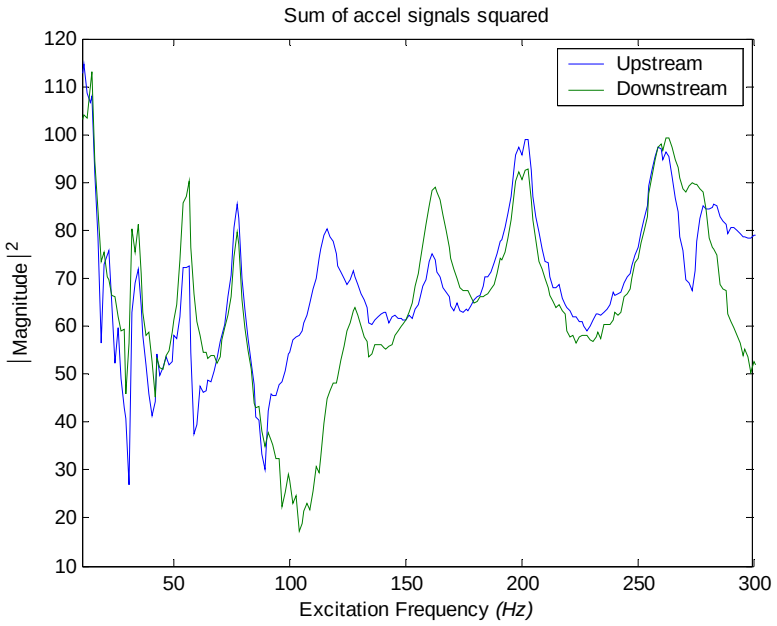

Figure 4.77. Comparison of radial acceleration signals before and after hybrid control device

Figure 4.73 compares the incident power of the fluid wave before and after the hybrid device. Figure 4.74 shows the pressure levels downstream and upstream. These two figures together show the Helmholtz resonator part of the symmetric device to work around *95 Hz*. The Helmholtz resonator section also suffers from the effect of bubbles as explained in section 4.2 and shown in section 4.6. The compliance caused by a soft shell and the accumulation of bubbles in the system create attenuations in the fluid wave at mid to high frequencies. Figure 4.75 shows the mobility of the system in the axial direction with and without the DVA. The mobility was measured instead of energy because an apsoptive wedge that would need to be attached at the end to provide absoption would be physically impossible to build. The motion of the system in the axial direction is pinned down at *100 Hz* by *3.5 dB*. Figure 4.76 compares incident power of the bending wave in the system before and after the hybrid device and figure 4.77 shows the acceleration levels in the radial direction. A reduction of *10 dB* in power at *102 Hz* for the bending wave is clearly visible.

As expected, the hybrid device controls fluid waves, bending waves, and longitudinal waves at around the same frequency at the same location. This prevents energy transfer between traveling wave types and improves the efficiency of the devices that make up the hybrid control device. The Helmholtz resonator part of the hybrid device can be tuned by changing the stiffness of the cavity shell. The removal of bubbles would be very important in this case, as the increase in stiffness caused by constraining the shell would be much less than the reduction in stiffness caused by bubbles in the system. The dimensions of the hybrid control device are also small compared to the size of the piping installation, thus providing an efficient tool in vibration control without putting extra loads on the supports.

4.9. Conclusions

A piping installation will generate unwanted noise in the form of structure-borne sound and fluid-borne vibrations, due to the heavy coupling between the waves in the system. Passive control devices are an integral part of noise control solutions for piping installations. This chapter provided an overview of various passive control devices finding application in piping installations. The properties and principle by which these devices function, the applications of these devices, and their flaws and/or limits were discussed.

The chapter started with an overview of the experimental setups used to compare these passive control devices. The importance of creating a reference point by which we could evaluate these devices was emphasized. Test rigs #1 & #2 were introduced and their properties were explained.

Simulation scenarios for various impedance discontinuities in a piping system were presented. The first scenario presented a rigid walled condition. The propagation of the fluid wave was not interrupted as would be expected from a continuous system. The second scenario presented a pressure release boundary condition. The pressure values in the downstream section were attenuated due to the pressure release boundary. The third scenario presented the change in the system behavior when a quarter-wavelength tube is inserted. The reductions in pressure downstream due to the quarter-wavelength tube were observed. The last scenario presented the system behavior when a bubble is present. This simulation showed a trend of decreasing pressure values with frequency. Lastly, pressure values along the pipe axis for test rig #1 were presented. The effect of bubbles in system response was represented as reductions in system response at mid to higher frequencies.

The first discontinuities to be analyzed were a rigid supporting structure and an isolation stand. Rigid stands are generally used to attach the piping installation to a structure. They are also used to control the motion of the pipe. Rigid stands will couple waves together and provide energy transmission between wave types. They will also provide for efficient conductors of vibration into the supporting structures induced by the bending motion of the pipe. This vibration, once in the structure, will then radiate sound. Isolation stands are used to isolate the vibrations of the piping installation from the structure. They are basically a spring attached to a structure, from which the pipe is suspended. They are effective in isolating the vibrations of the pipe from the structure. These devices can be characterized as a single degree of freedom system with base excitation (pipe). They, therefore, have a resonant frequency and around that frequency they transmit most of the vibrations in the pipe into the structure. The limiting factor in the amount of vibrations transmitted is the damping present in the stand.

The quarter-wavelength tube, a common control device suggested by engineers, was analyzed next. It has been shown that quarter-wavelength tubes work very well for the fluid wave. They make use of the phase change to create a change in impedance and reflect the fluid wave back to the source. The flaw in quarter-wavelength tubes is their physical shape. They work as cantilever beams for the shell waves and reduce the effectiveness of their application for the fluid wave by creating a flanking energy pathway. Another important factor that limits their application is the physical length requirement for the tube. The wavelength of the fluid wave at low frequencies is long, thus requiring long tubes. This puts a limitation on their application because of space requirements and limits their use to higher frequencies only.

The Helmholtz resonator is commonly found in piping installations. Like the quarter-wavelength tubes they work on the phase shift to control fluid pulsations. Unlike the quarter-wavelength tubes, they do not have the reoccurring harmonics, but work in a larger bandwidth. For this reason, they can be modeled as band-stop filters. They are also more compact than the quarter-wavelength tubes. They can be modeled as a single degree of freedom system with the mass of the fluid at the neck as the mass and the compression provided by the cavity as the spring. They function very well for the fluid wave right at the neck but the excitation of the base of the cavity provides for the excitation of the shell, which creates a flanking energy pathway and this energy couples back into the fluid downstream. It can be concluded that they are not very efficient in controlling pulsations in a piping installation.

The symmetric Helmholtz resonator developed during the course of this study strives to correct the problems associated with the asymmetry of the classical Helmholtz resonator. The necks are placed opposing each other, the cavity is made circular and

wrapped around the pipe. This device is axisymmetric and prevents coupling between wave types by canceling opposing excitations. The removal of the coupling between wave types provides for an efficient Helmholtz resonator and pressure levels measured along the pipe axis confirm these results when reductions provided by the classical and symmetric Helmholtz resonator are compared. This Helmholtz resonator can be made small with the selection of cavity material that is less stiff than metals. It can also be tuned by changing the stiffness of the cavity externally by clamping it.

Symmetric distributed vibration absorbers are designed to control the bending and longitudinal shell waves. The spring layer for the DVA is continuous along the pipe circumference and a uniform mass layer is wrapped around it. This single degree of freedom device is not affected by the changes in the polarization angle of the bending wave. The shearing and normal stiffness of the spring layer can be changed (or chosen) by selecting appropriate material. This allows for the device to have the same resonant frequency in both out of plane and axial directions, thus controlling both the bending and longitudinal wave at the same time.

It was also shown that the hybrid control device combines the fluid wave control of the symmetric Helmholtz resonator with the bending and longitudinal wave control of the symmetric distributed vibration absorber. This device controls all wave types present in the system without coupling them together. The removal of coupling between wave types provides for the efficiency of the device and reductions are not just limited to the small pipe section after the device, but rather to the complete downstream section.

Although the passive devices used to control fluid waves were designed as band-stop or notch filters, broadband reductions in mid to higher frequencies were also observed.

These are due to the bubbles in the fluid providing scattering or making the system more compliant. It should be noted that there was no pressure loading on the fluid except for the inverted Helmholtz resonator case, in which the pressure levels above the designed frequency were higher than the case with the Helmholtz resonator installed normally. A normally functioning fluid-filled piping installation will have some pressure to convey the fluid and the passive control devices will most likely work as they're designed.

Chapter 5

Active Control

This chapter will describe active control approaches for controlling structure borne and fluid borne vibrations in a piping installation. While there have been many studies about passive control devices and techniques, there is a limited application of active control techniques.

The chapter will start with the description of the experimental setup used to develop and test active control approaches. The sensors used during the experiments will be described and their roles as reference and error sensors will be presented. The actuators used in active control will be presented, which will be followed by the description for placement of these actuators and the presentation of techniques used in analyzing the effectiveness of actuators and their placement. Singular value decomposition, an effective tool for analyzing actuator placement, will be described. The chapter will end with the presentation of results obtained from the application of active control.

5.1. Experimental setup

A test rig was developed and consisted of an upstream section, which had two vibration isolation hanger systems, and a downstream section, which had a separable section for insertion of passive control devices and a 2 meter long clear PVC section for flow

visualization (see figure 5.1). The end of the downstream section had a water storage tank used to maintain regular water flow and the output of this tank was connected to the inlet of the pump (excitation source). The pump worked at a frequency just below *60 Hz*. The flow was constricted by a ¾" ball valve at the end of the downstream section right before the storage tank to load the system and induce pressure fluctuations. A pressure gauge was placed at the end of the upstream section to control and maintain the pressure load.

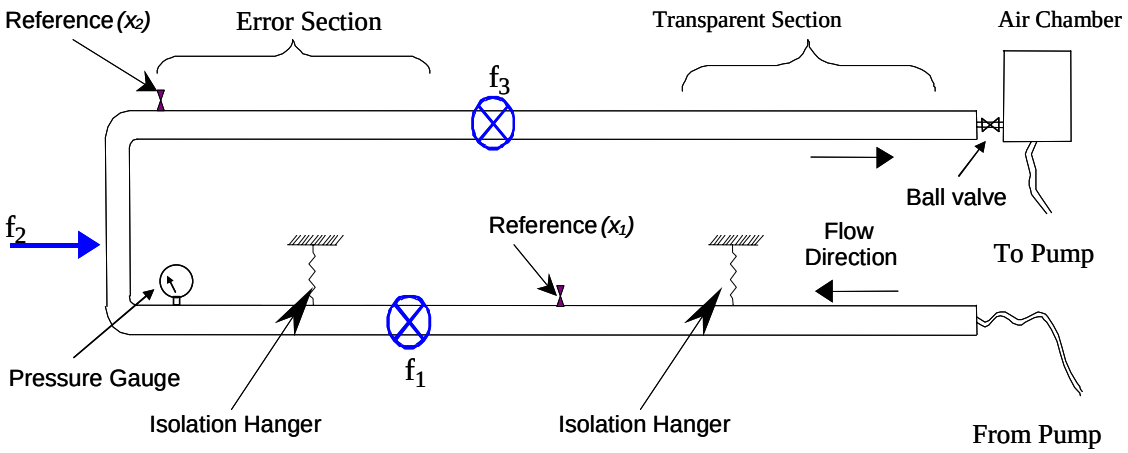

Figure 5.1. Schematic of experimental setup

A multi channel filtered X-LMS feedforward active control system (figure 5.2) was used to drive a set of actuators, attached to the pipe, in order to minimize the signals coming from a set of error sensors (*e*). The system used a pair of reference sensors (*x*) to drive the control filters (*W*) that in turn drove the actuators. The path between the input to the actuators and the output from the error sensors is termed the "plant" (*G*), a model of which is used to automatically adapt the control filter such that the error signals are

minimized. The disturbance (*d*) represents the signal as the error sensor before control (i.e. due to the pump).

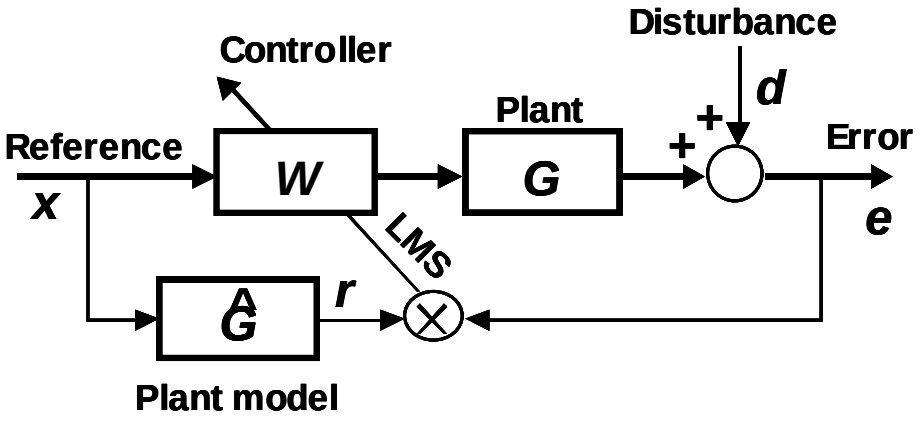

Figure 5.2. Schematic of X-LMS feedforward control

It is assumed that, although the controller is adapting, its coefficients are changing slowly compared with the timescale of plant dynamics, so that the error signal can be represented as:

$$e(n) = d(n) + w^T r(n) \tag{5.1}$$

where w is the vector of control coefficients and is given as:

$$w = [w_0 \cdots w_{I-1}]^T \tag{5.2}$$

and $r(n)$ is the vector of past values of the filtered reference signal and is represented as:

$$r(n) = [r(n) \cdots r(n-I+1)]^T \tag{5.3}$$

It is assumed that w is nearly time invariant, so that its dependence on time index *n* can be suppressed. *I* is the number of controller coefficients. Equations presented in 5.1

through 5.3 are for single channel filtered X-LMS feedforward control and were used for the sake of simplicity.

The basis of the LMS algorithm is to adapt the filter coefficients in the opposite direction to the instantaneous gradient of the mean-square error with respect to the coefficients. Thus, the gradient can be written as:

$$\frac{\partial e^2(n)}{\partial w} = 2e(n)\frac{\partial e(n)}{\partial w} = 2e(n)r(n) \tag{5.4}$$

where equation 5.1 and properties of vector derivations have been used to obtain the final part of equation 5.4. The final form of the control algorithm can thus be written as:

$$w(n+1) = w(n) - \alpha r(n)e(n) \tag{5.5}$$

which is known as filtered-reference LMS or filtered-x LMS, because the reference signal is generally represented by *x*. The algorithm was proposed by Morgan [61] and independently for feedforward control by Widrow [62] and for the active control of sound in ducts by Burgess [63].

The filtered reference signal will be generated using an estimated version of the true plant response represented as a plant model. This can be implemented as a separate real-time filter $\hat{G}(z)$, which is used to generate the filtered reference signal $\hat{r}(n)$ (see figure 5.2). *z* is the z-transform variable. The filtered-reference LMS algorithm prefilters the reference signal with the estimated plant response so the measured error signal and filtered reference signal are aligned in time to give a valid cross-correlation estimate.

The readers are encouraged to refer to Elliott [64], Fuller et al. [65], and Nelson et al. [66].

The controller was implemented on a set of Texas Instruments C40 DSP chips and the feed-forward control software, developed for VAL, was used to drive the system. A picture of the active control setup can be seen in figure 5.3.

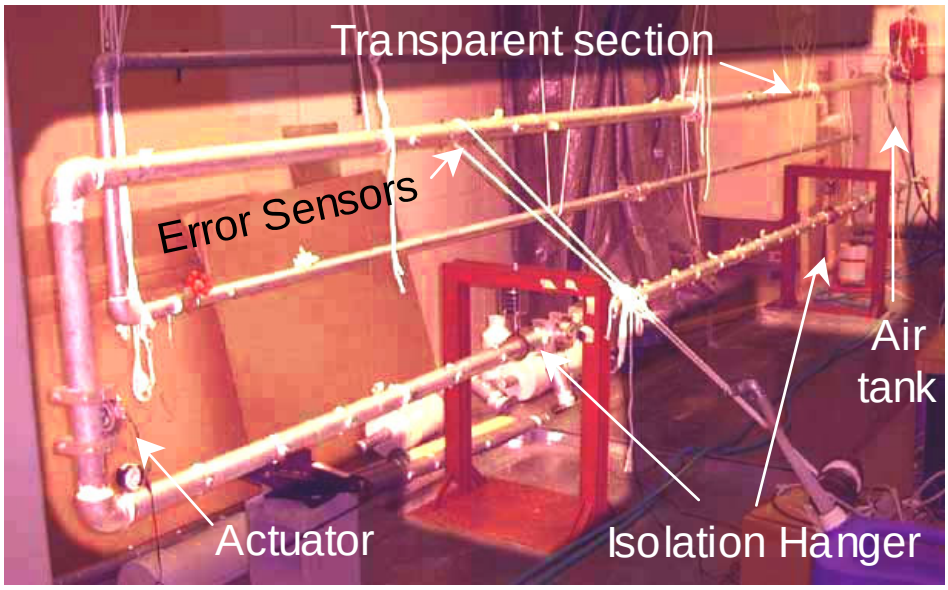

Figure 5.3. Experimental rig and active control setup

5.2. Sensors

This section will describe the error and reference sensors used during the active control tests and how they were placed on the test rig.

5.2.1. Error sensors

Six accelerometers and two pressure sensors were installed on the test rig for use as error sensors. Three experiments were conducted using a subset of error sensors. For the first set of experiments only acceleration signals were used as error signals. The

second set of experiments used only pressure signals. A final experiment using the complete set of error sensors was then carried out.

In principle, at least two sensors are needed to measure each wave type except for the bending wave which needs four sensors. The pressure sensors were attached to the pipe through ¼" tapped holes and mounted flush. Brass studs were attached to the pipe to mount the accelerometers. Brass was used to reduce the weight loading of the pipe. Four accelerometers were attached to the studs perpendicular to the pipe axis. These were used to pick up bending waves. Two accelerometers were attached parallel to the pipe axis to pick up the longitudinal wave (figure 5.4).

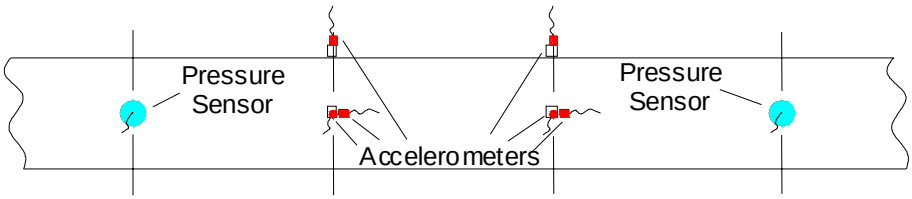

Error Sensors

Figure 5.4. Error sensor placements

5.2.2. Reference sensors

Two reference sensors were used for the active control setup. One sensor was placed at the middle of the upstream section while the other was placed at the beginning of the downstream section (figure 5.1). Both sensors picked up harmonic signals from the pump and broadband excitation that excited the natural dynamics of the system.

5.3. Actuators

Aura bass shakers (inertial actuator, see figure 5.5) rated at 4 ohms with 25 watts of output power were used as active control actuators (secondary source). Three actuators (one downstream, one upstream, and one along the short section) were attached to the system with custom designed bases (see figure 5.1 and 5.3). Aluminum was used to reduce the loading weight.

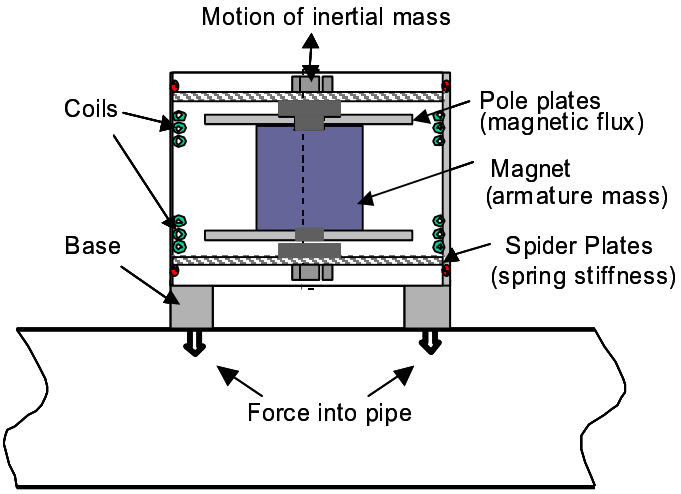

Figure 5.5. Inertial actuator attached to pipe

Figures 5.6, 5.7 and 5.8 show the power input from three actuators into the bending wave, longitudinal wave, and fluid wave, respectively. The control authority over the disturbance is directly related to the energy that can be put into the system by the actuators.

Actuator two is well coupled into the longitudinal wave and especially the bending wave. Since the actuators predominantly excite the pipe in the out-of-plane direction (*w*), it could be expected that the actuators mainly drive the bending wave. However, the waves are coupled together through the bends and discontinuities in the pipe. Therefore, all of the wave types are driven by the actuators. This means that non-

invasive actuators can be attached to the outside of pre-existing piping systems in order to control all of the waves traveling along the pipe including fluid waves.

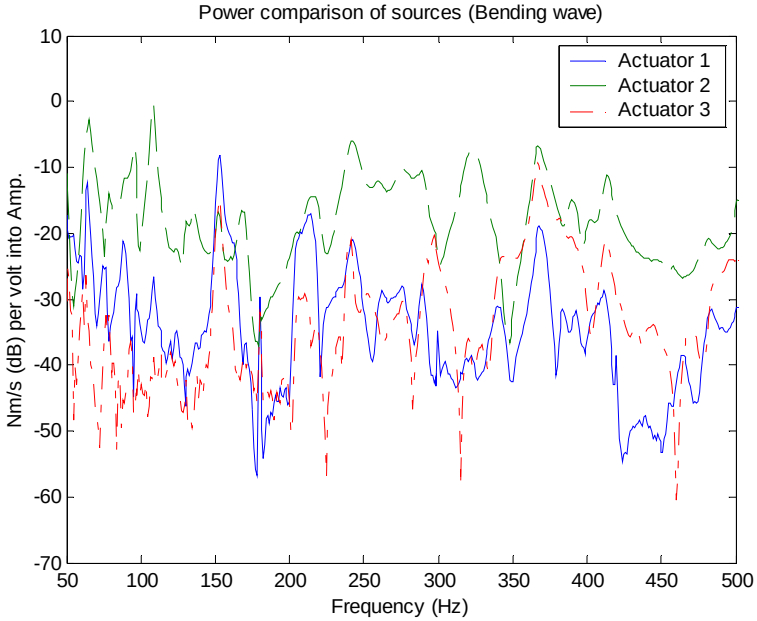

Figure 5.6. Power from actuators into bending wave

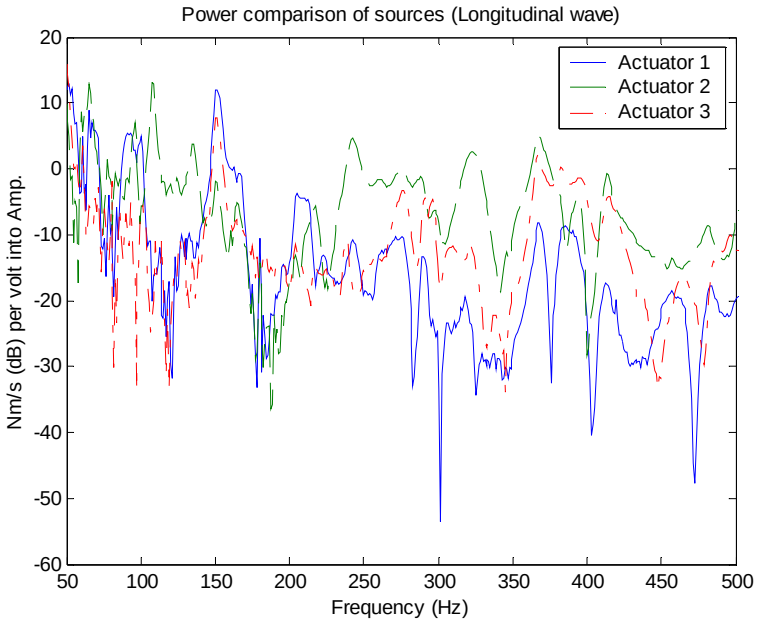

Figure 5.7. Power from actuators into longitudinal wave

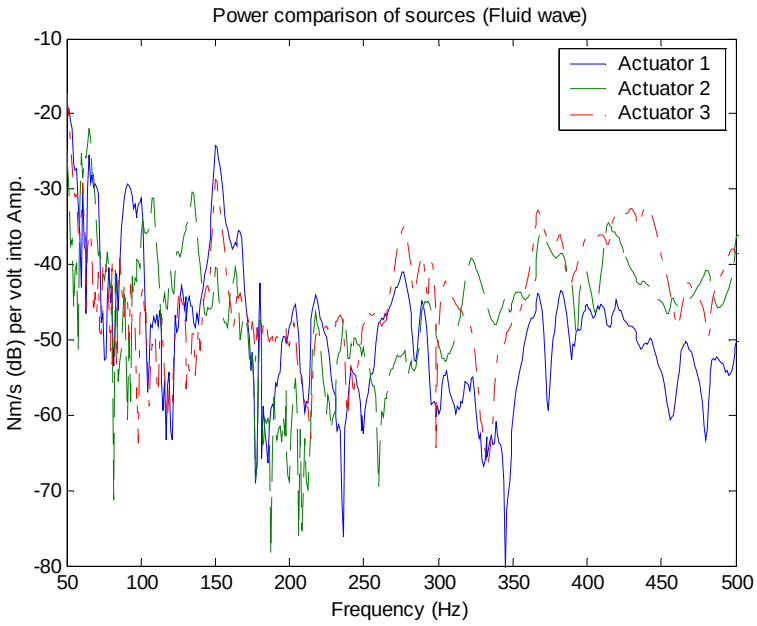

Figure 5.8. Power from actuators into fluid wave

5.4. Positioning of actuators and SVD

If it is assumed that the reference signals are coherent with the errors and that sufficient error signals are used to monitor the system, then the limitations in performance due to the actuators can appear in two ways: (i) an insufficient number of actuators are used to control all of the degrees of freedom in the system or (ii) there are enough actuators but they are not coupling into the system independently (for example placed too closely together). The second problem was of interest in this work since the pipe was only excited by external radial forces and it was important to determine whether all of the wave types could be "independently" excited. To investigate this, a singular value decomposition method was employed.

A complex matrix A of the form $L \times M$ can be factorized using singular value decomposition:

$$A = U\Sigma V^H \tag{5.6}$$

where the $L \times L$ matrix *U* and $M \times M$ matrix *V* are generally complex, but unitery so that $U^H U = UU^H = I$ and $V^H V = VV^H = I$, and if $L > M$, then the $L \times M$ matrix Σ can be written as:

$$\Sigma = \begin{bmatrix} \sigma_1 & 0 & \cdots & 0 \\ 0 & \sigma_2 & & \vdots \\ \vdots & & \ddots & \vdots \\ 0 & & & \sigma_M \\ 0 & \cdots & \cdots & 0 \\ \vdots & & & \vdots \\ 0 & \cdots & \cdots & 0 \end{bmatrix} \tag{5.7}$$

where σ_i are the non-negative singular values of *A*.

The transfer functions between each of the three actuators and eight error sensors were measured to obtain an 8x3 matrix of filters. At each frequency the singular value decomposition was then applied to this matrix to yield three matrices of the following form:

$$[T] = [U][\Sigma][V]^H \tag{5.8}$$

where *T* is the 8x3 transfer function matrix, *U* is the left singular vector matrix (8x8), Σ is the diagonal singular value matrix (8x3), and V^H is the right singular vector matrix (3x3). Figure 5.9 shows the normalized singular values from the actuators to errors as a function of frequency. It can be seen that the first two singular values are quite large but the third (and smallest) singular value is fairly small (*-20 dB*). This implies that the three

actuators are independently coupled into the error sensors in mainly two ways. This result could mean that either (i) the piping system only has two important degrees of freedom or that (ii) the actuator configuration could be improved. It is more likely that case (ii) is true and it will be important in the future to use more actuators and a larger variety of actuator locations. The result is not unreasonable given that the actuators are all mounted to the outside of the pipe and act in a radial direction.

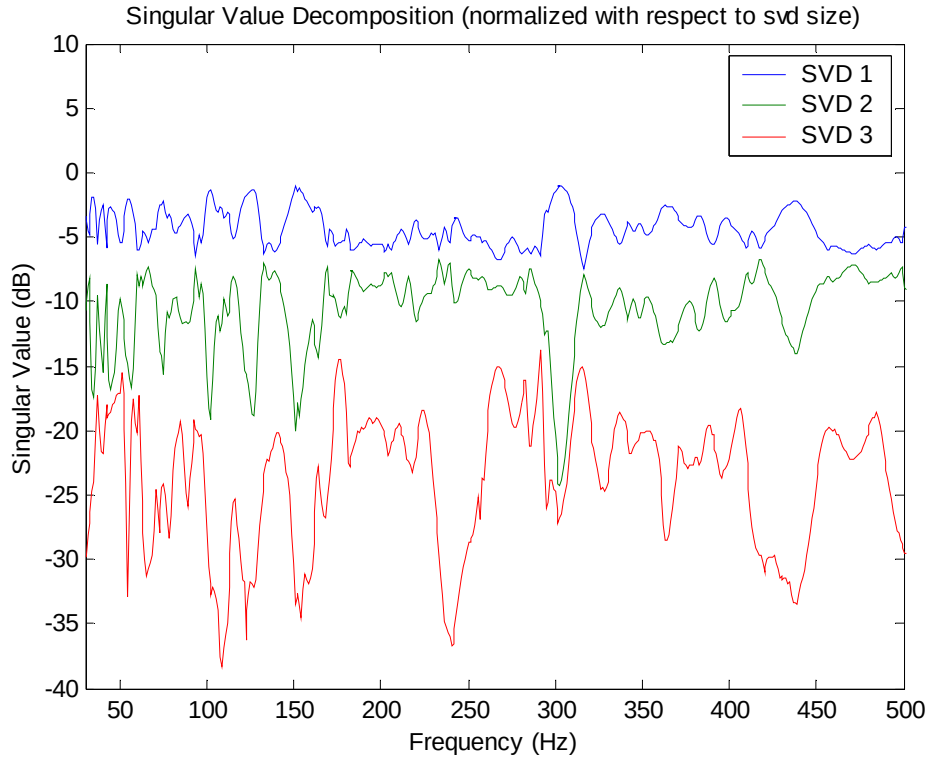

Figure 5.9. Normalized singular values from actuators to errors as a function of frequency

5.5. Primary disturbance

Figure 5.10 shows the power traveling downstream in the error sensor section of the pipe (in Nm/s) due to the action of the primary source (in this case the pump) for each wave type present in the system. It can be seen that the longitudinal wave carries the most energy in the system at low frequencies. Pump harmonics are dominant, but flow also causes some broadband excitation. Although the harmonics carry most of energy, the natural modes of the system can cause large response at resonance due to low-level broadband excitation.

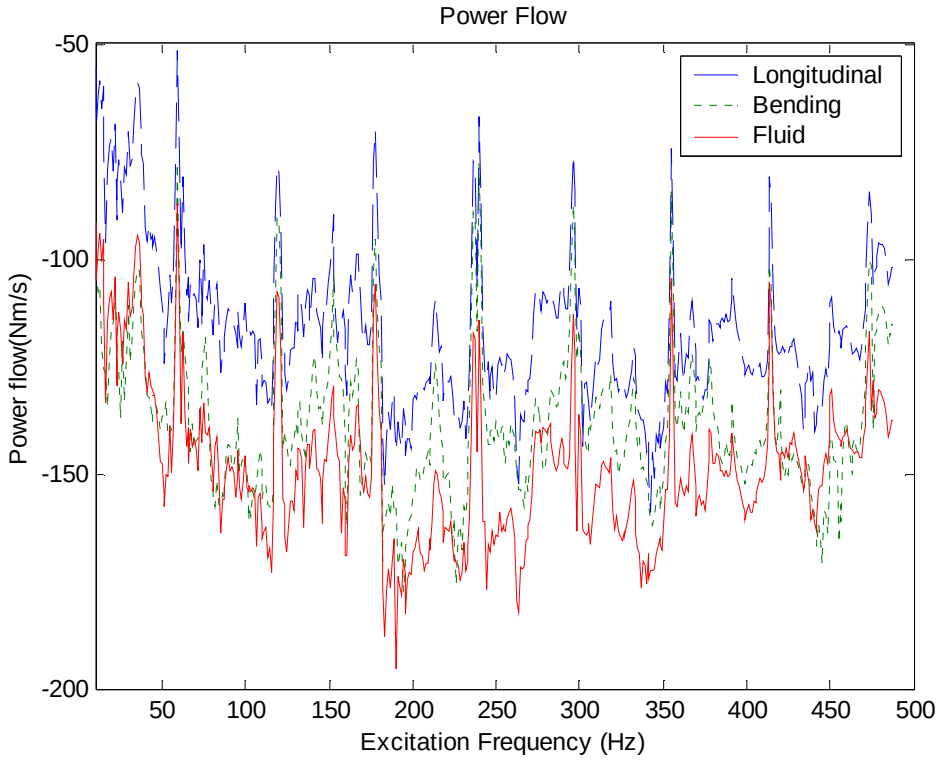

Figure 5.10. Power traveling downstream through error section due to action of primary source (pump)

The disturbance signal can also be analyzed using the singular value method. Taking the transpose of the left singular vector matrix (equation 5.8) and multiplying that by the

disturbance signals from the primary source yielded the 8x1 disturbance vector in modal coordinates:

$$[\mathbf{g}] = [U]^T [d] \tag{5.9}$$

where *g* is the 8x1 disturbance vector in modal coordinates, U^T is the transpose of the left singular vector, and *d* is the vector that contains the disturbance signals. The *d* vector consists of the transfer functions between error sensors and reference #2 (i.e. reference #2 used to provide a phase reference).

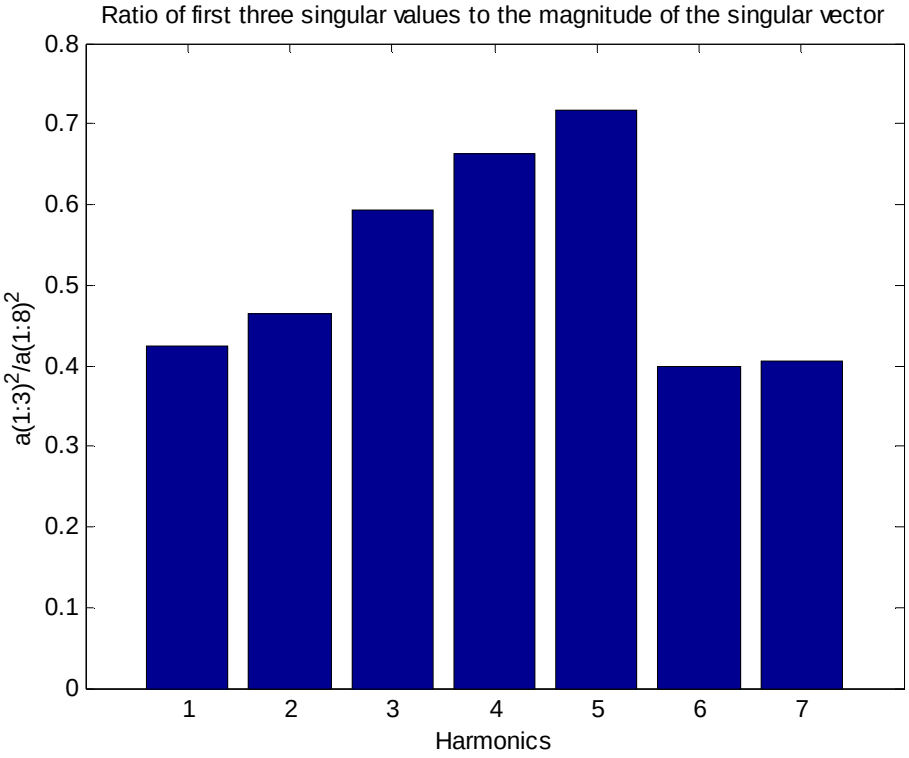

Figure 5.11. Ratio of first three values squared to magnitude squared

Since there are three actuators, only the first three values in the disturbance vector *g* can be controlled where the other five represent the uncontrollable part of the disturbance. Figure 5.11 shows the ratio of the first three values of the disturbance vector squared to

the magnitude of all eight disturbance vector values squared at the harmonics of the pump. This represents the ratio of “energy” that can be removed by the control system.

This shows that the 4th and 5th harmonics are likely to be the easiest to control and this is borne out in the experimental results (following sections).

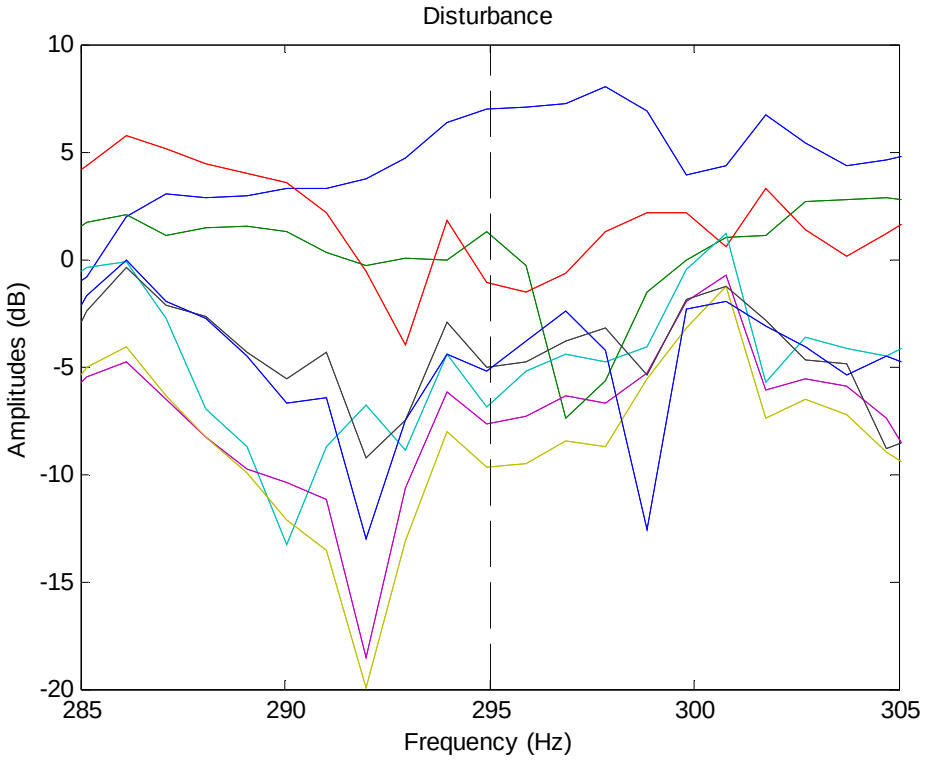

Figure 5.12. Disturbance vector filtered through SVD (i.e. in modal coordinates)

Figure 5.12 shows the disturbance signals in modal coordinates (*g*) for the fifth harmonic (*295 Hz*). In general, the first three disturbances are dominant over the other five and therefore significant reductions can be achieved. However, the five uncontrollable disturbance values are still significant in size. This bears out the former conclusion that the system has more than two important degrees of freedom and that more and better placed actuators would improve performance.

5.6. Results

Previous sections gave background on the active control experiments. This section will present the results obtained from three active control experiments: (i) active control experiments where acceleration signals were used as error signals, (ii) experiments where pressure fluctuations were used as error signals, and (iii) experiments where a hybrid array of sensors consisting of pressure transducers and accelerometers were used as error sensors.

5.6.1. Control using acceleration signals as errors

Figures 5.13 and 5.14 show the sum of the squared acceleration and sum of the squared pressure signals obtained using only acceleration signals as error signals (six errors). This setup achieved a reduction of *16.4 dB* in shell waves, but only a reduction of about *1.6 dB* in the fluid wave in *50 Hz* to *450 Hz* range.

5.6.2. Control using pressure signals as errors

Figures 5.15 and 5.16 show the results of active control where only the two pressure sensors were used as errors. The reduction obtained from this setup was about *7 dB* in fluid wave over the *50 Hz* to *450 Hz* range, whereas there was very little reduction in the shell waves (a reduction of *.6 dB*) and the level at some locations even increased.

5.6.3. Hybrid system (control using both acceleration and pressure as error signals)

Figures 5.17 and 5.18 show the results of the active control setup where a hybrid system (a combination of acceleration signals and pressure signals) was used (eight errors). This approach gave us a reduction of approximately *16.5 dB* in shell disturbances and *12.8 dB* in fluid disturbances in the *50 Hz* to *450 Hz* range.

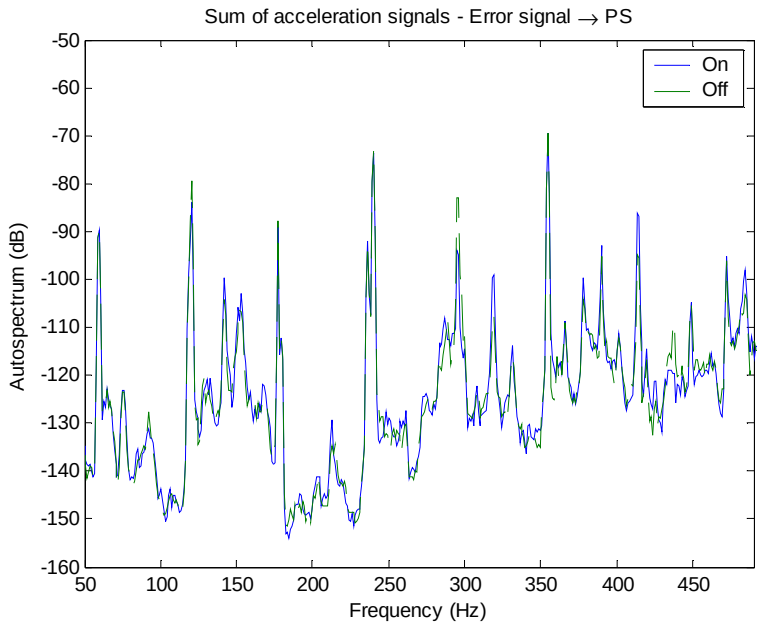

Figure 5.15. Sum of squared acceleration signals when pressure transducers are used as error sensors

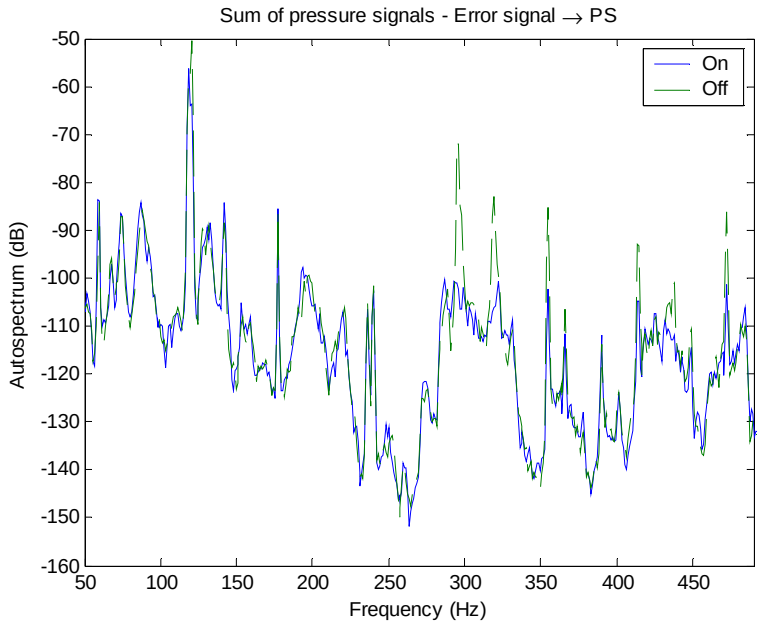

Figure 5.16. Sum of squared pressure signals when pressure transducers are used as error sensors

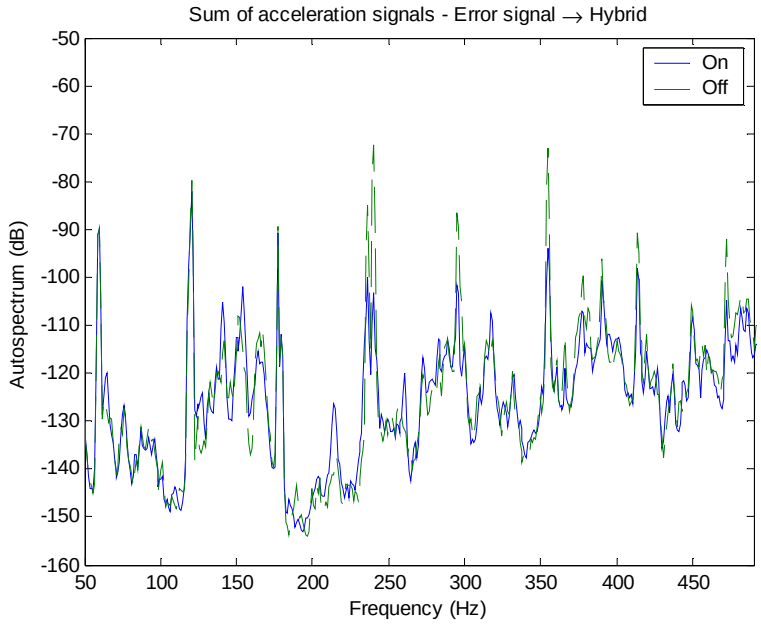

Figure 5.17. Sum of squared acceleration signals with hybrid (accelerometers and pressure transducers) error sensors

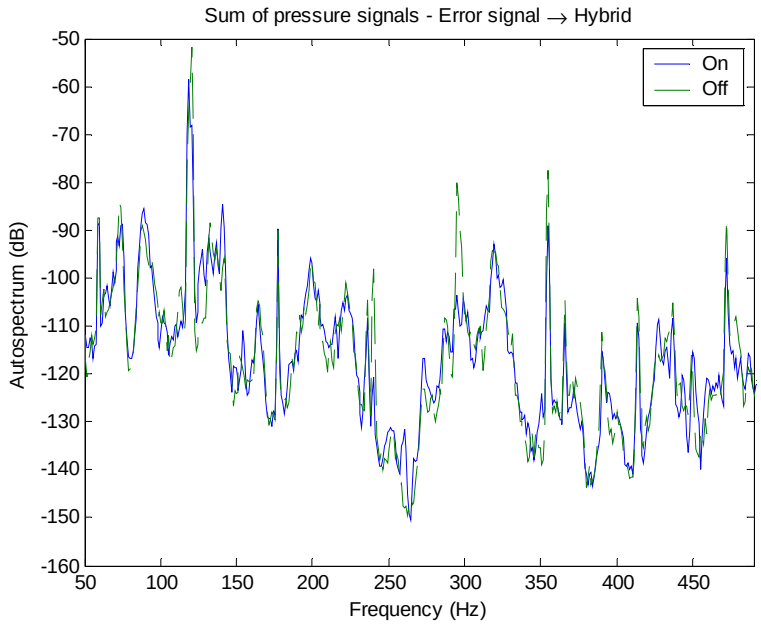

Figure 5.18. Sum of squared pressure signals with hybrid (accelerometers and pressure transducers) error sensors

5.7. Conclusions

It has been shown (Kiyar, Johnson, & Fuller [53]) that when a wave encounters a discontinuity, it will be scattered into other wave types. Therefore the energy transmission pathways are usually complex and difficult to analyze. In order to achieve good control, all of these pathways have to be controlled at the same time in order to prevent the energy circumventing the control treatment.

This section presented a method of using the natural scattering property of discontinuities to allow actuators applied to the outside of the pipe to couple into all of the wave types. This is done by placing the actuators at different positions along the pipe with discontinuities (in this case bends in the pipe) between the actuators and the error sensors. In order to investigate the coupling of the actuators to the error sensors a

singular value decomposition method was used. The transfer functions between the three actuators and the eight error sensors were measured and grouped into matrix form. A singular value decomposition was performed on this matrix at every frequency and it was determined that the actuators were indeed effectively coupling into the different waves in the system but that the actuators only coupled into the errors in two “independent” ways. It is likely that additional actuators and different actuator locations would improve performance and this is the focus of future work. Disturbance signals generated by the primary source were filtered through the left singular vector matrix to yield a disturbance vector in modal coordinates from which the amount of control authority and degrees of freedom of the system could be determined. It showed that reasonable control could be achieved but that more actuators were necessary.

Active control was performed for three different sets of error sensors. (i) only structural error sensors, (ii) only pressure sensors and (iii) a hybrid system using both structural sensors and pressure sensors. Results show that control can be targeted at specific wave types but that doing this can actually cause an increase in the amplitudes of other waves. For this reason a hybrid solution is best and it was demonstrated that both structural and acoustic waves could be simultaneously controlled using structural actuators that only applied forces in the radial direction. Most of the peaks in the energy graphs presented in this section were caused by excitation due to a pump. However, some of the smaller peaks in the energy graphs are related to the free resonances of the system and reductions of these resonances were also obtained.

Chapter 6

Conclusions and future work

The goal of this work was to study the physical mechanisms behind the behavior of fluid-filled steel pipes and to develop viable active and passive tools to control the coupled fluid-borne and structure-borne energy flow. This chapter will start by briefly describing the work done during the course of this project followed by the descriptions of significant knowledge learned and significant contributions of this work in the field of fluid-filled piping installations and noise control solutions for fluid-filled pipes. The chapter will end with some suggestions for future work by the author.

6.1. Summary of work done

Multiple tasks were carried out simultaneously for this project. There were two aspects to these tasks: (i) the construction of testing hardware and (ii) development of test methodologies. The first article that needed to be carried out for the development part was the execution of a comprehensive literature review of present studies on fluid-filled pipes and circular shells.

The literature review comprised studies of journal articles, theses, and reference books and was divided into following sections: (i) research on shell theories, (ii) research on fluid-filled cylindrical shells, (iii) research on fluid-filled pipes with flow, (iv) research on present experimental work, (v) research on discontinuities in fluid-filled pipes, (vi)

research on control approaches for piping systems, and (vii) other miscellaneous research.

An understanding of the physics for the fluid-filled pipes and experimental methodologies was necessary since the goal of this work was to develop noise and vibration control solutions for fluid filled pipes. Thin shell theories used in the modeling of cylindrical shells were analyzed and the formulations for *in vacuo* cylindrical shells were investigated. This research was later expanded to include the effects of heavy fluid loading on fluid-filled cylindrical structures and the propagation of waves in a coupled fluid-shell structure. The next task was to review the recent studies on experimental technologies and the effects of discontinuities in fluid-filled pipes. The literature review was completed with assessments of existing control approaches and other miscellaneous research on fluid-filled pipes.

Many authors have tackled the theoretical aspect of fluid-filled pipes, i.e. mathematical modeling of *in vacuo* cylindrical shells and coupled fluid-filled cylindrical shells. The investigation and formulation of governing equations of fluid filled pipes are widely reprinted in the literature. The research on experimental sensing methodologies for fluid-filled pipes appears to have been mostly carried out by the same researchers. Most of these works were carried out on vertical standing fluid-filled shells. Although developing experimental methods and verifying theoretical models on vertical standing test rigs yield satisfactory results, it lacks the uncertainty and indeterminate effects found in realistic piping installations. This kind of research has to account for the change in pressure along the pipe axis, but due to its setup, cannot account for various phenomena like bubbles, bends, etc. Another deficiency in these studies is the lack of consideration of the coupling between the shell and fluid. Most of these studies

investigate waves present in a system separately. Research on discontinuities in fluid-filled pipes and control approaches for these systems is scarce at best.

The next step in the development process was the formulation of a mathematical model to represent the physical system. To aid in this process, the equations of motion for the shell and fluid were derived and solved to yield the Love equations and the acoustic wave equation that govern wave propagation in an infinitely long fluid-filled circular pipe. The dispersion equation was derived using the Donnell-Mushtari shell theory. The dispersion curves were then plotted and using the dispersion equation and compared with dispersion curves obtained from the experimental test rig. This was also a verification of the mathematical model of the physical system. The last step of the mathematical modeling was the formulation of energy expressions for the different wave types present in the system.

Present measurement methods were investigated and were evaluated on the development rig. These experimental methods, with the exception of the four-channel method, mostly decomposed traveling waves one at a time and the effect of coupling on wave propagation was neglected. The more sophisticated four-channel method measures two coupled traveling wave types, but it still didn't yield satisfactory results. A new wave decomposition method using multiple transducer arrays to acquire multiple waves was developed to overcome this problem.

The second part of the project comprised experimental work. To this end, two test rigs were designed and constructed to carry out the experiments. The first rig was built around a 21' (~6m) galvanized steel pipe. Holes with a diameter of 1/8" were drilled at 25 cm intervals along the pipe and tapped to mount brass studs. These holes served as

mounting points for pressure transducers and also functioned as mounting bases for accelerometer arrays. The pipe length was chosen, such that one wavelength of extensional wave at *100 Hz* would fit along the pipe axis. The ends were capped with an iron cap at one end and a diaphragm at the other end to roughly simulate free-rigid boundary conditions for the fluid wave and free-free boundary conditions for the shell waves. This rig was used to validate the theory behind the physical behavior of fluid-filled pipes (wavenumbers) and to develop the sensing methodology (wave decomposition). The correlation between wavenumbers obtained through experiments and wavenumbers calculated using theoretical models was verified. The importance of these findings resulted in the ability to use wavenumbers calculated using theoretical modeling in wave decomposition instead of the wavenumbers that needed to be calculated each time a test was run, thus reducing overhead in post-processing. A second rig was built to test and characterize discontinuities. It offered a standard test procedure and repeatability by which a comparison could be made between various discontinuities.

Typical discontinuities and passive control devices that can generally be found in piping installations were investigated. Most of these classical control devices had flaws in their design and their lack of efficacy was presented. New passive control devices that improved on classical control principles were designed and tested. An active control method utilizing external actuators was implemented and an analysis of this approach was performed by singular value decomposition.

6.2. Significant new knowledge learned

A piping installation consists of many different parts that act in unison to convey energy and fluid. Bends, supports, noise control devices, and any other device that leads to a change in flow direction or disrupts the flow (like mufflers) will act as a discontinuity. Any discontinuity in a pipe with traveling shell waves and fluid waves will distribute energy between waves due to the heavy coupling between the shell and the fluid. This effect renders many control approaches ineffective.

This effect was first noticed during the post-processing of data from a simple flange discontinuity when energy was transferred between shell waves (probably due to imperfections in the connection). Consecutive analyses of other typical discontinuities substantiated these findings. The coupling of energy between different wave types presented contradicting possibilities as (i) reduction in efficiency of classical passive control devices, resulting in unfavorable conditions in the form of flanking energy pathways, and (ii) the possibility of utilizing this effect in novel control approaches. This section will discuss the unwanted effects of flanking energy pathways.

The definition of a flanking energy pathway is transmission of energy outside a proposed control pathway. The most typical flanking energy pathway in a piping system occurs when a discontinuity lacks axisymmetry. This becomes especially important due to the heavy coupling between the fluid and the shell. To this end, many classical control devices suffer from flanking due to asymmetry.

Supporting structures are an essential part of any physical system. Supporting structures in piping installations come in two forms: (i) rigid stands, where the pipe is

typically clamped and (ii) isolation stands, where an isolator is installed between the pipe and the structure. Isolation stands can be in the form of spring elements to reduce vibration transmission into structure or in the form of a seismic shock absorber. The effects of these two typical piping elements on the installation were investigated. Rigid stands will couple waves together and provide energy transmission between wave types. They will also provide for efficient conductors of vibration induced by the bending motion of the pipe. This vibration once in the structure will cause every efficient radiator to radiate sound. They are sometimes used to control the lateral motion of a pipe and this situation will lead to an inadvertent increase in efficiency of vibration transmission into the structure. Isolation stands can be modeled as a single degree of freedom system as they are basically a spring attached to a mass (a section of the pipe). They will transmit energy into the structure around their resonant frequency. They may or may not transmit energy above their resonant frequency depending on their installation. They will act mass-like and transmit energy if both ends of the spring element are attached to the pipe and support.

Many of the passive control devices studied showed broadband reductions where only a notch filtering effect was expected. Simulation scenarios were carried out to investigate these phonemona. The effects of inserting specific impedance values at a control volume in the middle of a pipe were studied. The results showed that the addition of a bubble caused drops in the system response in the form of pressure values at mid to high frequencies.

Next to be analyzed were two control devices that work on the same principle. Both the Helmholtz resonator and the quarter-wavelength tube make use of the phase change to create a change in impedance to control fluid pulsations. The main difference between

the quarter-wavelength tube and the Helmholtz resonator is the lack of reoccurring harmonics that exist in a quarter-wavelength tube. However, the control bandwidth of a Helmholtz resonator is greater depending on the size than the control wavelengths of the quarter-wavelength tube. Although the quarter-wavelength tubes function well in controlling fluid waves, their flaw lies in their non-symmetric physical design. They work as cantilever beams for the shell waves and reduce the effectiveness of their application for the fluid wave by creating a flanking energy pathway. Another important factor that limits their application is the physical length requirement for the tube. The wavelength of the fluid wave at low frequencies is long, thus requiring long tubes. This puts a limitation on their application because of space requirements and limits their use to higher frequencies only. Helmholtz resonators function very well for the fluid wave right at the neck but the excitation of the base of the cavity provides for the excitation of the shell, which creates a flanking energy pathway and this energy couples back into the fluid downstream. Therefore, it can be concluded that they are not very efficient in controlling pulsations in a piping installation. Like the quarter-wavelength tubes, they also have flaws associated with being asymmetric and work to couple waves together.

The limitations of classical passive control devices lie in their physical design. Most of these devices are asymmetric and allow for transfer of energy between different traveling waves. Any device that has flanking energy pathways will be rendered ineffective as a noise and/or vibration control solution. This predicament emphasizes the importance of multiple wave type control, preferably at the same location, to inhibit flanking energy pathways. The problem of asymmetry, taken into account with flanking energy pathways, required a different approach. The symmetric Helmholtz resonator and symmetric distributed vibration absorber were the answers to this problem.

6.3. Significant techniques found

Several important innovations were conceived during the course of this study. These innovations can be broken into two sections: (i) novel control methods and (ii) an improved measurement methodologies. Novel control methods comprise the symmetric Helmholtz resonator to control fluid pulsations and the symmetric distributed vibration absorber to attenuate shell waves, as well as externally actuated active control of fluid-filled pipes. Coupled wave decomposition, factoring in the effect of heavy coupling between the fluid and the shell, is the main concept behind improved measurement methodologies.

The symmetric Helmholtz resonator developed during the course of this study strives to correct the problems associated with the asymmetry of the classical Helmholtz resonator. The necks are placed opposing each other, the cavity is made circular and wrapped around the pipe. There are three main advantages of this device. First, this device is axisymmetric and prevents coupling between wave types by canceling opposing excitations. Second, this Helmholtz resonator can be made small with the selection of cavity material that is less stiff than metals. A resonator with the shell made of heavy metals has to be about 15 times larger to match resonant frequencies. The last and probably the most important advantage is the ability to tune it externally using clamps to change the stiffness of the shell.

Symmetric distributed vibration absorbers are designed to control the bending and longitudinal shell waves. The spring layer for the DVA is continuous along the pipe circumference and a uniform mass layer is wrapped around it. This single degree of freedom device is not affected by the changes in the polarization angle of the bending

wave. The shearing and normal stiffness of the spring layer can be changed (or chosen) by selecting appropriate material. This allows for the device to have the same resonant frequency in both out of plane and axial directions, thus controlling both the bending and longitudinal wave at the same time.

The symmetric distributed vibration absorber is mechanically analogous to the symmetric Helmholtz resonator. The symmetric Helmholtz resonator can be modeled as a single degree of freedom system in the acoustic domain and the symmetric DVA can be modeled as a single degree of freedom system in the mechanical domain. Both of these devices use the principles of classical control approaches while overcoming their design flaws by removing flanking energy pathways through the use of symmetry. The results presented in section 4.6 for the symmetric Helmholtz resonator and the results presented in section 4.7 for the symmetric vibration absorber show significant reductions at their design frequencies. The results presented in section 4.8 for a hybrid control device that incorporates the symmetric Helmholtz resonator and the symmetric distributed vibration absorber show a reduction of about *20 dB* in power for the fluid wave and *10 dB* in power for the bending wave. The power flow of the longitudinal wave could not be determined and acceleration signals with and without the DVA were measured instead. A *3.5 dB* reduction in the acceleration magnitude can be seen.

Broadband reductions at mid to high frequencies were seen in all passive devices due to bubbles. The existence of bubbles caused pressure values to be as much as *40 dB* down starting at mid frequencies. This coupled with the uncertainties propagating from the decomposition methods made the analyses for these passive devices very difficult. The broadband reduction was observed starting as early as *100 Hz* for the symmetric Helmholtz resonator.

Tested active control approaches were focused around the principle of simultaneous multiple wave type control. In order to achieve good control, all energy transmission pathways have to be controlled at the same time in order to prevent the energy circumventing the control treatment. An active control method utilizing the natural scattering property of discontinuities was developed, which allowed actuators applied to the outside of the pipe to couple into all of the wave types. This was done by placing the actuators at different positions along the pipe with discontinuities (in this case bends in the pipe) between the actuators and the error sensors. In order to investigate the coupling of the actuators to the error sensors a singular value decomposition method was used. A singular value decomposition was performed on this matrix at every frequency and it was determined that the actuators were indeed effectively coupled into the different waves in the system. The main advantage of this technique is the utilization of the inherent discontinuities found in a typical piping installation to incorporate energy from actuators into all wave types to achieve good control. Discontinuities that render passive approaches ineffective make this a powerful control approach which can supplement passive control devices. An overall reduction of *16.4 dB* in shell waves was observed when only acceleration signals were used for errors and an overall reduction of *7 dB* in fluid wave was observed when only pressure transducers were used as errors. A reduction of approximately *16 dB* in shell waves and a reduction of approximately *12 dB* in fluid waves were observed when a combination of accelerometers and pressure transducers were used as errors.

Waves entering discontinuities and the vibro-acoustic behavior of short pipes result in coupled waves. Present research on the determination of wave amplitudes through wave decomposition is limited to two wave types at any given time (the four channel method). The ten-channel method was developed to provide a better understanding of

the vibro-acoustic behavior of fluid-filled pipes. It incorporates all wave types of interest into one decomposition matrix and yields the coupled wave amplitudes. The main disadvantage of this method is the necessity of more discreet measurements. This method will yield the same results as lower channel decomposition methods if the fluid used is changed to air (or another light fluid where the effect of coupling can be neglected). A major shortcoming of this method is the spacing requirement for transducer arrays. The transducers need to be placed further apart at lower frequencies where the wavelengths of the measured waves become very long. Another flaw of this method is the harmonic appearance of large condition numbers. Closely spacing the transducers will increase the intervals at which high condition numbers can be seen. It is, therefore, reasonable to deduce that this method, while advantageous compared to present methods, will still succumb to physical limitations. The wave amplitudes determined using this approach will yield questionable results where the condition number is high. This method is still more powerful and more robust than its predecessors.

6.4. Work to be done in the future

This goal of this study was to develop feasible mechanisms to control vibrations and pulsations in a fluid-filled piping installation. While studies on different approaches has been done by different researchers and can be found in bits and pieces in different publications, a comprehensive study incorporating all these control mechanisms, measurement methods, and practical approaches was absent. It is the author's belief that this publication will bridge the gap between the studies currently available.

There are some subjects that need further research although this publication strives to present many aspects of control approaches related to fluid-filled pipes. Performing finite element analyses of passive control devices would be a major step in the verification process of the conclusions derived in this study. Some of the passive devices that were designed were tested under static pressure conditions and it would be interesting to see their performance under varying loads. The lack of pressure loading may also have adversely affected some results by showing broadband reduction when only a notch type filtering effect is expected and this also requires further investigation.

The performance of active control using external inertial actuators was very promising. The test rig was under 20-40 psi pressure loading and the control results where the harmonic disturbances caused by a pump and the natural mode shapes of the pipes were reduced was acceptable. However, the test rig used in this application was quite small. Application of this method in a larger piping installation is of key interest. The direction of the flow of energy in a piping installation is not well understood. The author believes that active control can be applied after the outlet and before the inlet of the energy transfer device (pump, turbine, etc.) to isolate unwanted vibrations in that section and prevent them from being transmitted into the supporting structure.

The symmetric Helmholtz resonator was found to be an effective passive control device. Its ability to be externally tuned needs to be investigated further. A couple of different stiffness conditions were simulated in the lab and the change in the resonant frequency was verified. Application of a local active control mechanism to change the stiffness of the shell by tightening and loosening the external clamps to make the system adapt to varying external conditions would be an added benefit.

Bubbles caused adverse conditions during the investigation of passive control devices. They caused the response of the system to detoriate starting at mid frequencies. The detrimental effect of the bubbles on tests can actually be used in a beneficial fashion. The bubbles don't affect the response of the system at lower frequencies, but inflict major change in system behavior at higher frequencies. Bubbles may well be introduced into the system intentionally as a control mechanism. Control approaches could be limited to lower frequencies and this could provide more cost effective control solutions.

References

1) Leissa, A. W., 1973 Vibration of Shells, NASA SP-288, *National Aeronautics and Space Administration*, Washington, D.C.
2) Gazis, D. C., 1959 *The Journal of the Acoustical Society of America* 31, pp. 568, Three-dimensional investigation of the propagation of waves in hollow circular cylinders – Analytical foundation.
3) Fuller, C.R., 1981 *Journal of Sound and Vibration*, Volume 75, pp. 207-228, The effects of wall discontinuities on the propagation of flexural waves in cylindrical shells.
4) Fegeant, O., 2001 *Journal of Sound and Vibration*, Volume 243, pp. 89-115, Closed form solutions for the point mobilities of axisymmetrically excited cylindrical shells.
5) Brennan, M. J. & Variyart, W., 2003 *Journal of Sound and Vibration*, Volume 260, pp. 329-348, Simplified mobility expressions for infinite in-vacuo pipes.
6) Variyart, W. & Brennan, M. J., 2002 *Journal of Sound and Vibration*, Volume 256, pp. 955-967, Simplified dispersion relationships for in-vacuo pipes.
7) Zhang, X. M., Liu, G. R., & Lam, K. Y., 2001 *Journal of Sound and Vibration*, Volume 239, pp. 397-403, Vibration analysis of thin cylindrical shells using wave propagation approach.
8) Flügge, W., 1962 *Springer-Verlag (Berlin)*, Stresses in Shells
9) Love, A. E. H., 1944 *Dover Pub., Inc. (New York)*, A Treatise on the Mathematical Theory of Elasticity
10) Donnell, L. H., 1938 *Proceedings of Fifth International Congress on Applied Mech*., A Discussion of Thin Shell Theory

11) Fuller, C. R. & Fahy, F. J., 1982 *Journal of Sound and Vibration*, Volume 81, pp. 501-518, Characteristics of wave propagation and energy distributions in cylindrical shells filled with fluid.

12) Fuller, C. R., 1983 *Journal of Sound and Vibration*, Volume 87, pp. 409-427, The input mobility of an infinite circular cylindrical elastic shell filled with fluid.

13) Fuller, C. R., 1984 *Journal of Sound and Vibration*, Volume 96, pp. 101-110, Monopole excitation of vibrations in an infinite cylindrical elastic shell filled with fluid.

14) Brevart, B. J. & Fuller, C. R., 1994 *Journal of Sound and Vibration*, Volume 177, pp. 411-422, Radial impulsive excitation of infinite fluid-filled elastic cylindrical shells.

15) Brevart, B. J. & Fuller, C. R., 1996 *Journal of Sound and Vibration*, Volume 190, pp. 763-774, Energy exchange between the coupled media of impulsively excited, fluid-filled, elastic cylinders.

16) Finnveden, S., 1997 *Journal of Sound and Vibration*, Volume 208, pp. 685-703, Simplified equations of motion for the radial-axial vibrations of fluid-filled pipes.

17) Finnveden, S., 1997 *Journal of Sound and Vibration*, Volume 208, pp. 705-728, Formulas for modal density and for input power from mechanical and fluid point sources in fluid filled pipes.

18) Feng, L., 1994 *Journal of Sound and Vibration*, Volume 176, pp. 399-413, Acoustic properties of fluid-filled elastic pipes.

19) Feng, L., 1996 *Journal of Sound and Vibration*, Volume 189, pp. 511-524, Experimental studies of the acoustic properties of a finite elastic pipe filled with water/air.

20) Xu, M. B. & Zhang, X. M., 1998 *Journal of Sound and Vibration*, Volume 218, pp. 587-598, Vibration power flow in a fluid-filled cylindrical shell.

21) Xu, M. B. & Zhang, W. H., 2000 *Journal of Sound and Vibration*, Volume 234, pp. 387-403, Vibrational power flow input and transmission in a circular cylindrical shell filled with fluid.

22) Zhu, F., 1995 *Journal of Sound and Vibration*, Volume 186, pp. 543-550, Rayleigh-Ritz method in coupled fluid-structure interacting system and its applications.

23) Pinnington, R. J., 1997 *Journal of Sound and Vibration*, Volume 204, pp. 271-289, The axisymmetric wave transmission properties of pressurized flexible tubes.

24) Zhang, L., Tijsseling, A. J., & Vardy, A. E., 1999 *Journal of Sound and Vibration*, Volume 224, pp. 69-99, FSI analysis of liquid-filled pipes.

25) Tijdeman, H., 1975 *Journal of Sound and Vibration*, Volume 39, pp. 1-33, On the propagation of sound waves in cylindrical tubes

26) Michalke, A., 1989 *Journal of Sound and Vibration*, Volume 134, pp. 203-234, On the propagation of sound generated in a pipe of circular cross-section with uniform mean flow.

27) Gorman, D. G., Reese, J. M, & Zhang, Y. L., 2000 *Journal of Sound and Vibration*, Volume 230, pp. 379-392, Vibration of a flexible pipe conveying viscous pulsating fluid flow.

28) Brevart, B. J. & Fuller, C. R., 1993 *Journal of Sound and Vibration*, Volume 167, pp. 149-163, Effect of an internal flow on the distribution of vibrational energy in an infinite fluid-filled thin cylindrical elastic shell.

29) Chung, J. Y. & Blaser, D. A., 1980 *The Journal of the Acoustical Society of America*, Volume 68, pp. 907-921, Transfer function method of measuring in-duct acoustic properties.

30) Pavić, G., 1992 *Journal of Sound and Vibration*, Volume 143, pp. 411-429, Vibroacoustical energy flow through straight pipes.

31) Fahy, F. J., 1977 *The Journal of the Acoustical Society of America*, Volume 62, pp. 1057-1059, Measurement of acoustic intensity using the cross-spectral density of two microphone signals.

32) Pavić, G., 1976 *Journal of Sound and Vibration*, Volume 49, pp. 221-230, Measurement of structure-borne wave intensity, Part I: Formulation of the methods.

33) Pavić, G., 1977 *Journal of Sound and Vibration*, Volume 51, pp. 533-545, Measurement of sound intensity

34) Verheij, J. W., 1980 *Journal of Sound and Vibration*, Volume 70, pp. 133-138, Cross spectral density methods for measuring structure borne power flow on beams and pipes.

35) Verheij, J. W., 1990 *Noise Control Engineering Journal*, Volume 35, pp.69-76, Measurement of structure-borne wave intensity on lightly damped pipes.

36) Royston, T. J., 1995 *Noise Control Engineering Journal*, Volume 43, pp. 15-20, Technical Note: Shaped polyvinlidene fluoride (PVDF) sensors for intelligent measurement of plane-wave acoustic pressure in liquid-filled pipes.

37) Pinnington, R. J. & Briscoe, A. R., 1994 *Journal of Sound and Vibration*, Volume 173, pp. 503-516, Externally applied sensor for axisymmetric waves in a fluid filled pipe.

38) Briscoe, A. R. & Pinnington, R. J., 1996 *Journal of Sound and Vibration*, Volume 192, pp. 771-791, Axisymmetric vibrational power measurement in empty and fluid filled pipes.

39) Taylor, P. D., 1990 *Proceedings of CETIM 3rd International Congress on Intensity Techniques*, pp. 249-256, Measurement of structural intensity, reflection coefficient and termination impedance for bending waves in beams.

40) Jong, C. A. F. de & Verheij, J. W., 1992 *Proc. 2nd International congress on recent developments in air & structure-borne sound and vibration*, Measurement of energy flow along pipes.

41) Jong, C. A. F. de, *Ph.D. Thesis, Eindhoven University of Technology*, Analysis of pulsations and vibrations in fluid-filled pipe systems

42) Ming, R. S., Pan, J., & Norton, M. P., 2001 *Journal of Sound and Vibration*, Volume 242, pp. 719-735, The measurement of structure-borne sound energy flow in an elastic cylindrical shell

43) Finnveden, S., 1997 *Journal of Sound and Vibration*, Volume 199, pp. 125-154, Spectral finite element analysis of the vibration of straight fluid-filled pipes with flanges.

44) Xu, M. B., Zhang, X. M., & Zhang, W. H., 1999 *Journal of Sound and Vibration*, Volume 224, pp. 395-410, The effect of wall joint on the vibrational power flow propagation in a fluid-filled shell.

45) Dodson, J. M., Dowling, D. R., & Grosh, K., 1998 *Noise Control Engineering Journal*, Volume 46, pp. 15-22, Experimental investigation of quarter wavelength silencers in large-scale hydraulic systems.

46) Kravchenko, S. V., 1994 *Proc. Internoise 94*, Active vibration isolation in pipes conveying fluid.

47) Lin, Y. H. & Tsai, Y. K, 1997 *Journal of Sound and Vibration*, Volume 202, pp. 477-490, Non-linear active vibration control of a cantilever pipe conveying fluid.

48) Brevart, B. J., *Ph.D. Dissertation, Virginia Polytechnic Institute and State University*, Active control of coupled wave propagation in fluid-filled elastic cylindrical shells.

49) Maillard, J., 1998 *Research report: University of Karlskrona/Ronneby, Ronneby, Sweden*, Active control of pressure pulsations in piping systems.

50) Ruotolo, R., 2001 *Journal of Sound and Vibration*, Volume 243, pp. 847-860, A comparison of some thin shell theories used for the dynamic analysis of stiffened cylinders.

51) Muggleton, J. M., Brennan, M. J., & Pinnington, R. J., 2002 *Journal of Sound and Vibration*, Volume 249, pp. 939-954, Wavenumber prediction of waves in buried pipes for water leak detection.

52) Xu, M. B., Zhang, X. M., & Zhang, W. H., 1999 *Journal of Sound and Vibration*, Volume 222, pp. 531-546, Space-harmonic analysis of input power flow in a periodically stiffened shell filled with fluid.

53) Feng, L., 1995 *Journal of Sound and Vibration*, Volume 183, pp. 169-178, Noise and vibration of a fluid filled elastic pipe coated with an absorptive layer on the inner side of the wall.

54) Liu, M., Keane, A. J., & Taylor, R. E., 2000 *Journal of Sound and Vibration*, Volume 238, pp. 547-574, Modeling liquid-structure interactions within the framework of statistical energy analysis.

55) Kiyar, M. B., Johnson, M. E., & Fuller, C. R., 2001 *Report to Hyundai Contract No: 01-0636-10*, A study on minimization of structure-borne noise generated by fluid-borne excitation in a ship's pipeline system.

56) Kiyar, M. B., Johnson, M. E., & Fuller, C. R., 2002 *Report to Hyundai Contract No: 02-1126-12*, Integrated passive control methods for the reduction of vibration power flow from fluid-filled piping systems into supporting structures.

57) Kiyar, M. B., Johnson, M. E., & Fuller, C. R., 2002 *Proceedings of IMEC 2002 New Orleans, LA*, Experiments on the active control of multiple wave types in fluid filled piping systems.

58) Pavić, G., 1990 *Journal of Sound and Vibration*, Volume 142, pp. 293-310, Vibrational energy flow in elastic circular cylindrical shells.

59) Soedel, W., 1981 *Marcel Dekker, New York*, Vibrations of shells and plates.

60) Heckl, M. & Cremer, L., 1973 *Springer-Verlag, Berlin*, Structure-borne Sound

61) Morgan, D. R., 1980 *IEEE Transactions on Acoustics Speech and Signal Processing*, An analysis of multiple correlation cancellation loops with a filter in the auxiliary path, ASSP-28, pp. 454-467

62) Widrow, B., Shur, D., & Shaffer, S., 1981 *Proc. 15th ASILOMAR Conference on Circuits, Systems and Computers*, On adaptive inverse control, pp. 185-195

63) Burgess, J. C., 1981 *The Journal of the Acoustical Society of America*, Active adaptive sound control in a duct: a computer simulation, Volume 70, pp. 715-726

64) Elliott, S. J., 2001 *Academic Press*, Signal Processing for Active Control

65) Fuller, C. R., Elliott, S. J., & Nelson, P. A., 1997 *Academic Press*, Active Control of Vibrations

66) Nelson, P. A. & Elliott, S. J. 1992 *Academic Press*, Active Control of Sound

67) Skaistis, S., 1988, *Marcel Dekker Inc*., Noise Control of Hydraulic Machinery

68) Junger, C. J. & Feit, D., 1972, *The MIT Press*, Sound, Structures, and Their Interaction

69) Kinsler, L. E., Frey, A. R., Coppens, A. B., & Sanders, J. V., 2000, *John Wiley & Sons, Inc.*, Fundamentals of Acoustics

Vita

M. Baris Kiyar was born on April 1st, 1978 in Istanbul. His early childhood was spent moving from one place to other. He attended elementary school in various locations in Turkey and Kiel, Germany. He attended Jr. High and high school in Turkey and Japan. He attended Istanbul Technical University majoring in mechanical engineering (manufacturing) with a minor in automotive engineering, following his graduation from Kadikoy Anadolu High School in Istanbul. He held the positions of vice president of student body and president of student body in his junior and senior years in ITU, respectively. He was a starting member of Citlembik Ltd., which specialized in IT solutions. He worked as the editor of Computer Shopping magazine during his last years in ITU. He worked as Chief Field Engineer in Zawiya, Libya, for STFA Construction Co. He has played drums professionally and for pleasure since 1992. This, coupled with the acoustics books his father had, sparked his interest in vibrations and acoustics. He worked on his Master's degree in the Vibration and Acoustics Laboratories under the guidance of Dr. Chris Fuller and Dr. Marty Johnson.

Appendix A: Dispersion Surfaces

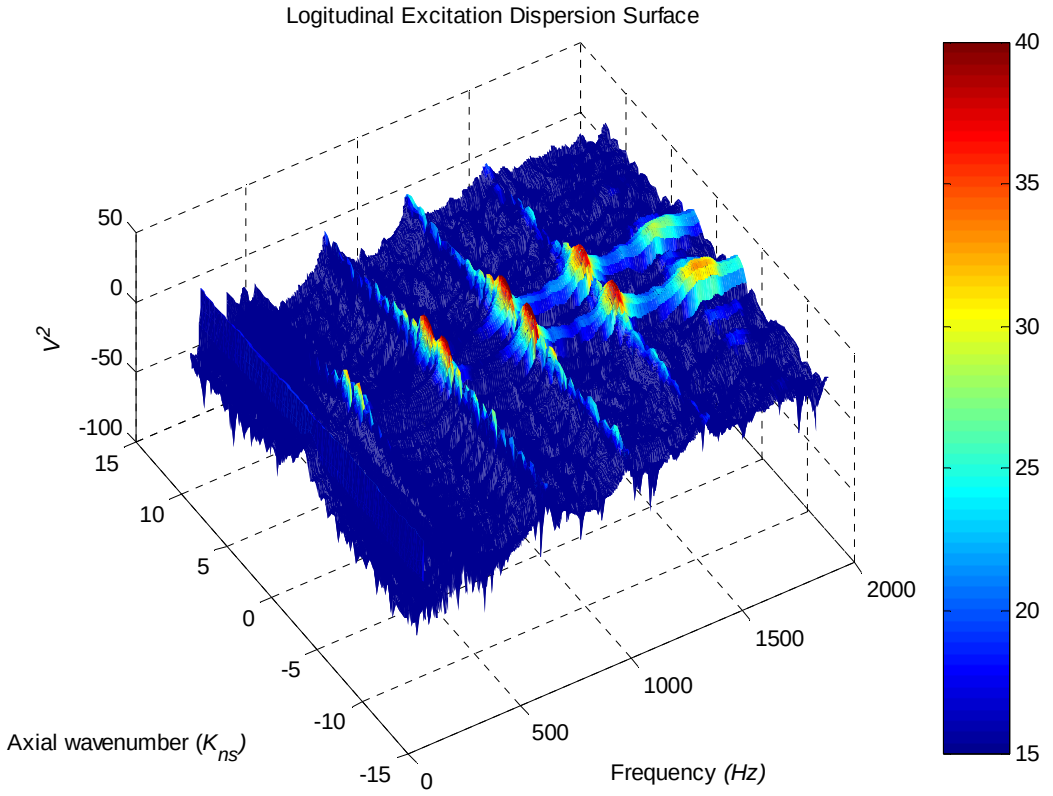

Figure A.1. Dispersion surface for longitudinal wave

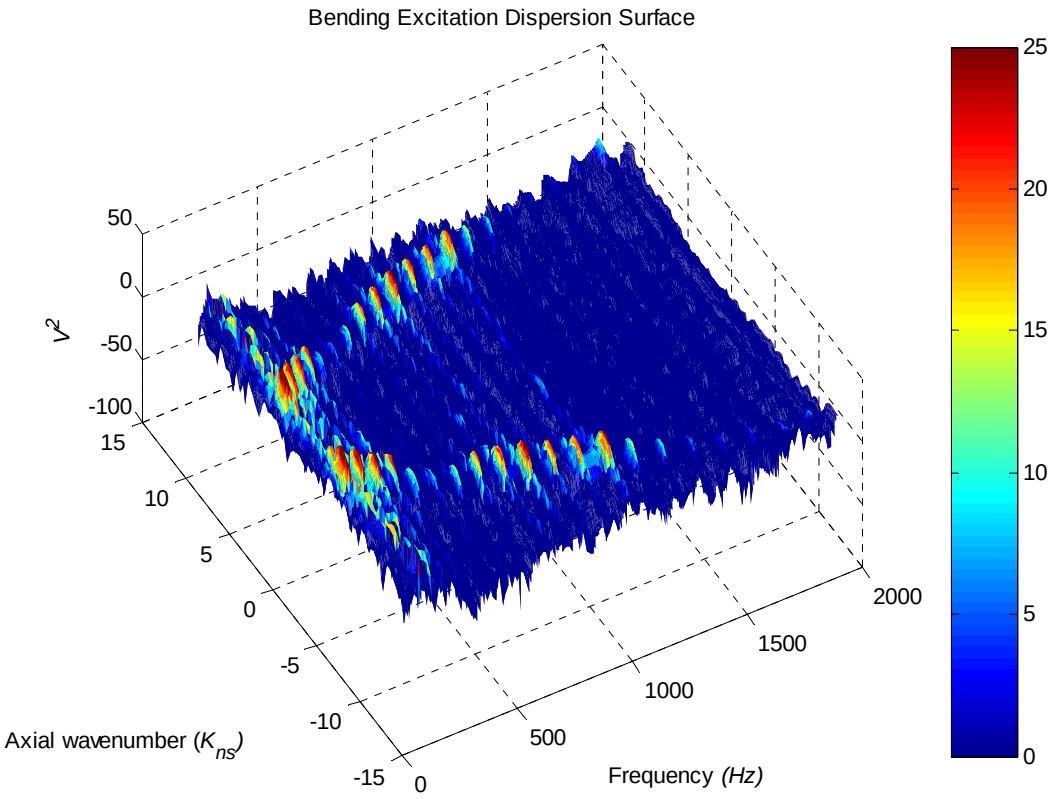

Figure A.2. Dispersion surface for bending wave

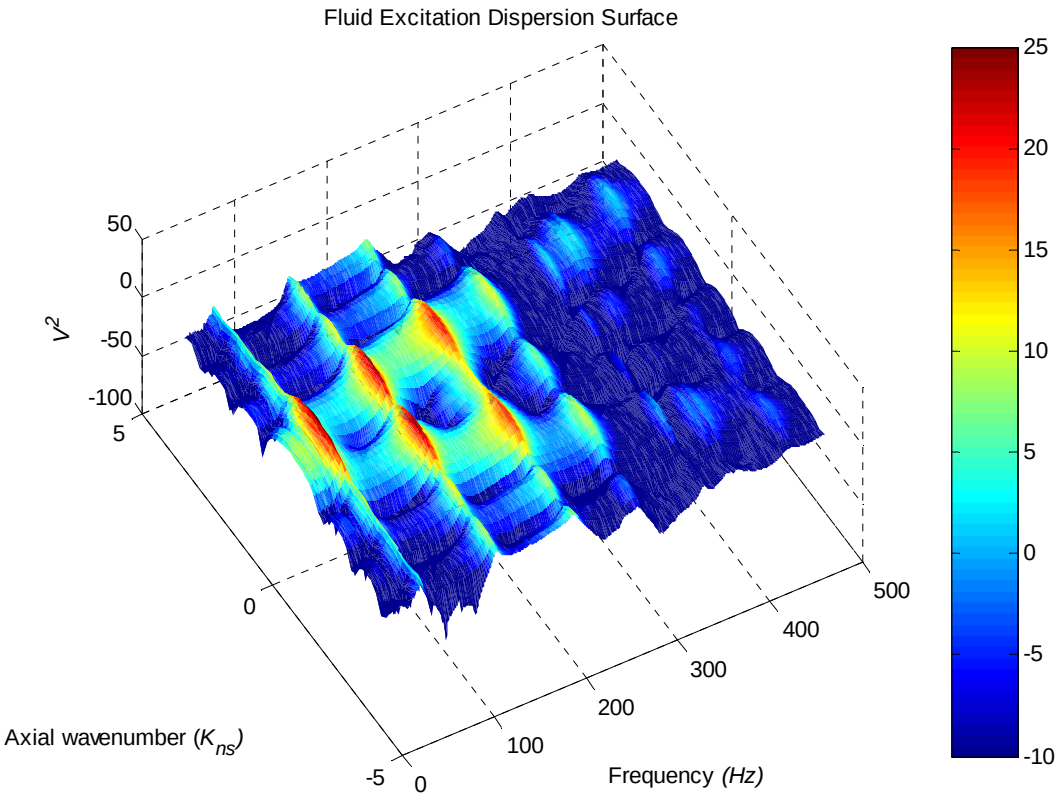

Figure A.3. Dispersion surface for fluid wave

Appendix B: Finite element analysis of classical Helmholtz resonator

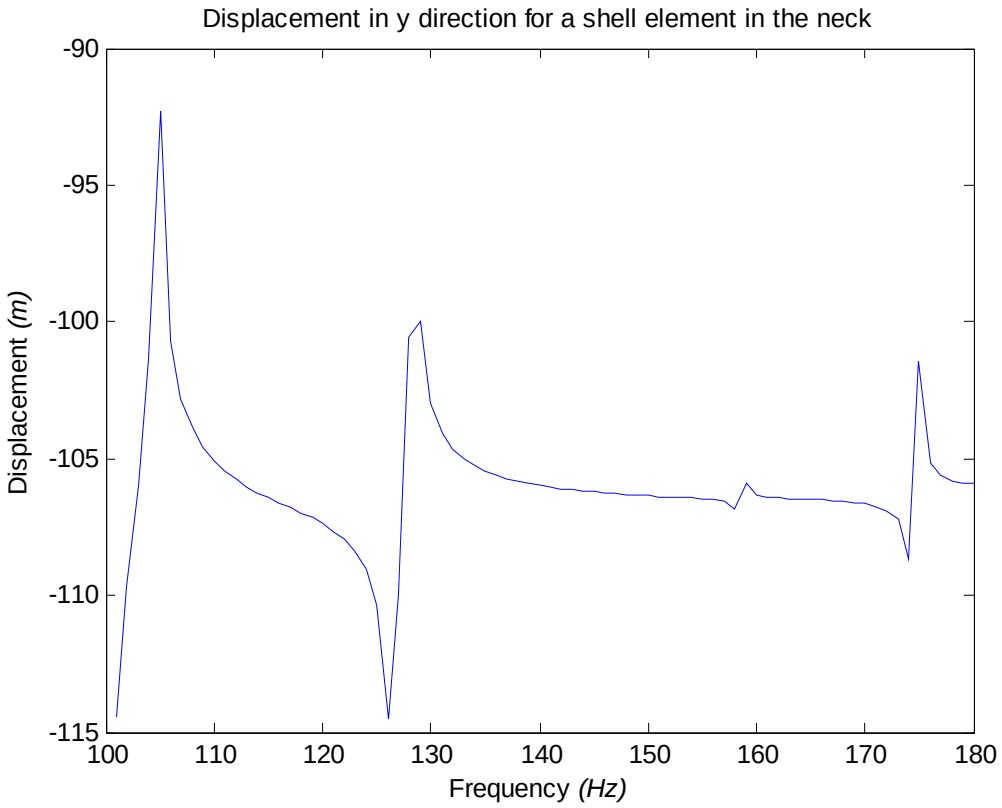

Figure B.1. y axis displacement of a shell element at the neck of a classical Helmholtz resonator

Appendix C: Formulation of pipe impedances and bubbles

This appendix will describe the formulation of pipe impedances and bubbles used in the simulation scenarios of section 4.2. A schematic of these scenarios is shown in figure C.1. In this setup, we have a known velocity distribution in the form of V_{a1}, which is the velocity of the piston. Sections *B* and *C* do not have any sources and pressure values along sections *A* and *B* are evaluated with changing conditions (i.e. quarter-wavelength tube, rigid wall, bubble, etc.) of section *C*.

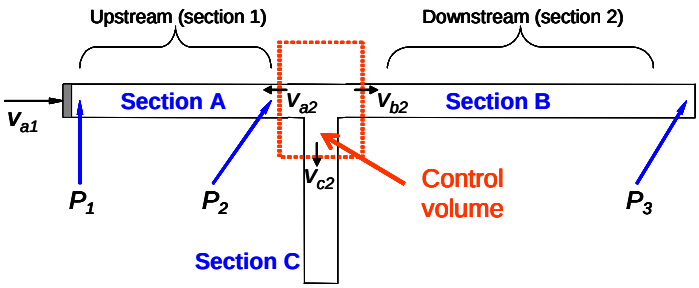

Figure C.1. Schematic of simulation setup

Pipe Impedance

Assuming that the fluid in a fluid-filled pipe of cross-sectional area *S* and length *L* is driven by a piston at *x=0* and that the pipe is terminated at *x=L* with a mechanical impedance of Z_{ml} and following closely with the formulation of Kinsler *et al* [69], propagating waves in the pipe will be of the form:

$$p(x,t) = Ae^{j[\omega t + k(L-x)]} + Be^{j[\omega t - k(L-x)]} \qquad \text{(C.1)}$$

where the amplitudes *A* and *B* are determined by the boundary conditions at *x=0* and *x=L*. The continuity of particle velocity and the continuity of force require that the mechanical impedance of the wave at *x=L* equals the mechanical impedance Z_{ml} of the termination, yielding:

$$Z_{ml} = \rho_o c S \frac{A+B}{A-B} \tag{C.2}$$

The input mechanical impedance at *x=0* is given as:

$$Z_{m0} = \rho_o c S \frac{Ae^{jkL} + Be^{-jkL}}{Ae^{jkL} - Be^{-jkL}} \tag{C.3}$$

Combining equations C.2 and C.3 and eliminating the amplitude coefficients *A* and *B* yields:

$$\frac{Z_{m0}}{\rho_o c S} = \frac{\left(Z_{mL} \big/ \rho_o c S\right) + j\tan(kL)}{1 + j\left(Z_{mL} \big/ \rho_o c S\right)\tan(kL)} \tag{C.4}$$

For resonance let the pipe be driven at *x=0* and closed at *x=L* with a rigid cap which will mean $\left|Z_{mL} / \rho_o c S\right| \to \infty$ in equation C.4, which will yield:

$$Z_{m0} = -j\rho_o c S \cot(kL) \tag{C.5}$$

Transfer impedance relates the pressure at the end of the pipe to the particle velocity at the source and will be required in order to couple the pipe sections together. The transfer impedance is given by:

$$Z_t = -j\rho_o cS \Big/ \sin(kL) \tag{C.6}$$

Bubble impedance

The stiffness of a bubble can be modeled analogous to the stiffness of a Helmholtz resonator. The bubble is assumed to be a cylindrical cavity with a volume much less than of the fluid surrounding it. The surface where the compression is applied is of the same size as the cross-sectional area of the pipe. If the volume is modeled as a cavity with area *S* and if the volume is changed by $\Delta V = -S\xi$ i.e. a displacement of ξ, the resulting condensation will be given as:

$$\frac{\Delta\rho}{\rho} = -\frac{\Delta V}{V} = \frac{S\xi}{V} \tag{C.7}$$

where *V* is the volume and ρ is the density.

The pressure increase is given by:

$$p = \rho_o c^2 \Delta\rho \Big/ \rho = \rho_o c^2 S\xi \Big/ V \tag{C.8}$$

The force f required to maintain displacement is:

$$f = Sp = s\xi \tag{C.9}$$

and the effective stiffness is given by:

$$s = \rho_o c^2 S^2 / V \tag{C.10}$$

The input mechanical impedance of a bubble can be written as:

$$Z_m = j\frac{s}{\omega} \tag{C.11}$$

where *s* is the stiffness and ω is the frequency.

Simulating a three section system

A constant velocity distribution was applied at a piston at *x=0* for the simulation scenario presented in section 4.2. The transfer and input impedances for the pipe sections were then used with the continuity of pressure and volume velocity equations for the control volume to obtain P_1, P_2, and P_3 values as seen in figure C.1.

The continuity of pressure states that the pressures of the three sections must be equal at the control volume. These pressure values can also be modeled using a combination of velocities, input impedances, and transfer impedances, which yields:

$$P_{a2} = Z_{ta}V_{a1} + Z_{0a}V_{a2} = Z_{0b}V_{b2} = Z_{0c}V_{c2} \quad \text{(C.12)}$$

where V_{a1} is the velocity of the piston, V_{a2}, V_{b2}, and V_{c2} are the velocities of the waves exiting the control volume and Z_{ta} is the transfer impedance between pressure values one end of the pipe *A* to a source at the other end. Z_{0a}, Z_{0b}, and Z_{0c} are the input impedances into the three pipe sections. From the continuity of volume velocity:

$$V_{a2} + V_{b2} + V_{c2} = V_{a2} + V_{b2} + V_{b2}\frac{Z_{0b}}{Z_{0c}} = 0 \quad \text{(C.13)}$$

Combining equations C.12 and C.13 yields the following relationship between velocities:

$$V_{a1} = \frac{\left[Z_{0b} + Z_{0a} + \frac{Z_{0b}Z_{0a}}{Z_{0c}} \right]}{Z_{ta}} V_{b2} \quad \text{(C.14)}$$

The remaning velocity values V_{a2}, V_{b2}, and V_{c2} can be calculated using equation C.12 since V_{a1} is known and the pressure values can be calculated as:

$$P_1 = V_{a1}Z_{0a} + V_{a2}Z_{ta} \quad \text{(C.15)}$$

$$P_2 = V_{a1}Z_{ta} + V_{a2}Z_{0a} \quad \text{(C.16)}$$

$$P_3 = V_{b2}Z_{tb} \quad \text{(C.17)}$$

Z_{ta} and Z_{tb} are the transfer impedances of pipe section A and pipe section B, respectively. Different values of Z_{0c} are used for the simulation scenario. An impedance value of infinity is applied to simulate a rigid walled boundary condition (i.e. a continuous pipe). An impedance value of zero is applied for a pressure release boundary condition. The exact impedance of a short pipe section as seen in equation C.5 is applied for a quarter wavelength tube and the impedance of a bubble is applied to simulate a bubble case as defined in equation C.11.